"An Investigation of Microstructure and Mechanical Properties of Low Carbon Steels subjected to Welding"

Von der Fakultät für Georessourcen und Materialtechnik der Rheinisch -Westfälischen Technischen Hochschule Aachen

zur Erlangung des akademischen Grades eines

Doktors der Ingenieurwissenschaften

genehmigte Dissertation

vorgelegt von

Herrn Krishna Chaitanya Komerla, M. Sc.

aus Proddatur, Indien

Berichter: Herr Univ.-Prof. Dr.-Ing. Wolfgang Bleck
            Herr Univ.-Prof. Dr.-Ing. Uwe Reisgen

Tag der mündlichen Prüfung: 11.11.2020

Diese Dissertation ist auf den Internetseiten der Universitätsbibliothek online verfügbar

The Effect of Beam Oscillations on the Microstructure and Mechanical Properties of Electron Beam Welded Steel Joints

K. Komerla, S. Gach, T. Vossel, A. Schwedt, A. Bührig-Polaczek, U. Reisgen, W.Bleck (2019), The International Journal of Advanced Manufacturing Technology 102:1–13. https://doi.org/10.1007/s00170-019-03355-4

Investigation of Microstructure and Mechanical Properties of Friction Stir Welded AA6016-T4 and DC04 Alloy Joints

K. Komerla, A. Naumov, C. Mertin, U. Prahl, W. Bleck (2018), The International Journal of Advanced Manufacturing Technology 94(9):4209–4219. https://doi.org/10.1007/s00170-017-1022-6

Finite Element Simulation of Residual Stress Induced by High Energy Beam Welding in Dual Phase Steel

K. Komerla, S. Gach, F. Akyel, T. Vossel, U. Reisgen, W. Bleck (2020), Lasers in Manufacturing and Materials Processing. https://doi.org/10.1007/s40516-020-00112-4

To Jaya, Seechi & Babu for their endless love and support

Acknowledgements

I would like to express my gratitude to my advisor Professor Bleck for his guidance and support during my stay at the Steel Institute, RWTH Aachen University. I am also grateful to professor Reisgen for his very helpful suggestions on the welding part of this thesis.

Special thanks are due to my friends Manjunatha Madivala, Patrick Fayek and Alexandros Serafeim for their invaluable suggestions and constructive comments. I would also like to thank my friends and colleagues Stefan Gach, Fatma Akyel and Andreas Naumov for their help in carrying out the experiments and proof reading the articles.

Last, but by no means less, I would like to thank my wife Prathyusha and my sister Krishna Priya for their continuous support and encouragement.

Abstract

Welding is a complex thermo-mechanical process in which, under transient and non-equilibrium conditions multiple metallurgical phenomena can occur simultaneously. The weld thermal cycles introduce significant alterations to the microstructure of material and thereby, affect the mechanical properties of the weldments. In order to create a sound joint, it is essential to understand the impact of various process parameters on the weld microstructure and weld mechanical properties. Beyond conventional process parameters like, acceleration voltage, amperage, welding speed and applied external pressure, a deeper understanding of the influence of welding parameters like tool offset, beam oscillations and oscillation trajectories is necessary to produce long lasting and sustainable joints. In this study, the effect of such uncommon process parameters on the quality of welds is presented. To that end, the two following welding methods have been investigated.

1. Fusion welding - High energy beam welding

2. Pressure welding - Dissimilar friction stir welding

Low carbon steels like the automotive dual phase steel (DP1000) and deep drawable mild steel DC04 each possessing 1 mm thickness, along with a 5 mm thick structural steel S235JR were investigated. Additionally, for dissimilar friction stir welding, a 1.12 mm thick solution treated and aged aluminum alloy AL6016-T4 was also studied. Results indicate that, for the same weld heat input, the application of uncommon process parameters can yield a range of different weld microstructures that exhibit improved weld mechanical properties.

In the case of high energy beam welding, beam oscillations were applied to create a dynamic distribution of power around the stationary position of the beam that enhanced the flow of heat inside the keyhole and created wider fusion and heat-affected zones. A reduction in the size of welding crowns could be achieved by simply oscillating the energy source. As a consequence of this dynamic power distribution, the weld microstructure exhibited large columnar grains in the fusion zone and equiaxed grains of varying size in the heat-affected zone. This variation in grain size across the weld joint could be attributed to the steep temperature gradient produced during electron beam welding. Typically high hardness is observed in welds due to the occurrence of quenched martensite during conventional welding. However, weld samples fabricated using beam oscillations possessed not only lower hardness but also exhibited good tensile strength, lower residual stress and minimal distortion in comparison to the joints produced by stationary beam welding. This decrease in hardness arose from enhanced grain growth and additional indirect tempering like effect caused by beam oscillations.

While in the case of friction stir welding, the tool offset resulted in a mode of welding where, minimal shear strain was accumulated in steel and complete dynamic recrystallization of microstructure in aluminum was achieved. Additionally,

macroscopic defect free and inter-metallic compound free joints were obtained, with only a small fraction of Fe chips embedded in the aluminum matrix. Through plastic deformation and thermal effects, significant differences in grain size and micro-hardness were created in the weld joint. High temperatures and extreme strain rates inherent to the welding process, activated the dynamic recrystallization of microstructure in the aluminum alloy. The kernel average misorientation map revealed the lack of stored deformation energy, indicating the presence of fully recrystallized grains. However, due to its high thermal stability, steel did not recrystallize but, exhibited marginal grain growth in both thermo-mechanically affected zone and heat-affected zone. It also contained a highly refined grain structure in the weld zone. The texture maps plotted for the weld zone of Fe alloy showed weak shear texture indicating minimal shear strain accumulation. Thus, by adopting such process parameters and understanding their impact on the microstructure, joints with enhanced life can be produced at low costs.

However, experimental research of such parameters is both time consuming and expensive. Hence, there is a strong need for numerical models that predict the final mechanical state of the weldments. Therefore, such an attempt is also made towards the development of a metallurgical framework in this project to study and analyse the process of welding, its metallurgy and microstructure. A sequentially coupled finite element formulation was adopted to simulate the fusion welding process. To accurately predict the sharp temperature gradients across the different weld zones, a moving volumetric heat source model, combining a spherical and a conical thermal flux distribution was developed. The temperature profiles computed with this heat source model were found to be in excellent agreement with the experimentally measured data. Additionally, a comparison of the optical micrographs with the simulated weld geometries further strengthened the basis of the developed framework.

Zusammenfassung

Schweißen ist ein komplexer thermomechanischer Prozess, bei dem unter transienten und Ungleichgewichtsbedingungen mehrere metallurgische Phänomene gleichzeitig auftreten können. Die Wärmezyklen bei dem Schweißvorgang führen zu erheblichen Änderungen der Mikrostruktur des Materials und beeinflussen dadurch die mechanischen Eigenschaften der Schweißteile. Um eine stabile Verbindung herzustellen, ist es wichtig, die Auswirkungen der verschiedenen Prozessparameter auf die Schweißgefüge und die mechanischen Eigenschaften der Schweißnaht zu verstehen. Neben konventioneller Prozessparameter wie, Beschleunigungsspannung, Stromstärke, Schweißgeschwindigkeit und angewandten Außendruck, ein tieferes Verständnis des Einflusses von Schweißparameter wie Werkzeugversatz, Strahloszillationen und Oszillationstrajektorien erforderlich ist um langlebige und nachhaltige Verbindungen herzustellen. In dieser Studie wird die Wirkung solcher unkonventioneller Prozessparameter zur Qualität von Schweißnähten vorgestellt. Zu diesem Zweck wurden die beiden folgenden Schweißverfahren untersucht

1. Schmelzschweißverfahren - Hochenergiestrahlschweißen

2. Druckschweißen - Reibrührschweißen

Kohlenstoffarme Stähle wie der Dualphasenstahl für die Automobilindustrie (DP1000) und der tiefziehbare DC04, die jeweils 1 mm dick, sowie ein 5 mm dicker Baustahl S235JR wurden untersucht. Zusätzlich wurde für das ungleiche Reibrührschweißen eine 1,12 mm dicke lösungsbehandelte und gealterte Aluminiumlegierung AL6016-T4 ebenfalls untersucht. Die Ergebnisse deuten darauf hin, dass bei gleichem Wärmeeintrag die Anwendung der unkonventioneller Prozessparameter können eine Reihe von verschiedener Schweißgefüge ergeben, die verbesserte mechanische Eigenschaften der Schweißnaht aufweisen.

Bei den Hochenergiestrahlschweißen wurden Strahlschwingungen angewendet, um eine dynamische Leistungsverteilung um die stationäre Position des Strahls herum zu erzeugen, die den Wärmefluss im „Keyhole" verbessert und breitere Schmelz- und Wärmeeinflusszonen erzeugte. Eine Reduzierung der Größe von Schweißkronen konnte durch einfaches Oszillieren der Energiequelle erreicht werden. Infolge dieser dynamischen Leistungsverteilung zeigte die Schweißmikrostruktur große säulenförmige Körner in der Schmelzzone und gleichachsige Körner mit unterschiedlicher Größe in der Wärmeeinflusszone. Diese Variation der Korngröße über die Schweißverbindung könnte auf den steilen Temperaturgradienten zurückgeführt werden, der bei dem Elektronenstrahlschweißen erzeugt wird. Typischerweise wird bei Schweißnähten eine hohe Härte beobachtet, da beim herkömmlichen Schweißen abgeschreckter Martensit auftritt. Schweißproben, die unter Verwendung von Strahloszillationen hergestellt wurden, besaßen jedoch nicht nur eine geringere Härte, sondern zeigten auch eine erhöhte Zugfestigkeit, eine geringere Restspannung und minimalen Verzug im Vergleich zu den durch stationäres

Strahlschweißen erzeugten Fugen. Diese Abnahme der Härte ergab sich aus einem verstärkten Kornwachstum und einer zusätzlichen Diffusion von Kohlenstoff aus dem Austenit Gitter, die durch Strahlschwingungen verursacht wurden.

Im Falle des Reibrührschweißens, der Werkzeugversatz führte zu einem Schweißmodus, bei dem sich minimale Scherdehnungen im Stahl akkumulierten und eine vollständige dynamische Rekristallisation der Mikrostruktur im Aluminium erreicht wurde. Zusätzlich wurden makroskopisch defektfreie und intermetallische verbindungsfreie Verbindungen erzielt. Wobei, nur ein kleiner Teil der Fe-Späne in die Aluminiummatrix eingebettet war. Durch plastische Verformung und thermische Effekte wurden signifikante Unterschiede in der Korngröße und Mikrohärte in der Schweißverbindung erzeugt. Hohe Temperaturen und extreme Dehnraten, die bei dem Schweißprozess auftreten, aktivierten die dynamische Rekristallisation der Mikrostruktur in der Aluminiumlegierung. Die kernel average misorientation (KOM) karte zeigte den Mangel an gespeicherter Deformationsenergie, was auf das vollständige rekristallisation hinweist. Aufgrund seiner hohen thermischen Stabilität rekristallisierte Stahl jedoch nicht, sondern wies sowohl in der thermomechanisch beeinflussten Zone als auch in der Wärmeeinflusszone ein marginales Kornwachstum auf. Es enthielt auch eine sehr feine Kornstruktur in der Schweißzone. Die für die Schweißzone der Fe-Legierung aufgetragenen Texturkarten zeigten eine schwache Schertextur, was auf eine minimale Scherdehnungsakkumulation hinweist. Durch die Anwendung solcher Prozessparameter und das Verständnis ihrer Auswirkungen auf die Mikrostruktur können Verbindungen mit verbesserter Lebensdauer zu niedrigen Kosten hergestellt werden.

Die experimentelle Erforschung solcher Parameter ist jedoch sowohl zeitaufwendig als auch teuer. Daher besteht ein großer Bedarf an numerischen Modellen, die den mechanischen Endzustand der Schweißverbindungen vorhersagen. Daher wird in diesem Projekt auch ein solcher Versuch unternommen, einen metallurgischen Rahmen zu entwickeln, um den Prozess des Schweißens, seine Metallurgie und Mikrostruktur zu untersuchen und zu analysieren. Zur Simulation des Schmelzschweißprozesses wurde eine sequentiell gekoppelte Finite-Element-Formulierung angenommen. Um die scharfen Temperaturgradienten über die verschiedenen Schweißzonen genau vorherzusagen, wurde ein bewegliches volumetrisches Wärmequellenmodell entwickelt, das eine konisch und eine kugelförmige Wärmeflussverteilung kombiniert. Die mit diesem Wärmequellenmodell berechneten Temperaturprofile stimmten hervorragend mit den experimentell gemessenen Daten überein. Zusätzlich wurde durch einen Vergleich der optischen Schliffbilder mit den simulierten Schweißgeometrien, die Basis des entwickelten Rahmens weiter gestärkt.

Contents

Contents

Nomenclature

α	Ferrite
$\alpha^{'}$	Martensite
γ	Austenite
Ac_1	Austenite start temperature
Ac_3	Austenite finish temperature
M_f	Martensite finish temperature
M_s	Martensite start temperature
BCC	Body centred cubic
BCT	Body centred tetragonal
BM	Base material
CE	Carbon equivalent value
CGHAZ	Coarse grained heat affected zone
CPD	Cumulative probability distribution
DIC	Digital image correlation
DP	Dual phase
EBSD	Electron back scatter diffraction
EBW	Electron beam welding
EDS	Energy dispersive spectroscopy
FCC	Face centred cubic
FEM	Finite element method
FGHAZ	Fine grained heat affected zone
FL	Fusion line
FSW	Friction stir welding
FZ	Fusion zone
GNB	Geometrically necessary boundary

Nomenclature

GTAW	Gas tungsten arc welding
HAZ	Heat affected zone
HV	Vickers hardness
IMC	Inter-metallic compound
KAM	Kernel average misorientation
LOM	Light optical microscopy
MH	Micro-hardness
RD	Rolling direction
SD	Shear direction
SEM	Scanning electron microscope
SN	Shear normal
TD	Transverse direction
TE	Total elongation
TMAZ	Thermo-mechanically affected zone
UTS	Ultimate tensile strength
WZ	Weld zone

1 Introduction

Today, welding is extensively used in the fabrication of various machine parts and structural components for automobiles, ships, pressure vessels, aerospace carriers etc., and it certainly is advantageous over many other fabrication techniques. For example, in the production of turbines for power generation and aerospace applications, welding technologies have aided in replacing large casted parts with welded sub-assemblies, and thereby reduced both production cost and manufacturing time [1, 2, 3, 4].

Welding is a remarkably complicated, non-linear operation that is riddled with challenges. The transient heating and subsequent cooling cycles, that materials experience during welding, alter the microstructures locally and thus create complex strain fields. These inhomogeneous strain fields in turn give rise to geometrical distortions, residual stresses and their adverse effects such as brittle failure, reduced fatigue life, stress corrosion cracking, buckling of structural elements and others. Despite being the most common technology used in metal fabrication, the influence of welding process parameters on the thermo-mechanical behaviour of materials is not yet thoroughly understood. Perceiving the impact of different process parameters on the energetics of heat transfer, melting, solidification, phase transformations among different gaseous, liquid and solid phases, along with the final mechanical state of the weld is paramount to producing lasting weld joints.

Low carbon steels are among the most commonly used materials in manufacturing, because of their superior strength, good workability and cost effectiveness. They comprise over 90 % of the total steel production, therefore, it is crucial to develop feasible methods to easily weld such materials. Furthermore, increasing complexity in product design, advances in materials science and ever increasing fabrication costs are driving the need for more efficient and techno-economical welding solutions. In order to meet these technical challenges and to overcome problems such as, coarse grains in the fusion zone, inadequate weld cleanliness, inability to join thicker plates in a single pass or joining difficult to weld materials, technologies like high energy beam welding and friction stir welding have been developed [5, 6, 7, 8].

In nuclear, chemical and oil industries, electron beam welding (EBW) which is one of the high energy beam technologies, provides the necessary depth to width ratio and narrow heat-affected zones, making it ideal for joining thick sections in a single pass [9]. In the automotive industry, welding design of complex gear transmission parts, crankshafts, piston rods etc. is made easy due to high energy density welding technologies. In its attempt to reduce weight while maintaining strength, the automotive sector has substituted many parts of steel with lighter aluminium alloys. The distinct physical and chemical properties of both these materials led to new challenges in welding and joining them. The fundamental problem with welding such materials is the occurrence of detrimental inter-metallic compounds, that are prone to micro-cracking. Under such circumstances, where fusion welding is found to be critical, friction stir welding (FSW), a solid state welding technology has

proven itself to be an unique and effective solution. Recently, Honda integrated this technology in the assembly lines for welding a vehicles suspension system, claiming enhanced mechanical properties and reduced production costs [10]. In the railway sector, hollow profiles and T-stiffer extrusions used in structural construction of train cars are being friction stir welded to reduce distortion and shrinkage. Hitachi were among the first to use friction stir welded aluminum floor elements in their high-speed train coaches to reduce weight. In the aviation sector, friction stir welding process offered tremendous potential for low cost joining of lightweight aluminum airframes. The European aeronautic defence and space company presented data showing that the mechanical properties of these welds were close to their parent materials [11].

The versatility and applicability of these two welding techniques have made them the primary targets of many a researcher around the globe. In this thesis, an attempt is made at gaining a deeper understanding on the impact of different welding processes on the rapid metallurgy of low carbon steels and to develop a physics based numerical approach to accurately predict residual stresses and distortion in welds.

1.1 Scope of Thesis

The objective of this research is to investigate the influence of process parameters such as electron beam oscillations and tool offsetting (during EBW and FSW respectively) on the thermo-mechanical behaviour of different low carbon steels, and thereby optimize the welding processes. This includes the study of the transient thermal, microstructural and mechanical fields during welding; i.e., temperatures, weld pool dynamics, solidification microstructures, thermal and transformation strains up to the development of final residual stresses. A simple illustration presenting the overview of welding procedure design is shown in the Fig. 1.1. In order to accomplish such a task, a combined experimental and modelling approach was pursued.
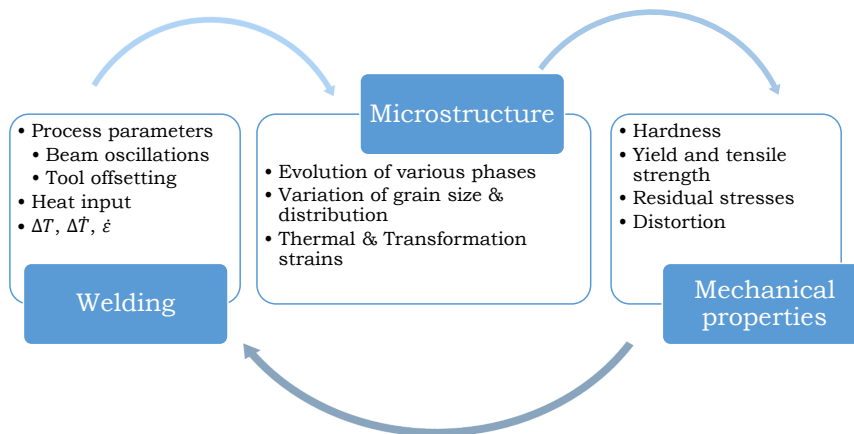

Figure 1.1: Welding process design based on microstructure and mechanical properties of weldments

Comparison against benchmark studies were conducted, to better understand the

differences generated by beam oscillations or tool offset on the microstructure and mechanical properties of the weld joints. Thermocouples were tack welded along the weld line at different positions to soundly map the temperature gradients occurring during both the welding processes. Weld cross sections were cut and their microstructures were studied using optical microscopy, electron back scatter diffraction (EBSD) and other mechanical characterization methods.

In order to obtain accurate predictions from the simulations, a thermal-metallurgical-mechanical model was developed, which included a novel heat source model, temperature-dependent visco-plasticity with isotropic hardening and phase transformations based on cooling rates. The model parameters discussed were either experimentally measured or have been gathered from literature. The results obtained from the simulations were validated through various experimental methods like hole drilling, optical microscopy, electron back scatter diffraction etc. Though the developed model is generic, and is applicable to any welding process, in the scope of this thesis it has been validated only for high energy beam welding methods. The same frame work with some modifications can also be extended to simulate friction stir welding of dissimilar materials.

In this thesis, a high strength dual phase (DP) steel and a deep drawable DC04 steel both possessing 1 mm thickness, a 5 mm thick typical construction steel S235JR and a 1.12 mm thick aged aluminum alloy Al6016-T4 were considered as welding materials due to their wide use across the different sectors of the industry. The following objectives were set

1. Investigate the influence of beam oscillations on the weld geometry, microstructure and mechanical properties (Hardness, yield & tensile strength) of electron beam welded joints.

2. Investigate the influence of tool offset on dynamic recrystallization behaviour, grain refinement/coarsening and strain accumulation during dissimilar friction stir welding of aluminum and steel.

3. Develop a numerical framework to study the thermal, metallurgical and mechanical response (Residual stress and distortion) of weld joints during various welding processes.

4. Simulate the effect of heating and cooling rates on phase transformations, spatial distribution of various phases, their thermal and transformation strains and in turn, the resulting residual stresses during electron beam welding.

1.2 Thesis structure

This thesis presents an experimental and theoretical analysis of the influence of uncommon welding process parameters such as beam oscillations and oscillation trajectory during electron beam welding and tool offsetting during dissimilar friction stir welding, on the weld microstructure and weld mechanical properties of low carbon steels. This work comprises of 5 chapters which are described as follows

- Chapter 2 presents fundamentals of welding and its metallurgy, including a literature review of the current state-of-the-art in welding, experimental method-

ology, characterisation techniques and finite element modelling of high energy beam welding process. Even though the modelling approach presented is tailored to suit electron beam welding, it can also be extended to other fusion welding processes.

- Chapter 3 reports on the experimental results on the influence of afore mentioned uncommon process parameters on the microstructure and mechanical properties of both electron beam welded low carbon steel joints and dissimilar friction stir welded Al-Fe joints. Results and discussions are provided in the form of authors publications in different peer reviewed journals.

- Chapter 4 discusses the fusion zone characteristics, microstructure, hardness and weld strength. It also provides a detailed sequentially coupled thermo-metallurgical finite element model, which was developed based on Abaqus code to predict cooling rate, thermal cycles and the evolution of martensite phase and its effect on the development of residual stresses.

- Chapter 5 gives a brief overview of the major conclusions and findings of this work.

2 State of the art

2.1 Fundamentals of welding

Welding is the art of joining materials together by melting and/or pressing such that a continuity between the work pieces is produced. Taking into account the recent developments including the hybrid approaches to welding, there are currently over 75 different types of welding processes available to a manufacturer. Each of these processes has its own unique advantages and disadvantages that make it suitable to a given application. Arc welding processes offer advantages such as portability and low cost, but are relatively slow and rely on extremely high heat inputs in order to produce welds. High energy density processes such as laser or electron beam welding produce welds with low heat inputs at very high welding speeds, but the equipment needed is expensive and the joint fit-up needs to be near perfect. Solid state welding process such as friction stir welding may avoid weld discontinuities associated with melting and solidification, but are slow, expensive and are often restricted to limited joint designs. Resistance welding processes are typically very fast and require no additional filler materials, but are often limited to thin sheets. Most of these welding processes use some combination of heat and/or pressure; as such have been broadly categorized under either *fusion* welding or *Press* welding. Arc and high energy beam welding processes that do not particularly need the application of pressure, fall under fusion welding. While friction welding methods that rely on pressure and minimal heating fall under press welding. With numerous technologies being available, the choice of a suitable welding technique depends on factors such as the type of materials being welded, required mechanical properties, and needed degree of automation. The increasing demand for better quality at lower costs is forcing the manufacturing sector to adopt systems with high levels of automation. As a consequence, high energy beam welding and friction welding technologies are becoming more relevant due to their high degree of modularity, precision and automation. It is easier to weld thick components with minimal distortion in a single pass with electron beam welding due to its excellent depth-to-width ratio. For difficult to weld materials like aluminum and steel, where the formation of detrimental inter-metallic compounds are observed, friction stir welding provides an effective alternative solution. For these reasons, in this thesis electron beam welding (fusion welding) and FSW (press welding) processes became the focus of investigation.

2.1.1 High energy beam welding

High energy density welding is a fusion welding process that utilizes a heat source capable of providing thermal flux of rather large power density. The energy density in these processes is approximately $10^{10} - 10^{13}$ W/m^2, which is few orders higher than the typical arc welding process where the energy density is about 5×10^8

W/m^2. EBW and laser beam welding are two major types of high energy density welding processes.

EBW is one such fusion welding technique where a narrow beam of electrons is used in welding two pieces of metal. Upon impact with the work piece, the fast-moving electrons penetrate the surface of the material and transfer their kinetic energy to the surrounding atoms in the form of heat, causing localized melting and partial vaporization. A deep cavity is formed due to the intense recoil pressure exerted by the vapour flux on the evaporating surface. The formation of such a cavity or keyhole leads to deep penetration with high aspect ratio. The precise control of the electron beam power density makes it possible to achieve better penetration depths with narrow weld seams and high welding speeds. This is one of the biggest advantages of EBW over conventional welding methods. However, the welding process must be carried out in vacuum in order to prevent the dispersion of the beam. In the presence of a gaseous medium, electrons scatter widening the beam and drastically reducing its power density. Application of EBW is not only limited by vacuum but also by other factors like beam deflection due to retained magnetism in materials, X-ray irradiation and the need for complex tooling. Despite such limitations, it has proven to be advantageous in diverse fields of applications. In the production of turbines for energy and aerospace applications, this technology has aided in reducing production costs and time by substituting large casted parts with welded sub-assemblies. Additionally, due to the fact that the process takes place in vacuum, the formation of detrimental oxides and nitrides in the heat affected zone is effectively eliminated which enhances the durability of joints. In the automotive industry, it is particularly useful in welding gear transmission parts, crankshafts, piston rods, valve heads and others. In nuclear, chemical and oil industries, EBW provides the necessary depth to width ratio and narrow heat-affected zones, making it ideal for joining thick sections in a single pass [12].

Laboratory scale welding trials were conducted on steel blanks of sizes 150 × 100 × t (t is 5mm for S235JR steel and 1mm for DP steel). Autogenous welding, without the use of welding consumables and preheating was carried out. The beam was focussed on surface of the work pieces being butt welded in the PA position using a universal chamber EBW machine of type K7 made by Probeam (Germany). As the work pieces were cut using shear cutter, their edges were carefully prepared to remove any irregularities and ensure a perfect fit between them. Welds were produced in a single pass. Temperature was recorded with the help of wire shaped thermoelements that were spot welded at various points around the weld line. Furthermore, welding was carried out in vacuum and no external cooling was employed in the chamber. The weld set up, various welding parameters and required settings can be found in chapter 3, section 3.1.

2.1.2 Friction stir welding

FSW is a solid state welding process that uses frictional heat to create joints. A non-consumable cylindrical tool with a shoulder and a profiled pin is rotated and plunged into work pieces that are either butted or lapped together. The heat generated due to the frictional contact causes material to soften and the rotational forces exerted on the material by the tool, lead to the mixing of both materials and creates a solid

phase weld. This method was developed by the welding institute especially for joining aluminum alloys, however over the course of various studies it has proven to be advantageous in welding difficult to weld materials such as aluminum and steel. Fundamentally, when welding aluminum and steel via conventional fusion welding methods, brittle Al-Fe intermetallic compounds (IMC) are obtained. These IMCs are detrimental to the weld joints service and longevity. By applying FSW, where melting of work pieces is prevented, a superior bond can be established between those materials.

In this study, dissimilar blanks of Al-Fe were butt welded using a position controlled friction stir welding machine. The welding equipment comprised of a conventional three-axis numerically controlled milling machine, with a maximum spindle power of 7.5kW, a tungsten carbide tool cemented with cobalt and special clamping system. Aluminum blanks were placed on the retreating side to enhance material flow. Primarily the influence of various welding parameters on the underlying metallurgical phenomena such as dynamic recrystallization of aluminum, grain refinement and strain accumulation were studied in the welded joints.

2.2 Materials

Low carbon steels and an aged aluminum alloy were utilised for studying the unconventional parameters of the two welding processes. The chemical composition of the alloys is listed in Table 2.1. The hot rolled S235JR structural steel is an im-

Table 2.1: Chemical composition in weight % of alloys used in this study

Element	C	Si	Mn	P	S	Mg	Cr	Ni	Cu	Al	Ti	N
S235JR	0.075	0.054	0.94	0.0264	0.001	-	0.393	0.039	0.022	0.026	-	0.012
DP1000	0.082	0.315	2.50	0.0145	0.002	-	0.685	0.022	0.101	0.032	0.076	0.0141
DC04	0.008	0.008	0.19	0.008	0.005	-	0.015	-	0.007	0.0037	0.029	-
Al6016-T4	-	1.31	0.06	-	-	0.32	0.001	-	0.009	98.07	0.01	-

pact tested, low carbon ferritic steel grade widely used for structural applications like construction of bridges, penstocks, pipes and offshore structures [13, 14]. In the as-obtained state, it consisted of approximately 10% pearlite and 90% ferrite microstructure. It provided an yield and a tensile strength of 310 MPa and 414 MPa respectively. The dual phase DP1000 is an advanced high strength steel that offers impressive mechanical properties like the absence of yield point elongation, high work hardening rate and high ultimate tensile strength [15, 16, 17]. These unique characteristics of DP steels are vastly sought after in the automotive industry, to reduce weight and improve passenger safety [18, 19]. DP steels derive strength from their complex microstructure, comprising of hard martensite islands dispersed in soft ferritic matrix [20, 21]. In the as obtained state, it consisted of approximately 40% martensite and 60% ferrite phase fractions. It exhibited an yield strength of 740 MPa and tensile strength of about 1000 MPa. whereas, hot rolled deep drawable DC04 steel is widely used for structural and chassis parts of automobiles due to their excellent formability and good ageing resistance. It consists of purely ferritic microstructure with embedded carbides and exhibits an yield strength of 220 MPa and a tensile strength of 350 MPa. Besides low carbon steels, the Al6016-T4 aluminum alloy was also investigated to study the dissimilar friction stir welding

process. In the recent past, aluminum alloys have attracted considerable attention from the automotive industry to design lightweight vehicles with improved fuel efficiency and reduced emissions. Heat treatable Al-Mg-Si alloys are of particular interest due to their good formability, high strength, excellent corrosion resistance and weldability. The dimensions of all the work pieces obtained were selected such that a quasi-steady state during welding could be maintained and to have sufficient materials for mechanical and metallurgical analyses.

2.3 Weldability of steel

The weldability of a steel is a measure of its resistance to cracking during & after welding, and in service. It is desired that the weld joint offers adequate strength and resistance to brittle and ductile crack propagation. If this tendency is easily obtained in a steel, it is deemed to be weldable. Typically, the base material (BM) near the fusion line experiences temperature above the Ac_3 and transforms into austenite during the heating cycle of welding. As the weld cools, this austenite decomposes into different new structures depending on the cooling rate, alloying content and initial microstructure of the BM. If the final weld microstructure contains phases that are extremely brittle and hard, it is prone to failure due to cracking. It is known that, high concentrations of carbon and other alloying elements such as Mn, Si and Ni tend to increase hardenability and decrease weldability of a steel. For ease, a carbon equivalent value (CE), is used to determine how the alloying content affects the weldability of a steel. By varying the amount of carbon and other alloying elements in the steel, the desired strength levels can be achieved by proper heat treatment. A better weldability and low temperature notch toughness can also be obtained. Ito-Besseyo [22] presented the following equation to calculate the CE for low carbon steels

$$CE = C + \frac{Mn + Cr + Cu}{20} + \frac{Si}{30} + \frac{V}{10} + \frac{Mo}{15} + \frac{Ni}{60} + 5B \qquad (2.1)$$

where the alloying elements are expressed in wt. %. It is recommended that the CE value be less than 0.25 when using the above equation. Steels with CE values in excess of 0.41 are not easy to weld and need preheating prior to welding. Dual phase (DP), S235JR or DC04 steel are steels with low CE values (<0.25) and provide good weldability and toughness.

2.4 Weld microstructure

As state earlier, the microstructure that develops after welding is influenced by the process parameters, the chemical composition of the alloy and the heating and cooling rates experienced by the weldments. Upon a closer examination of a fusion welded cross section, three distinct zones can be observed as shown in the Fig 2.1. The unaffected base metal (BM), the heat affected zone (HAZ) and the fusion zone (FZ). In the case of FSW joints, besides weld zone (WZ) and HAZ, an additional thermo-mechanically affected zone (TMAZ) can be found.

2.4.1 Heat affected zone

The HAZ is the area between the fusion line (FL) and the BM. It is a portion of the BM that experienced temperatures that are below the melting point, but are high enough to change its microstructure and alter its properties during welding. The microstructure of HAZ depends on the peak temperature attained and the length of time spent between the temperature range of 800 to 500 °C. It may contain martensite, bainite or coarse pearlite phases. The HAZ typically consists of four different microstructural zones, (i) coarse grain heat affected zone (CGHAZ) where grain growth takes place during weld thermal cycles, (ii) Fine grain heat affected zone (FGHAZ) where recrystallization takes place (iii) inter-critical heat affected zone (ICHAZ) where microstructure is partially transformed and (iv) sub-critical heat affected zone (SCHAZ) where the BM is tempered. The CGAHZ resides next to the fusion line and experiences temperature above the Ac_3 and therefore austenite grain growth occurs. The grain size and width of the CGHAZ increase with increasing heat input and low cooling rates [23]. In the FGHAZ the temperature is high enough to trigger austenite transformation but does not support substantial grain growth, as such fine austenite grains nucleate and grow around the existing lath or grain boundaries. Due to such behaviour grains typically smaller than that of BM are observed. The ICHAZ, is a partially austenitized. Only part of grains undergo austenite transformation and transform into martensite. Finally in the SCHAZ, the peak temperature is below the AC_1 and the grain size is not affected. However, the existing microstructure is subjected to an indirect tempering leading to a decrease in strength. The mechanical properties of each of the HAZ are different due to the considerable variation in their microstructures. The hardness of different HAZ regions varies gradually declining from the FL to the SCHAZ. In general, when moving across the HAZ, from the BM toward the FL, the peak temperature experienced increases and so, likewise, the austenite grain size and hardenability increase. High hardness values usually correlate with increased brittleness and reduced ductility.
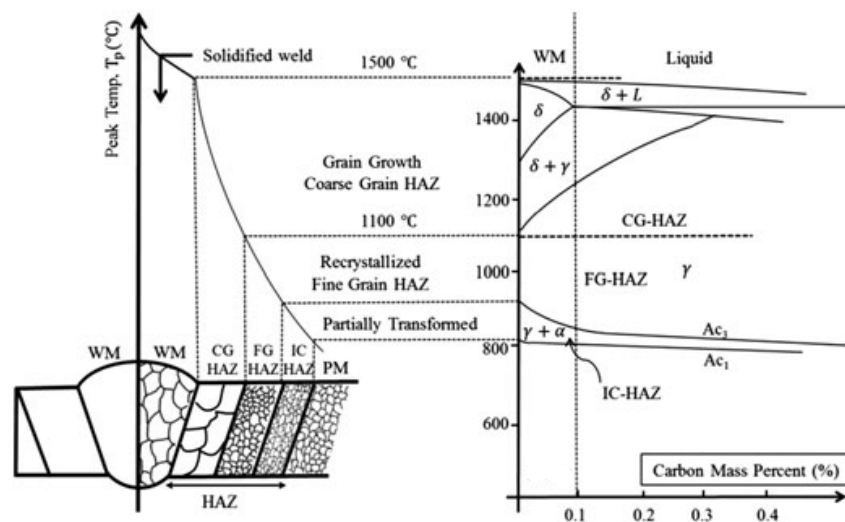

Figure 2.1: Variation of weld microstructure in correspondence with equilibrium Fe-C binary phase diagram [24]

2.4.2 Fusion zone

The weld metal is the fusion zone which on cooling solidifies and creates a bond between the two work pieces. It consists of a columnar solidification microstructure similar to *as cast* structures [25]. The ASM hand book on welding [26], described the evolution of this columnar microstructure as epitaxial growth because the solidifying grain is a continuation of the base metal grain at the fusion boundary. The columnar grain size and shape can be changed by altering the weld pool shape. The weld metal grains will grow epitaxially from the pre-existing base metal grains, however not all grains will be favourably oriented for continued growth. Two factors control the competitive growth of the weld metal grains, (i) grains tend to grow in the direction that is anti-parallel to the direction of heat extraction, (ii) grains choose the easy growth crystallographic directions. The first criterion results from the need to transport the latent heat of solidification down the temperature gradient into the cooler base metal. Because the temperature gradient is highest in a direction perpendicular to the solid/liquid interface. The second criterion results from the preferred crystallographic growth direction, which for cubic materials is [100] direction. Both these phenomena together account for the columnar grain zone that is often observed in castings. This situation is slightly more complex in welding, because the pool shape produces a curved solid/liquid interface that is constantly in motion. Grains at the fusion line may initially be oriented in a favourable direction but it become unfavourable as the curved solid/liquid interface changes its position. Here the melt pool shape also has a strong influence on the competitive growth and the resulting grain structure. In turn the melt pool shape is can be influenced by the welding parameters. At low to moderate welding speeds, the melt pool shape is elliptical and produces the grain structure as shown in the Fig. 2.2b. At higher travel speeds the melt pool takes the shape of a tear drop where the solid/liquid interface is straight. This elongated shape is attributed to the low thermal gradient and high growth rate that exists at the centre of weld line.
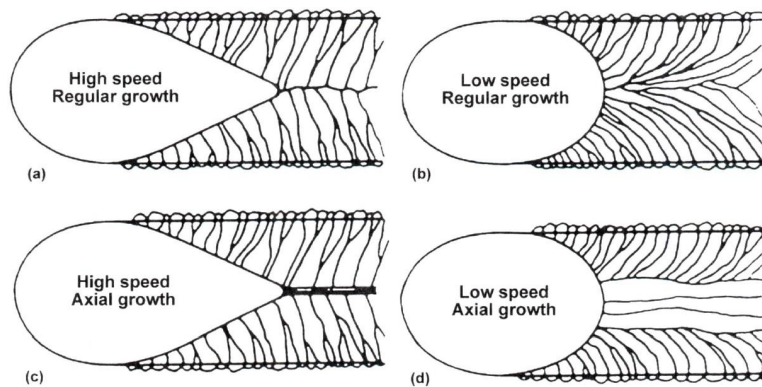

Figure 2.2: Grain morphologies that form from different weld pool shapes [26]

2.4.3 Stir zone

The material in WZ is exposed to both heat and severe plastic deformation. The maximum temperature in the FSW process occurs in this zone. Typically depending on the material and process parameters, 90 - 95 % of the materials melting temperature is achieved. Due to such high temperatures and deformation dynamic recrystallization of microstructure takes place and results in fine equiaxed grains. Also due to the dynamic balance of material movement under the tool, materials layers that appear as ring structures are typically seen.

2.4.4 Thermo-mechanically affected zone

The unique feature of FSW is the creation of such a region where the base metal is affected by mechanical operations. This area experiences plastic deformation and heat together which leads to highly deformed elongated grain structures. However, conditions are not entirely suitable for the complete dynamic recrystallization of the microstructure. In some cases however, partial recrystallization has been observed.

2.5 Weld joint characterization

It is vital not only to observe the weld joints appearance but also to evaluate the mechanical performance of the weld. Depending on the application, weld joints are qualified according to a suitable standard. It is however typical among most standards to observe the microstructure, hardness distribution and other mechanical properties against different types of loading. The following characterization methods were utilised to analyse the weld joints.

2.5.1 Metallography

It is essential to study the macro/microstructure of the weld joint to observe weld errors such as pores, cracks and lack of fusion etc. As these factors are mainly responsible for the weld performance and lifespan. Additionally grain size, segregations, inclusions and presence of various phases could also be recognized through metallography.

Specimens were cut along the weld line such that the fusion zone, the heat affected zone and part of the base material are contained in a single specimen. These specimens were then ground and polished to obtain a flat and shiny finish. In polished state samples are investigated for lack of penetration, porosity, shrinkage cavities, cracks and other inclusions. The specimens are then subjected to an etching operation using a suitable reagent that reveals the microstructure of the specimen. The medium and duration of etching depends entirely on the material studied. For steels considered in this study, 10% nitric acid diluted in ethanol (Nital) was used to reveal the microstructure of the welds.

In multiphase steels with complex microstructures, identifying the various phases could be challenging. For such cases, electron back scatter diffraction (EBSD) technique was utilized to quantify the various phases and other minute artefacts at higher resolutions. Besides mechanical grinding and polishing, samples are further

electro-polished to smoothen any remaining artefacts. In this study EBSD maps were acquired on a schottky field emission gun scanning electron microscope equipped with a Hikaki camera and TSL OIM software. An accelerating voltage of 20kV, step size of 100nm on a hexagonal grid and a dwell time of 7 ms were used for the measurement. After dynamic back-ground subtraction, the intensity of diffraction patterns was normalized and points of confidence index less than 0.1 were discarded. Grains were limited to a $5°$ misorientation criterion and kernel average misorientation was calculated over a distance of 100nm to investigate the microstructures of welds.

2.5.2 Hardness

Hardness testing of welds and their heat affected zones usually requires testing on a microscopic scale using an indenter. It provides an indication of two parameters significant to the determination of a successful weld joint, strength and microstructure of a known material. It is known that tensile strength of a crystalline material is proportional to its hardness. Typically for common steels, the tensile strength can be estimated simply by taking a third of its Vickers hardness multiplied by ten. For the carbon steels under consideration, the microstructure can vary from ferrite and pearlite through to bainite and martensite. The propensity for any microstructure to form, is a function of alloy content and cooling rate. Welding imposes a variety of thermal cycles that could result in undesirably hard microstructures that could undergo brittle fracture or excessively soft microstructures susceptible to plastic collapse under load. Single pass welds tend to be harder than multi-pass welds due to the lack of tempering inherent to multi-pass welding. The hardness therefore can be a useful indicator to determine if the thermal cycle induced by welding has rendered the heat affected zone of the weld susceptible to cracking or plastic collapse.

In this study Vickers hardness of the weld cross sections were measured at evenly spaced points across the weld covering the fusion zone, heat affected zone and part of base material. Micro-indentations were made using a load of 100 g with a dwell time of 5 s. For multiphase steels, a load of 100 g was used to keep the inter-indent spacing to a minimum of 0.1 mm. The applied load was found to be sufficient and provided good quality indents for analysis.

2.5.3 Tensile and bending tests

For design purposes, it is essential that the limiting value of stress, a structure can withstand without failure is known. Welding processes introduce significant alterations to the microstructure of the welds and as such, they tend to exhibit varying mechanical properties across the different weld regions. Uni-axial tensile tests are carried out on the welded joints to determine their potential. For this study, tensile test samples were cut along the rolling direction such that the weld line was positioned exactly at the centre of gauge length. As per the standard EN 4136:2013, quasi-static tensile tests were performed using a 100 kN load cell and a strain rate of 0.001/s. To ensure repeatability, a minimum of 3 specimens were tested in each weld condition. In order to map the strain distribution in the FZ and the HAZ, digital image correlation (DIC) technique was used during the tests. A speckle pattern consisting of white and black spots was created on the sample surface that enable

the DIC system to capture data. A high speed camera was employed to take series of pictures during deformation which were later analysed using the GOM software to obtain the strain maps of the welds. After the sample fails in the test, the failure location is tracked to understand if the weld exhibited an overmatching or an under matching strength. It is typically desired that welds are stronger than the base materials and the failure should occur in the base material away from the weld.

Three point bending tests are performed on welds in order to determine their flexural strength. In bending both tensile and compresses are induced over the cross section of the weld along with minor shear stresses. Bend testing allows for the determination of ductility, bend strength, fracture strength and resistance to fracture of a weld. These characteristics are useful in determining whether a weld will fail under pressure. It is especially important in any construction process involving weld joints loaded with bending forces. If a weld begins to fracture or completely fractures during a three or four point bend test, it is valid to assume that the weld joint will fail under a similar loading conditions, leading to the catastrophic failure of the entire structure. Also, a successful bend test indicates that weld itself has fused properly and does not contain any defects that could lead to failures.In this study, as per the standard EN 5173:2010 face and root bend tests were performed on the welds to quantify their ductility and flexural strength. A 50 kN load cell and a constant bending speed of 2 mm/s were used during the test. The three-point bending test setup, with 50 mm outer span, 100 mm inner span and the tool radius of 5.5 mm, along with the sample geometry is presented in 3. The electrical signal obtained from the transducer and strain gauge provided the required force and displacement data.

2.5.4 Dilatometry

welding involves heating and cooling cycles that result in melting, solidification, phase transformations, grain growth, tempering etc. Steels undergo not only solid to liquid phase transformations during welding but also solid-solid phase transformations like decomposition of austenite into martensite, bainite and ferrite during cooling. These transformations are controlled by the alloying content and the heating or cooling rates. Dilatometry aids in studying the phase transformation kinetics of such phases. However, melting and solidification cannot be simulated by a dilatometer. Cylindrical or flat specimens are obtained from the base material and subjected high heating and cooling rates that are comparable to that of heat affected zone of the weld joint. The cooling rates are controlled by flooding the test chamber with various inert gases like helium or argon. The relative change in length of the specimen is acquired with the help of a laser measurement system that continuously records the non-linear expansion and contraction of samples during solid state phase transformations.

2.5.5 Hole drilling test

The welding process causes a highly non-uniform heating of the parts being joined. Areas close to the weld are heated up above the melting temperature, and then cooled down, the heat being conducted to the bulk of the body. This local heat-

ing and subsequent cooling induces volumetric changes producing temporary and permanent stresses; i.e., residual stresses.

Hole drilling is a destructive testing method applied in order to analyse those residual stresses in the weld joints. It involves drilling a blind hole in the specimen and measuring strain in the vicinity of the hole. Electronic speckle pattern interferometry is employed to track distortion inside the hole, that arises from the relaxation of internal stresses after material is removed by drilling. The specimens surface is illuminated with coherent laser light and analysed by a camera system. The surface roughness naturally projects a speckled pattern, as light reflected from a rough surface interferes either constructively or destructively creating a speckled pattern of bright and dark areas in the image. A change in this speckle pattern due to stress relaxation creates a shift in the image that enables the measurement of strain. The stress is measured by correlating the strains (ϵ), the elastic modulus (E) and the Poissons coefficient (ν) as below

$$\sigma_{ij} = \frac{E}{(1+\nu)}\epsilon_{ij} - \frac{\nu E}{(1+\nu)(1-2\nu)}\delta_{ij}\epsilon_{kk} \tag{2.2}$$

$$\epsilon_{ij} = \begin{bmatrix} \epsilon_{11} & \epsilon_{12} & \epsilon_{13} \\ \epsilon_{21} & \epsilon_{22} & \epsilon_{23} \\ \epsilon_{31} & \epsilon_{32} & \epsilon_{33} \end{bmatrix}$$

The elastic modulus and the Poissons coefficient for steel are taken as 210 GPa and 0.3 respectively.

2.6 Finite element modelling

The advancements that computational sciences in the recent decades, it has become easier to simulate material behaviour during and after processing. Although simulating welding is still plagued with limitations, using appropriate boundary and initial conditions, the degrees of freedom of higher order differential equations could be reduced and a satisfactory solution could be obtained. Finite element methods, spectral element methods or finite difference schemes have provided the ability of addressing complex multiphase field problems like welding. To fully understand the material behaviour and predict residual stress arising from welding, a set of partial differential equations that describe the various underlying physics such as heat transfer, mass transfer, phase transformations, transformation stress and strain evolutions must be solved.

The simulation procedure involves a sequential coupling of heat transfer and a mechanical analysis. With no other loading than thermal expansion and contraction the deformation of a weld solely depends on the temperature field and history. As the internal heat generation arising from the plastic dissipation and the mechanical work done, is insignificant in comparison to the thermal flux produced during welding, the thermo-mechanical behaviour of the welded structure was simulated using a sequentially coupled formulation. The transient temperature distribution was solved independently from the mechanical stress problem. It is a challenging task to precisely map the temperature distribution during electron beam welding, especially at points present in close proximity to the keyhole. Therefore, a moving

volumetric heat source model that is representative of the electron beam was developed. The mathematical description of the heat source encompasses a distributed heat flux in order to obtain the temperature distribution. Dflux routine was utilized in defining the thermal flux distribution over a section of the finite element model. Furthermore, the time-temperature history and the evolution of various phase fractions recorded at each node in the FE mesh during the uncoupled heat transfer analysis were employed as thermal load and initial material state in the subsequent residual stress analysis. The thermal and transformation strains calculated in the Uexpan subroutine were then returned to the solver as thermal expansion coefficients during the stress analysis.

For friction stir welding however, a contact problem must be defined. As heat is generated due to frictional contact is accompanied by plastic dissipation, a thermal flux model would not be sufficient to describe the heat generation. Additionally the plastic straining must also be taken into account. The approach mentioned before could well be adopted but, in addition to the time-temperature history, the strain parameter must also be saved. In this thesis, a frame work of thermal, metallurgical and mechanical analyse is presented only for fusion welding methods, however it could be extended for press welding by including the additional strain parameter.

2.6.1 Metallurgical model

Phase transformations in steels are driven by the difference in Gibbs free energy between the parent and product phases. This free energy for transformation can be defined as function of composition, stress/strain state and temperature [27]. Majority of phase transformations occurring in steels are thermally activated and are accompanied by the diffusional movement of atoms, also known as reconstructive/diffusional transformations. Under rapid cooling conditions however, such diffusional movement of atoms can be hindered and transformation can proceed in a displacive manner where the coordinated movement of atoms in the lattice produces a product phase with identical composition as the parent phase. These diffusional or displacive phase transformations are always accompanied by volumetric dilatations that arise from heterogeneities in the distribution of alloying elements and create local stress fields in the welded structures. High peak temperatures produce dendrites in the FZ, coarse to fine grained microstructures in the HAZ.

2.6.1.1 Austenitization

Austenitization is a non-isothermal process that occurs during the welding thermal cycles. When DP steels are heated above their Ac_1 temperature, face centred cubic structured austenite nucleates in the martensite phase, preferentially at the lath boundaries and continues to grow until the Ac_3 temperature is reached. Assuming that the transformation occurs by the nucleation and growth of a new phase, the kinetics of transformation and the evolution of phase fractions can be postulated using the Johnson-mehl-Avrami-Kolmogrov (JMAK) approach [28].

$$V_\gamma = 1 - \exp\left[-kt^n\right] \tag{2.3}$$

where V_γ is the austenite fraction, k and n are the material parameters and t is the time. Caballero et al. [29] introduced a heating rate dependent austenitization model for two phase microstructures that is also based on the nucleation and growth of a new phase. Though the model was developed for ferrite and pearlite steels, it can be adopted to DP steels. The nucleation and growth of austenite in martensite phase can be described as

$$V_\gamma^m = V_{m_0} \left[1 - \exp \left(\frac{4\pi}{3\dot{T}^4} \dot{N} G^3 \Delta T^3 \right) \right] \tag{2.4}$$

where V_{m_0} is the initial martensite fraction and $\dot{T}$ is the heating rate obtained during welding. The nucleation rate $\dot{N}$ and growth rate G were expressed as a function of their respective activation energies (Q_N, Q_G) as below

$$\dot{N} = f_N \exp \left(\frac{-Q_N}{k\Delta T} \right) \quad \& \quad G = f_G \exp \left(\frac{-Q_G}{k\Delta T} \right) \tag{2.5}$$

The fitting parameters f_N, f_G along with the activation energies for dual phase steels were taken from the study published by Thiesen et al. [30]. The kinetics of ferrite to austenite transformation after the conversion of martensite is expressed as

$$V_\gamma^\alpha = \begin{cases} V_{\alpha_0} \left[1 - \frac{5.6\dot{T}}{6\times10^{-12}V_{\alpha_0}(T-T_C)^{5.6}+5.6\dot{T}} \right] & \text{for} \quad T_C < T < T_D \\[4mm] V_{\alpha_0} - \frac{(V_{\alpha_0}-V_D^\alpha)\dot{T}^2}{\dot{T}^2+1.2\times10^{-3}(V_{\alpha_0}-V_D^\alpha)[(T-T_C)^2-(T_D-T_C)^2]} & \text{for} \quad T \geq T_D \end{cases}$$

where V_{α_0} is the initial ferrite fraction, T is the current temperature and T_C & T_D are the transformation temperatures determined experimentally by means of dilatometric analysis as shown in Fig 2.3a.

2.6.1.2 Melting & solidification

In a typical phase diagram, above the solidus line and below the liquidus line, there exists a two phase region where at different temperatures varying fractions of solid and liquid phases can be seen (see Fig. 2.3b). In the welding process, the cooling rates are too rapid to allow substantial diffusion of alloying elements in the solid phase therefore, a local equilibrium can be assumed at the solid-liquid interface. Thus the well known lever rule was employed to predict the volume fractions of liquid and austenite at temperature (T) during melting and solidification as shown below

$$V_L(T) = \frac{(T - T_A)/m_a}{(T_A - T)/m_a + (T_L - T)/m_l} \tag{2.6}$$

$$V_S(T) = \frac{(T_L - T)/m_l}{(T_A - T)/m_a + (T_L - T)/m_l} \tag{2.7}$$

where V_l, V_s are the liquid and solid volume fractions, T_l, T_a are the liquidus and solidus temperatures, m_l, m_a are the slopes of the liquidus and solidus lines obtained from the Fe-C phase diagram.

(a) Dilatometer curve showing the austenite start (T_C) and finish temperatures (T_D)

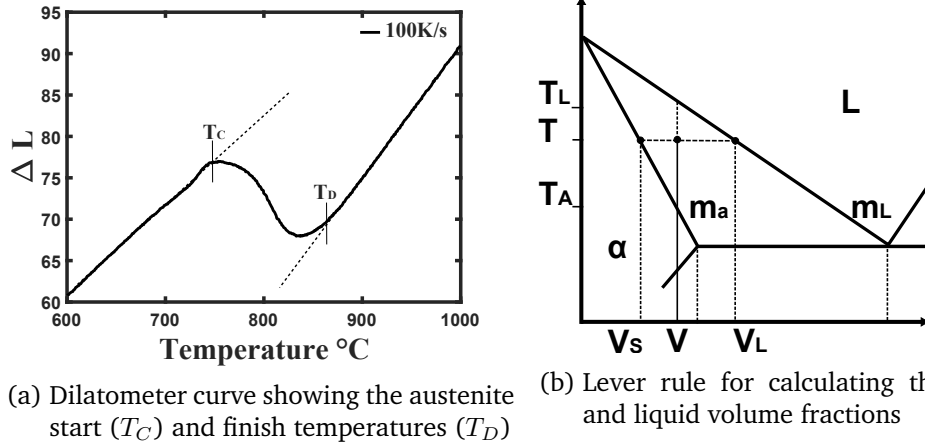(b) Lever rule for calculating the solid and liquid volume fractions

Figure 2.3: (a) Dilatometer curve showing the austenite start and finish temperatures; (b) Lever rule to calculate the solid and liquid fractions at any temperature in the two phase region

The melting function however, does not contribute towards the prediction of residual stresses. In molten state, the weld does not contain any considerable stresses. Nevertheless, it aid in estimating the dimensions of melt pool and also in establishing a verification function where, the sum of all the phase fractions at any instance must equal 1.0. As the different equations in the metallurgical framework are not explicitly coupled, it is necessary to perform such checks at regular intervals during the simulation.

2.6.1.3 Martensite transformation

During the rapid cooling process the face centred cubic austenite phase does not have sufficient time to rearrange itself into body centred cubic lattice, therefore in an attempt to lower its free energy state, the austenite lattice shears into a body centred tetragonal structure trapping the interstitial carbon atoms in the process. This austenite to martensite transformation is athermal in nature and is accompanied by large volumetric dilatation. This is one of the prime reasons for the generation of residual stresses in the weld joint. The level of residuals can be directly correlated to the volume fraction of martensite formed in the weld. The well known Koistinen–Marburger relationship [31] was used to describe the martensite transformation.

$$V_m = V_\gamma(1 - \exp[-b(M_s - M_f)]) \quad (2.8)$$

where V_m is the martensite volume fraction, V_γ is the existing austenite fraction, M_s and M_f are the martensite start and finish temperatures. The M_s and M_f were obtained from the dilatometer test (see Fig. 2.4) where samples were heated to a temperature that is 50 °C above the AC$_3$ and then quenched in the test chamber with Argon gas. To obtain the start and finish temperatures of just the martensite phase such a test was carried out. However, martensite in dual phase steel is obtained after an inter critical annealing treatment and it exhibits different carbon solubility. As a result the M_s and M_f temperatures might vary in comparison to the experimental
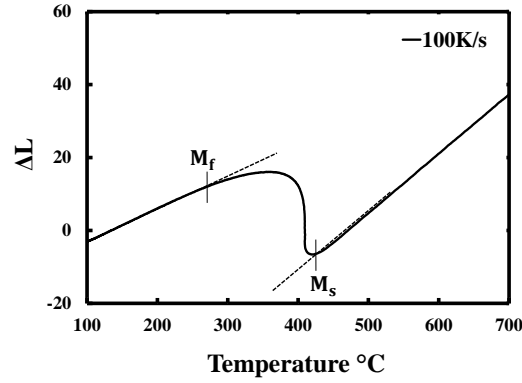
results.

Figure 2.4: Martensite start (M_s) and finish (M_f) temperatures of Dual phase steel

2.7 Thermal-metallurgical-mechanical coupling

The estimation of welding induced residual stress using finite element methods has been gaining attention because of its ability to consider realistic boundary conditions, temperature dependent material properties and complex weld joint geometries. An adequate representation of the heat source model and accurate estimation of the temperature fields is paramount to predicting the kinetics of phase transformations and the evolution of thermo-mechanical strains during the heating and cooling cycles of the welding process. Assuming an isotropic simulation domain with temperature dependent heat transfer, the heat flux introduced by the moving volumetric heat source was resolved using Fourier's law

$$\frac{\delta}{\delta x}\left(k\frac{\delta T}{\delta x}\right) + \frac{\delta}{\delta y}\left(k\frac{\delta T}{\delta y}\right) + \frac{\delta}{\delta z}\left(k\frac{\delta T}{\delta z}\right) + Q = \rho c \frac{\delta T}{\delta t} \tag{2.9}$$

where Q is heat flux per unit volume, k is conductivity, T is temperature, ρ is density and c is specific heat capacity of the material. The thermo-physical data of dual phase steels is listed in the appendix **??**. The time-temperature data obtained during heat transfer simulation was utilized to study the influence of peak temperature, heating and cooling rates on the various phase transformations taking place during welding. The metallurgical models presented in this paper considered the above mentioned factors in describing the evolution of various phases. The total volumetric dilatations arising from the thermal and transformation strains of each phase were captured in the form of a dilatation coefficient as follows

$$\beta = V_\alpha \beta_\alpha + V_{\alpha'} \beta_{\alpha'} + V_\gamma \beta_\gamma \tag{2.10}$$

The term β represents the combined thermal and transformation strains arising from all the existing phases. V_α, $V_{\alpha'}$ and V_γ are the volume fractions of ferrite, martensite and austenite phases calculated from the metallurgical models as discussed previously. Pan et al. [32] reported on the thermal stress and volume change of carbon

steels. It was reported that the austenite dilatation ($\beta_\gamma = 23 \times 10^{-6}$) remains constant with temperature, while the volumetric dilatation of martensite was found to increase with increasing temperature and decreasing carbon content. For low carbon steels an average value of $\beta_{\alpha'} = 15 \times 10^{-6}$ for martensite and $\beta_\alpha = 12 \times 10^{-6}$ for ferrite phases were suggested.

Furthermore, the formation of martensite, is accompanied by plastic accommodation of laths within the martensite islands. This deformation however is insignificant in comparison to the strains induced in the BM adjacent to the weld regions. Therefore, it can be assumed that the deformation of martensite in the FZ and HAZ is only elastic in nature while, in rest of the BM, especially the ferrite phase undergoes significant plastic deformation. Authors have investigated the temperature dependent elasto-plastic properties of DP steels with the aid of hot tensile tests in their previous study [33]. The stress-strain data obtained from those experiments were utilized in the current study to estimate the residual stresses in the weld joint.

2.8 Implementation

The volumetric heat source models and metallurgical models described in the previous sections have been implemented in ABAQUS [34] using various user subroutines. The flow chart shown in Fig. 2.5 presents an overview of the simulation approach. Firstly, the transient temperature field is calculated using the heat source model with thermal boundaries such as radiation, convection and conduction. As the material behaviour is temperature dependent, it is affected by the temperature field. The time-temperature data including the heating and cooling rates observed in the uncoupled heat transfer simulation are utilized to predict the various phase transformations and their spatial distributions, and thereby capture the various thermal and transformation strains. Finally the residual stress and distortion are calculated in the mechanical analysis.
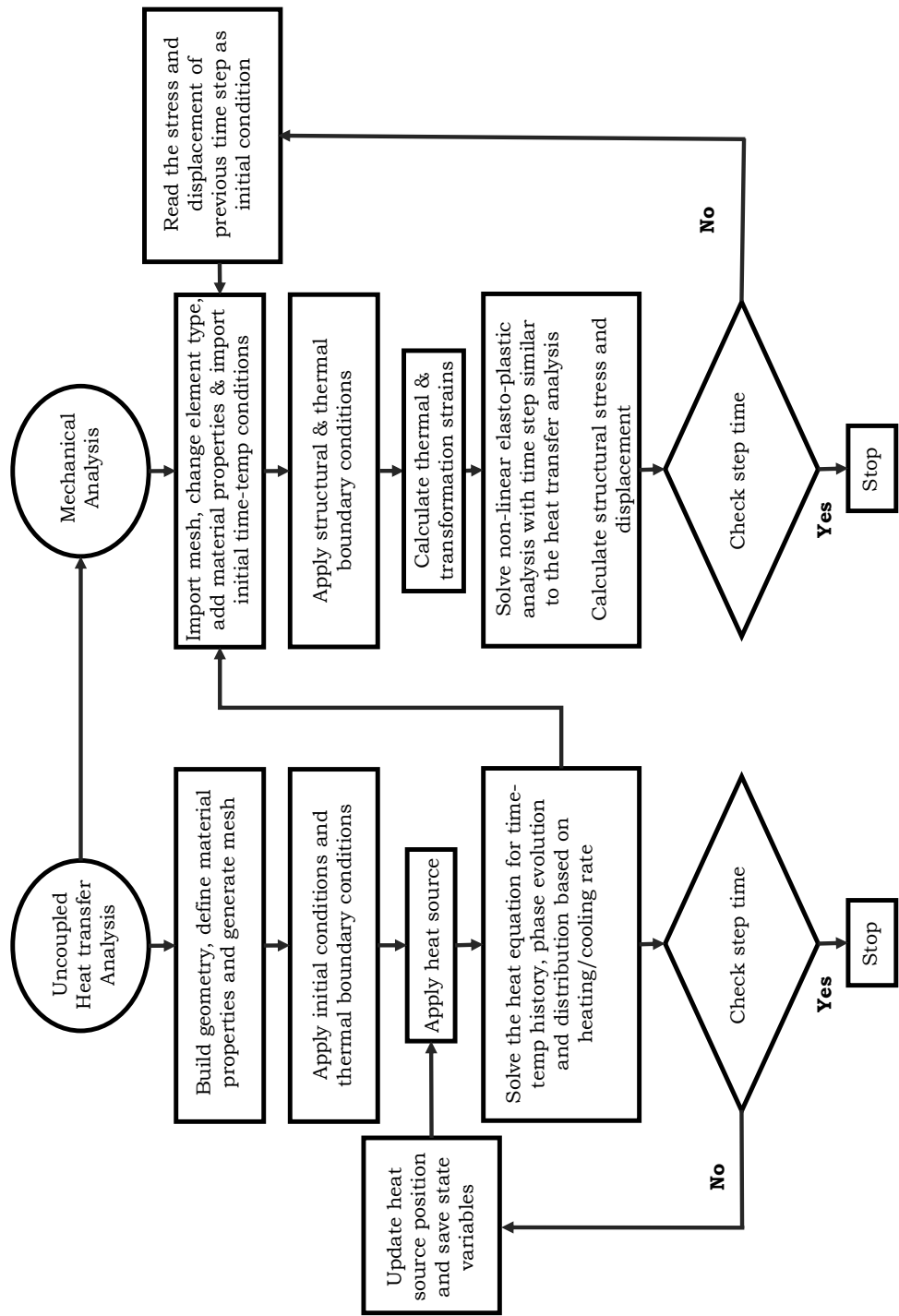
Figure 2.5: Flow chart illustrating the sequential coupling of thermal and mechanical analyses

3 Results

In this chapter, a detailed account on aspects such as, weld geometry, microstructure, micro-hardness, tensile and bending properties of the welds is presented. It is evident from the results that, the welding process parameters play a huge role in controlling the development of weld microstructures and thus are directly responsible for the final mechanical response of the welded component. A scientific approach based on experimental metallurgy, microstructural characterization and numerical simulations that tends towards the improvement of weld quality and longevity of weldments is described.

Furthermore, a physics based modelling approach aimed at optimization of welding process parameters is also presented. As part of the task, a novel volumetric heat source model that is representative of a high energy beam was developed along with a metallurgical framework, that describes the underlying material mechanics. Established empirical models were put to use in order to quantify the evolution of various phases and their distribution in the weld. With the help of user subroutines these models were integrated into a commercial FE software in order to predict the thermal, metallurgical and mechanical behaviour of the weld joints.

3.1 Publication I

The Effect of Beam Oscillations on the Microstructure and Mechanical Properties of Electron Beam Welded Steel Joints
K. Komerla, S. Gach, T. Vossel, A. Schwedt, A. Bührig-Polaczek, U. Reisgen, W. Bleck (2019), The International Journal of Advanced Manufacturing Technology 102:1–13. https://doi.org/10.1007/ s00170-019-03355-4.

Highlights

- Beam oscillation along a circular trajectory was found to create a stirring effect in the key hole, that results in better mixing and minimizes segregations in the weld

- The study revealed that low frequency beam oscillations do not significantly alter the morphology of the weld microstructure and aid in lowering hardness and residual stress, while enhancing tensile properties of the weldments

- The control of penetration depth achieved through beam oscillations produces welds with minimal weld undercuts/crowns and improves finish.

ORIGINAL ARTICLE

CrossMark

The effect of beam oscillations on the microstructure and mechanical properties of electron beam welded steel joints

Krishna Komerla[1] · Stefan Gach[2] · Thomas Vossel[3] · Alexander Schwedt[4] · Andreas Bührig-Polaczek[3] · Uwe Reisgen[2] · Wolfgang Bleck[5]

Abstract

The influence of beam oscillations on the microstructure and mechanical properties of low-carbon steels, subjected to electron beam welding, was investigated. Beam oscillations created a dynamic distribution of power around the stationary position of the beam resulting in the enhanced flow of heat inside the keyhole and yielded wider fusion and heat-affected zones. A reduction in the undercutting at the weld root was also achieved through beam oscillation. The weld microstructure consisted of large columnar grains in the fusion zone and equiaxed grains of varying sizes in the heat-affected zone. The variation in grain size across the weld joint was attributed to the steep temperature gradients produced during electron beam welding. High hardness was seen in the fusion and heat-affected zones due to the occurrence of martensite. Weld samples fabricated using beam oscillations showed lower microhardness compared with joints produced by stationary beam welding. This decrease in hardness arose from enhanced grain growth and additional diffusion of carbon out of the austenite lattice due to beam oscillations. Beam oscillations did not introduce any significant morphological changes to the weld microstructure, but resulted in enhanced tensile strength and lower microhardness in the weld joints.

Keywords Electron beam welding · Electron backscatter diffraction (EBSD) · Microhardness · Phase transformation · Weld microstructure · Tensile properties

1 Introduction

In manufacturing today, the need for advanced welding and joining technologies has become indispensable [1–3]. Coarse grains in the fusion zone, inadequate cleanliness and inability to join thicker plates in a single pass are some of the problems that arise during the fabrication of engineering components using regular welding processes [4, 5]. To overcome such difficulties, high-energy beam welding technologies have been developed. Electron beam welding (EBW) is one such fusion welding technique where a narrow beam of electrons is used in welding two pieces of metal. Upon impact with the work piece, the fast-moving electrons penetrate the surface of the material and transfer their kinetic energy to the surrounding atoms in the form of heat, causing localized melting and partial vaporization.

A deep cavity is formed due to the intense recoil pressure exerted by the vapour flux on the evaporating surface. The formation of such a cavity or keyhole leads to deep penetration with high aspect ratio. The precise control of the electron beam power density makes it possible to achieve better penetration depths with narrow weld seams and high welding speeds [6]. This is one of the biggest advantages of EBW over conventional welding methods. However, the welding process must be carried out in vacuum in order to prevent the dispersion of the beam. In the presence of a gaseous medium, electrons scatter widening the beam and drastically reducing its power density [7].

Application of EBW is not only limited by vacuum but also by other factors like beam deflection due to retained magnetism in materials, X-ray irradiation and the need for complex tooling [8]. Despite such limitations, it has proven to be advantageous in diverse fields of applications. In the production of turbines for energy and aerospace applications, this technology has aided in reducing production costs and time by substituting large casted parts with welded sub-assemblies. Additionally, due to the fact that the process takes place in vacuum, the

✉ Krishna Komerla
  kkomerla@iehk.rwth-aachen.de

Extended author information available on the last page of the article.

Springer

formation of detrimental oxides and nitrides in the heat-affected zone is effectively eliminated which enhances the durability of joints [9]. In the automotive industry, it is particularly useful in welding gear transmission parts, crankshafts, piston rods, valve heads and others. In nuclear, chemical and oil industries, EBW provides the necessary depth to width ratio and narrow heat-affected zones, making it ideal for joining thick sections in a single pass [10].

EBW is a dynamic process that is influenced by the welding parameters, the thermal material properties and the beam characteristics including the beam power, energy density distribution, welding speed, focal location and spot size [11]. The experimental measurement of the EBW is both difficult and time consuming; for this reason, numerical simulation models were developed, in order to study the melt pool dynamics and enhance the weld quality. Ziolrowski et al. [12] presented a volumetric heat source for deep welding of different metals that considered the electron beam deflections, resulting from the thermoelectric fields caused by the seebeck effect. Rai et al. [13] developed an energy balance model considering the variation of keyhole wall and calculated the fluid flow and the heat transfer during the EBW. The investigation reported on the temperature evolution around the keyhole, the thermal cycles, the weld geometry and the material flow. Chiumenti et al. [14] developed an in-house multi-physics finite element code, to study the electron beam power surface distribution and the corresponding adsorption within the work piece. Huang et al. [15] provided a novel three-dimensional mathematical model that describes the coupling of keyhole and the melt pool during EBW. The physical effects such as the beam reflection, adsorption of the keyhole wall, scattering of the secondary electrons, keyhole evaporation heat loss and beam defocus were rigorously treated in this heat source model. Despite the efforts, understanding of the electron interactions with the work piece during impingement, the formation of keyhole and the melt pool dynamics taking place during EBW is still lacking. There is a strong need for better simulation models that could aid the theoretical study of EBW.

In fusion welding, physical processes, such as melting, solidification, subsequent solid-state phase transformations, recrystallization and grain growth controlled by heat and mass transfer, define the development of weld microstructure and its morphological evolution. The process parameters including the welding current, applied voltage, welding speed and beam oscillation largely govern the transport conditions and the thermal history of the weld, which in turn influences the mechanical properties of the weld joints. It is therefore of critical importance to understand the effect of process parameters on the weld microstructure and mechanical properties in order to produce sustainable weld joints.

Many researchers have investigated the influence of welding parameters on the microstructure and mechanical properties of the electron beam welded joints. Oscillation of the electron beam along a predetermined pattern (elliptical, circular or linear) has been known to improve mixing and restrict segregation in the weld pool [16, 17]. In general, beam oscillation enlarges the keyhole and helps reduce the porosity formation in the weld [18, 19]. Furthermore, the change in dynamics of the molten zone also prevents the weld root from dropping through and provides a smoother weld seam. Trushnikov et al. [20] studied the dependence of weld profile on the changing distribution of bombarding electrons in the keyhole caused by oscillations and reported a significant alteration to the shape of the weld pool. Dinda et al. [18] performed dissimilar metal joining of plain carbon steel to Fe-7%Al alloy and reported that beam oscillation resulted in welds with homogeneous microstructure and lower hardness. Also, the yield strength and ultimate tensile strength of the weld joints were found to be unaffected. Wang et al. [21] reported on the stabilizing influence of beam oscillation on the weld morphology and upon the increase of equiaxed grains in the fusion zone of high-strength aluminium alloys. Kar et al. [22] found that austenitic stainless steel joints made with oscillating beam possessed homogeneous microstructure and showed improved notch toughness and bending strength. Rajakumar et al. [23] compared gas tungsten arc welding (GTAW) with EBW and reported that borated stainless steel joints made with oscillating electron beam exhibited finer dendritic microstructure in the fusion zone along with improved tensile properties in comparison with the GTAW joints. However, a comprehensive study on the influence of beam oscillations on low-carbon multiphase steels is yet to be reported.

The aim of this study is to investigate the influence of high-frequency beam oscillations on the microstructure and the mechanical properties of low-carbon steels. Conventional techniques like light optical microscopy (LOM), electron backscatter diffraction (EBSD), micro-indentation, tensile tests coupled with digital image correlation (DIC) and three-point bending tests were used to characterize the strength and performance of the butt welds.

LOM micrographs of the weld cross sections presented pore-free and crack-free joints with thorough penetration. Beam oscillation produced conical weld profiles with wider fusion zone (FZ) and heat-affected zone (HAZ) containing smaller undercuts at the weld root. EBSD pole figure maps of the weld sections revealed epitaxial grain growth in the FZ for both the alloys. The S235JR alloy exhibited columnar grains that curved towards the centre of the weld, while axial growth nearly perpendicular to the weld centre line was seen in the DP1000 weld joints. A comparison of the pole figure maps of weld sections showed that beam

Fig. 1 Light optical micrographs depicting the microstructure of S235JR and DP1000 steels in the as-obtained state
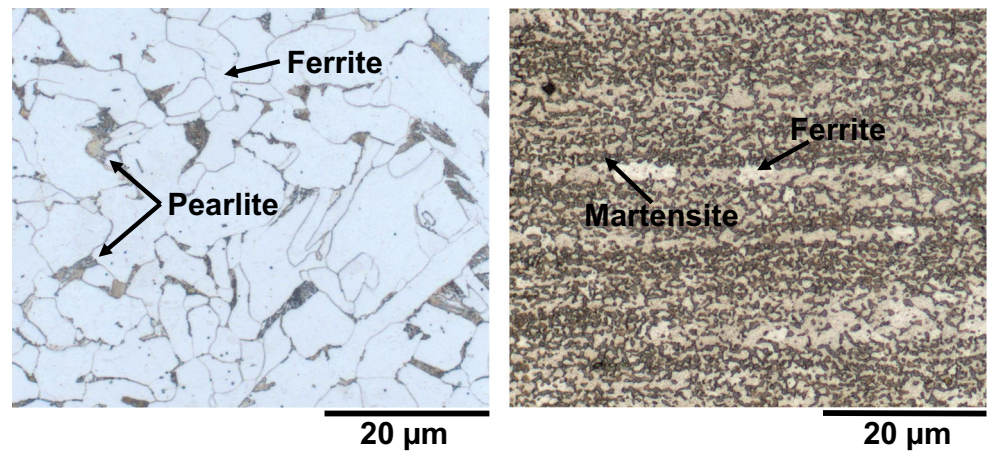
(a) Micrograph of S235JR alloy consisting of 90% ferrite and 10% pearlite phase fractions

(b) Micrograph of DP1000 alloy consisting of 60% ferrite and 40% martensite phase fractions

oscillation did not introduce any significant changes to the weld morphology. Considerable heterogeneity in grain size was observed across the weld joints due to the steep temperature gradients produced during EBW. A comparison of the Vickers microhardness maps showed that beam oscillations produced joints that exhibited lower microhardness. Additionally, in DP1000 alloy, beam oscillations yielded wider softened HAZ where the hardness was less than the base material (BM). This can be attributed to the tempering of martensite due to higher local peak temperature achieved by beam oscillation. The tensile properties of all the weld joints were similar to their base materials, no significant decrease in yield or tensile strength was seen. However, joints obtained with beam oscillation exhibited a marginal reduction in the elongation to failure when compared with their BM. The face and root bending strengths of the weld joints were found similar to the base material, no weld line opening or cracking was seen. The joints provided adequate ductility and strength and successfully qualified the bending tests.

2 Materials

A 5-mm-thick hot-rolled structural steel (S235JR) and a 1-mm-thick cold-rolled dual-phase steel (DP1000) were considered in this study. The S235JR is an impact-tested, low-carbon ferritic steel widely used in structural applications like construction of bridges, penstocks, pipes

and offshore structures [24, 25]. In the as-obtained state, it consisted of approximately 10% pearlite and 90% ferrite microstructure and showed an yield strength of 310 MPa and tensile strength of 415 MPa. The DP1000 is an advanced high-strength steel that offers impressive mechanical properties like the absence of yield point elongation, high work hardening rate and high ultimate tensile strength [26–28]. These unique characteristics of DP steels are vastly sought after in the automotive industry, to reduce weight and improve passenger safety [29, 30]. DP steels derive strength from their complex microstructure, comprising of hard martensite islands dispersed in soft ferritic matrix [31, 32]. In the as-obtained state, it consisted of approximately 40% martensite and 60% ferrite phase fractions. It exhibited an yield strength of 740 MPa and tensile strength of about 1000 MPa. The initial microstructure of both the alloys is presented in Fig. 1 and their chemical composition is listed in Table 1.

3 Experimental methods

3.1 Electron beam welding

Steel blanks were butt welded (position PA as per DIN EN ISO 6947) using a universal chamber EBW machine of type K7 made by pro-beam (Germany). To ensure perfect fit and ease of welding, sheets were cut into smaller blanks of size $150 \times 100 \times t$ mm ($t = 5$ mm for S235JR

Table 1 Chemical composition of S235JR & DP1000 alloys in weight %

Element	C	Si	Mn	P	S	Cr	Ni	Cu	Al	Ti	N
S235JR	0.075	0.054	0.94	0.0264	0.001	0.393	0.039	0.022	0.026	–	0.012
DP1000	0.082	0.315	2.50	0.0145	0.002	0.685	0.022	0.101	0.032	0.076	0.0141

Table 2 EBW parameters used in laboratory welding, weld nos. 1 and 2 were used in welding S235JR alloy and weld nos. 3 and 4 were used in welding DP1000 alloy

Weld No.	Chamber pressure (hPa)	Accelerating voltage (kV)	Beam current (mA)	Welding speed (mm/s)	Oscillation type	Oscillation radius (mm)	Frequency (Hz)
1	10^{-4}	120	35	40	Circle	0.5	500
2	10^{-4}	120	35	40	–	–	–
3	10^{-4}	120	7.5	40	Circle	0.5	100
4	10^{-4}	120	6	40	–	–	–

and 1 mm for DP1000) and their edges were carefully polished. Autogenous welding was carried out where, the electron beam was focussed on the surface of work piece to produce the welds in a single pass without preheating. Consumables, additional fixtures and welding tacks were not utilized during the welding process. The different sets of parameters used in welding the S235JR and DP1000 alloys are listed in Table 2. Welding was carried out perpendicular to the rolling direction (RD) of the sheets and the necessary parameters were chosen by observing the weld seams for complete penetration and clean weld profile.

Additionally, metallographic investigation of the weld cross sections was also carried out to ensure defect-free weld joints. Figure 2a illustrates the typical weld setup indicating the butt welding of steel blanks, the beam source and the welding direction.

3.2 Microstructural characterization

Light optical microscopy and electron backscatter diffraction (EBSD) were used to characterize the weld microstructure. Specimens cut from the weld cross section were embedded in thermo-setting epoxy resin to facilitate easy handling during grinding and polishing. After mounting, specimens were mechanically grinded using abrasive paper and then polished using diamond paste up to 1 µm in order to minimize topology and surface relief. Nital (Nitric acid and ethyl alcohol) etching was carried out to reveal the weld microstructure. Electron backscatter diffraction (EBSD) measurements were also carried out to identify various microstructural aspects of the weld joints. For EBSD measurements, additional samples were cut, grinded and further polished using colloidal silica suspension containing particles of size 50 nm to smoothen any remaining artefacts.
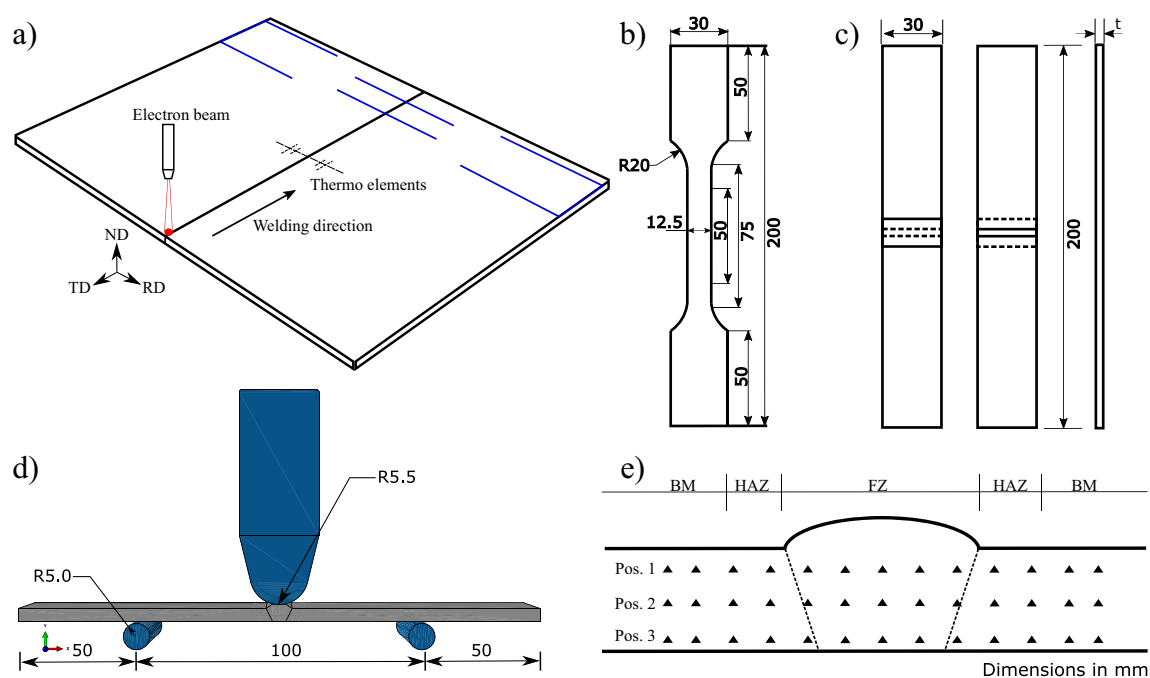

Fig. 2 a Weld setup depicting the beam source and welding along the transverse direction (TD). **b** Tensile test sample geometry cut along the rolling direction (RD). **c** and **d** Face (left) and root (right) bending test sample geometries along with three-point bending test setup. **e** Positions where microhardness is measured across the weld joint to obtain a hardness contour

EBSD maps were acquired on a Schottky field emission gun scanning electron microscope (SEM), equipped with a EDAX-TSL detector and OIM software. An accelerating voltage of 20 kV and step sizes of 200 nm for DP1000 and 250 nm for S235JR alloy were used for the measurement. After dynamic background subtraction, the intensity of diffraction patterns was normalized and points with a confidence index less than 0.1 were discarded. Grains were obtained by enforcing a 5° misorientation criterion.

3.3 Mechanical characterization

The mechanical properties of the weld joints were characterized using micro-indentation, tensile tests and three-point bending tests. Vickers hardness was measured at evenly spaced points across the cross section of joints covering the FZ, HAZ and part of the BM at various positions, as indicated in the Fig. 2e. At each position, over 30 indentations were made using a load of 100 g and a dwell time of 5 s. As both the S235JR and DP1000 alloys contained multiphase microstructures with fine grains, a weight of only 100 g was used in order to keep the inter-indent spacing to a minimum of 0.1 mm. The applied load was sufficient and provided quality indents in both the alloys. For tensile testing, samples were cut along the RD such that the weld line was positioned exactly at the centre of the gauge length. Geometry of the tensile samples is presented in Fig. 2b. As per the standard EN 4136:2013, quasi-static tensile tests were performed using a 100 kN load cell and a strain rate of 0.001/s. To ensure repeatability, a minimum of three specimens were tested for each weld condition. In order to map the strain distribution in the FZ and HAZ, digital image correlation (DIC) technique was used during the test. A speckle pattern consisting of white

and black spots was created on the tensile sample surface that enabled the DIC system to capture data. A high-speed camera took a series of pictures during deformation which were later analyzed using the GOM software to obtain the strain maps (Appendix). As per the standard EN 5173:2010 [33], face and root bend tests were also performed to quantify the ductility and bending strength of the weld joints. A 50 kN load cell and a constant bending speed of 2 mm/s were used during the test. The three-point bending test setup, with 50 mm outer span, 100 mm inner span and the tool radius of 5.5 mm, along with the sample geometry is presented in Fig. 2c and d. The electrical signal obtained from the transducer and strain gauge provided the required force and displacement data.

4 Results and discussion

4.1 Weld profile

In Fig 3, the weld profiles of S235JR and DP1000 alloys obtained from both oscillated and stationary beam welding are presented. Beam oscillation along a chosen trajectory creates a variation in the electron bombardments inside the keyhole, leading to the dynamic distribution of power around the stationary position of the beam. This caused a significant change in the heat flow around the keyhole. It is for this reason that the usual nail like weld nugget geometry, consisting of a wide upper zone and narrow key hole as seen in Fig. 3b and d, was replaced by a more homogeneous conical shape (see Fig. 3a and c). Also, the increased interaction volume of heat source with the work piece creates wider fusion and heat-affected zones. This effect became more pronounced for weld samples of smaller

Fig. 3 Cross sectional micrographs of weld joints, (**a**) & (**b**) weld profiles of S235 alloy obtained with oscillated & stationary beam welding, (**c**) & (**d**) weld profiles of DP1000 alloy obtained with oscillated & stationary beam welding
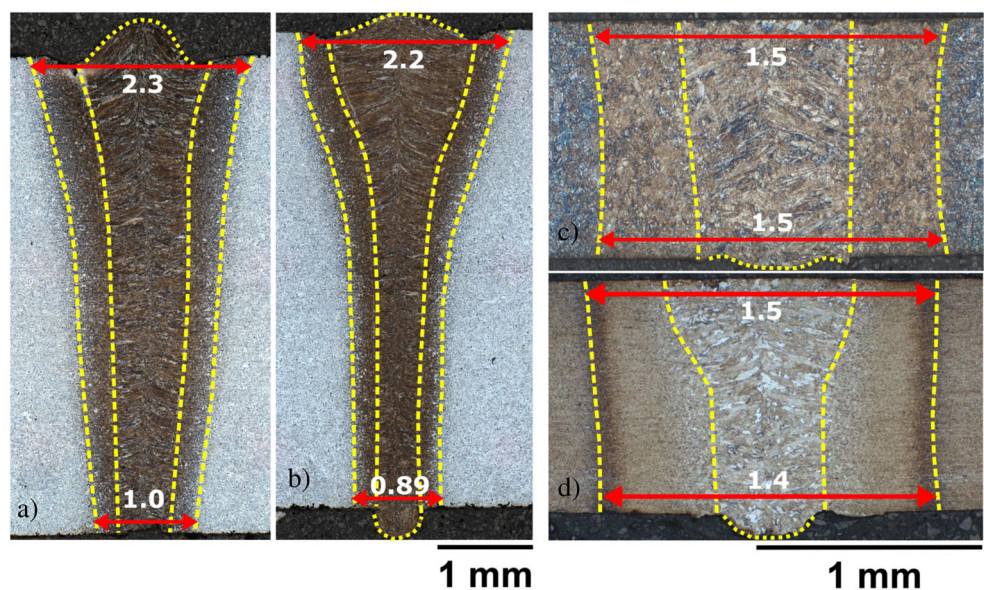
thickness. As the keyhole expands due to the oscillation of beam, the associated power density at the bottom of the keyhole was lowered, reducing the penetration depth of the beam. Therefore, weld joints obtained from stationary beam welding exhibit larger undercuts at the weld root in comparison with the weld joints obtained with oscillated beam welding.

However, the reduction in penetration depth due to the oscillation of beam was minimal and did not affect the weld quality. As non-destructive testing was not performed, to ascertain the weld quality, cross sections obtained from over five different positions along the welding direction were investigated and their micrographs revealed defect-free welds with thorough penetration. For convenience, only micrographs from one of the sections is presented in the Fig. 3.

4.2 Weld microstructure

Alloy composition, welding process parameters and metallurgical processes like melting, fluid flow, solidification and subsequent solid-state phase transformations control the development of microstructure and in turn the mechanical properties of the weldment. In a weld joint, the FZ experiences temperatures above the liquidus temperature during welding and exhibits solidification microstructure. The competitive growth of weld metal grains is primarily controlled by the highest temperature gradients and the easy growth crystallographic orientation, which for cubic metals is along the [100] direction [34]. According to the *ASM handbook* on welding [35], the highest temperature gradients are typically aligned perpendicular to solid-liquid (S/L) interface that follows the moving melt pool. At high welding speeds, the melt pool takes the shape of an elongated tear drop, where the S/L interface is straight and results in the axial growth of columnar grains from the fusion line towards the centre of the weld.

In the FZ of both the alloys, spontaneous epitaxial solidification took place, where large columnar grains nucleated at the fusion line and grew towards the centre of the molten weld pool. However, minor differences can be observed in their morphology. The DP1000 weld joints contain columnar grains that grew nearly perpendicular to the weld centre line.

While in the S235JR weld joints despite the high welding speed, their greater thickness leads to the entrapment of more heat at the weld centre which altered the shape of the melt pool. This change in melt pool shape lead to a curved S/L interface line, and as a result, the weld joints exhibited columnar grains that curved towards the centre of the weld.

The HAZ of the weld joint corresponds to temperatures that are high enough to induce metallurgical transformations but too low to cause melting. The peak HAZ temperature increases with the decreasing distance from the weld
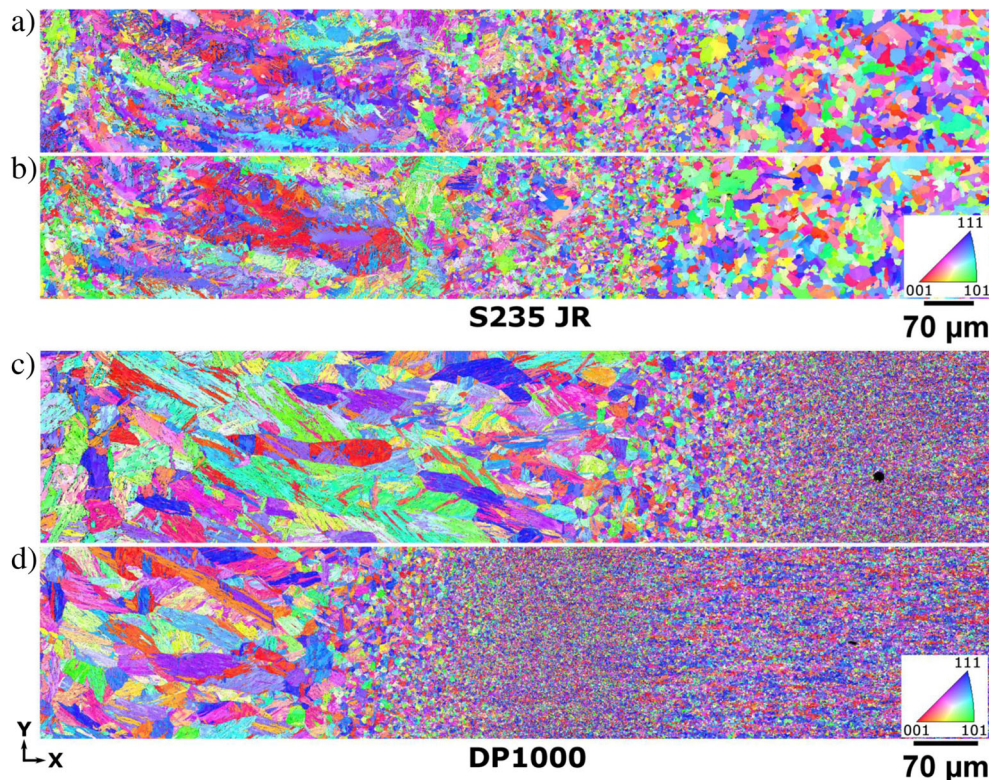

Fig. 4 Inverse pole figure (EBSD) maps obtained from the centre of S235JR and DP1000 weld joints depicting the morphology and the variation of grain size across the FZ, CGHAZ and FGHAZ obtained with oscillated (**a**, **c**) and stationary (**b**, **d**) beam welding

centre. Grain growth in crystalline materials is function of temperature and time; therefore, in the HAZ, the maximum grain size occurs usually adjacent to the FZ where highest peak temperature is seen. Also, the cooling rate has a considerable influence on the coarsening of the weld microstructure. At lower cooling rates, grains are exposed to higher temperatures for longer duration resulting in further coarsening. The various weld regions and phases in the FZ and HAZ for both the alloys are presented in Fig. 4. The inverse pole figure (EBSD) maps of the transverse section reveal a substantial variation of grain size across the weld joint for all the welded samples. Such heterogeneity in microstructure can be attributed to the steep temperature gradients attained during EBW. Based on the observed variation of the grain size, the HAZ was further divided into a coarse grain heat-affected zone (CGHAZ) and a fine grain heat-affected zone (FGHAZ).

The microstructure of S235JR steel joints consisted primarily of martensite (α'), small fraction of bainite (α_b) and ferrite (α) phases as shown in Fig. 5. α' forms when the face-centred cubic (FCC) austenite (γ) phase does not have sufficient time to rearrange itself into a body-centred cubic (BCC) lattice of α during rapid cooling. When this occurs, the FCC lattice shears into a body-centred tetragonal (BCT) structure, trapping the interstitial carbon atoms that were dissolved in the γ phase. This shearing of γ lattice into α' is accompanied by massive volumetric dilatation which is one of the crucial reasons behind the residual stresses in the weld

joint. Microstructure under stress tends to deform in order to minimize its internal forces, but the lack of slip planes in the BCT structure restricts its plastic deformation leading to elastic stresses. In the FZ, columnar grains of γ solidified from liquid and subsequently decomposed predominantly into lath α' and lower α_b during cooling. The local peak temperature in the CGHAZ was above Ac_3 and the base metal was fully austenized to form coarse equiaxed grains of γ that also decomposed predominantly into α' and α_b. The FGHAZ, was relatively larger in size in comparison with the CGHAZ and contained regions with local peak temperature ranging from around Ac_3 to below Ac_1.

Therefore, it exhibited grains that were either fully or partially austenized and grains of the base metal that were thermally softened. The transformation mechanism was similar to the CGHAZ, but the grain size was finer because of the lower local peak temperature.

In the DP1000 weld joints, similar observations are made with minor differences. α_b phase was not detected in the weld joint. The FZ and HAZ contained only α' and α phases as shown in Fig. 5. The higher Mn content in the alloy aided in stabilizing the austenite and the rapid cooling due to smaller sheet thickness combined with high welding speeds led to the rapid γ - α' shear transformation. Furthermore, the base metal of DP1000 steel contained very fine grained α surrounded by lath α' along with a small fraction of precipitates (TiN, AlN). As a result, grains seen in the FGHAZ are larger than that in the BM.
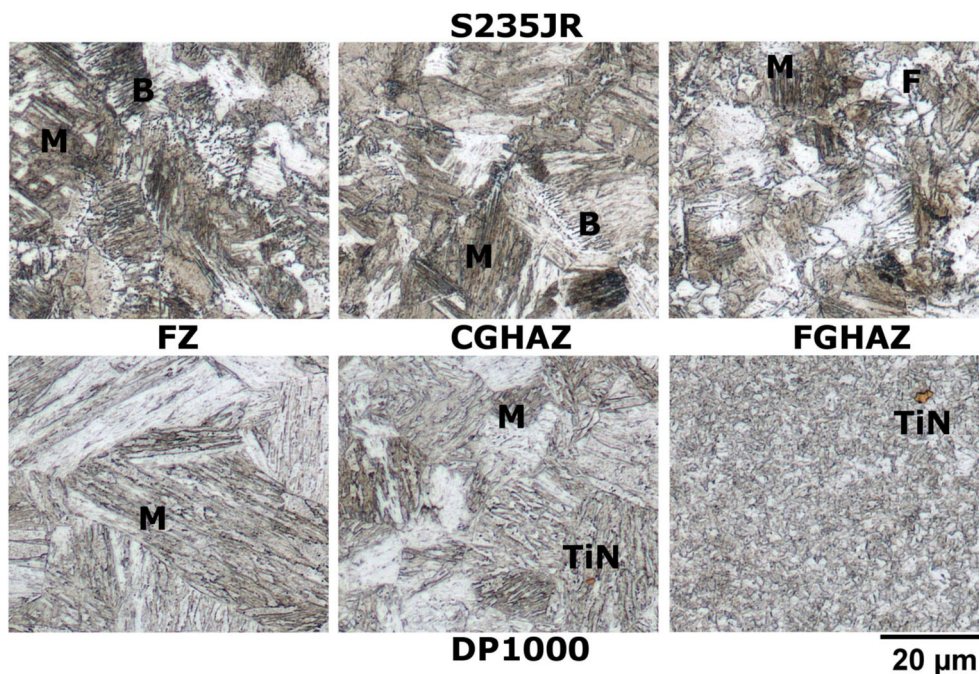

Fig. 5 Light optical micrographs of S235JR and DP1000 steel weld joints exhibiting various phases across the FZ, CGHAZ and FGHAZ of both S235JR and DP1000 weld joints
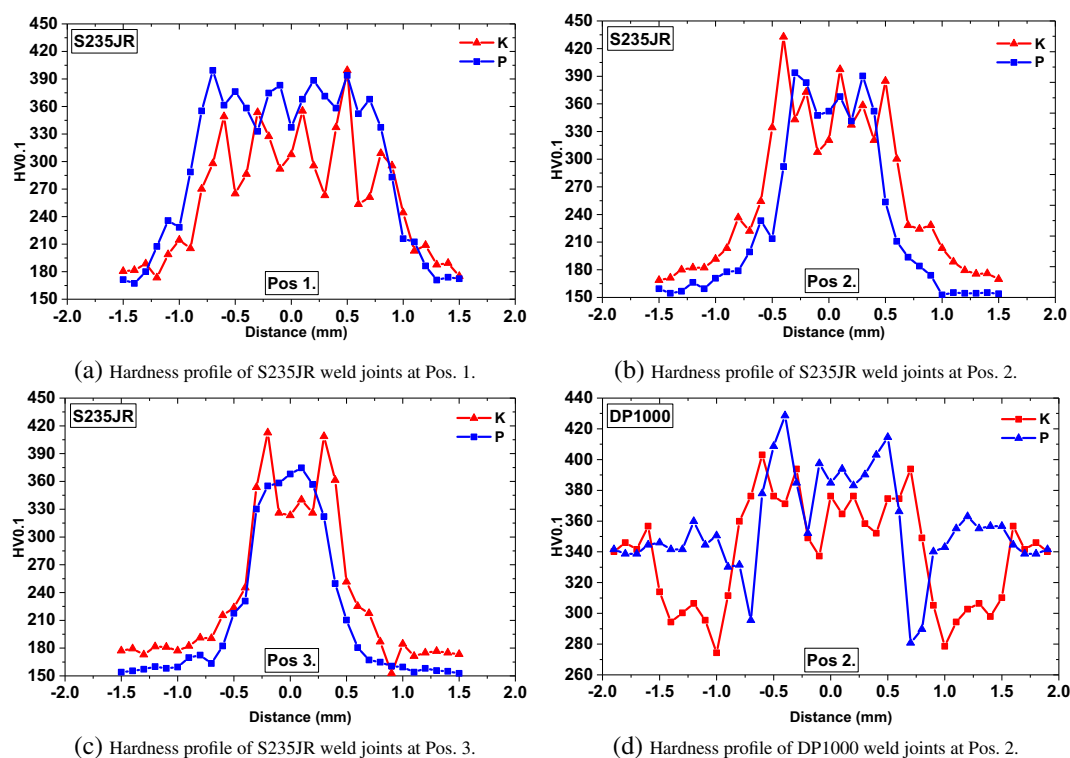
(a) Hardness profile of S235JR weld joints at Pos. 1.

(b) Hardness profile of S235JR weld joints at Pos. 2.

(c) Hardness profile of S235JR weld joints at Pos. 3.

(d) Hardness profile of DP1000 weld joints at Pos. 2.

Fig. 6 Quasi-static tensile response BM and weld joints. BM1 and BM2 refer to specimens of base material; K1 and K2 refer to welded specimens produced with oscillated beam welding; P1 and P2 refer to welded specimens produced with stationary beam welding
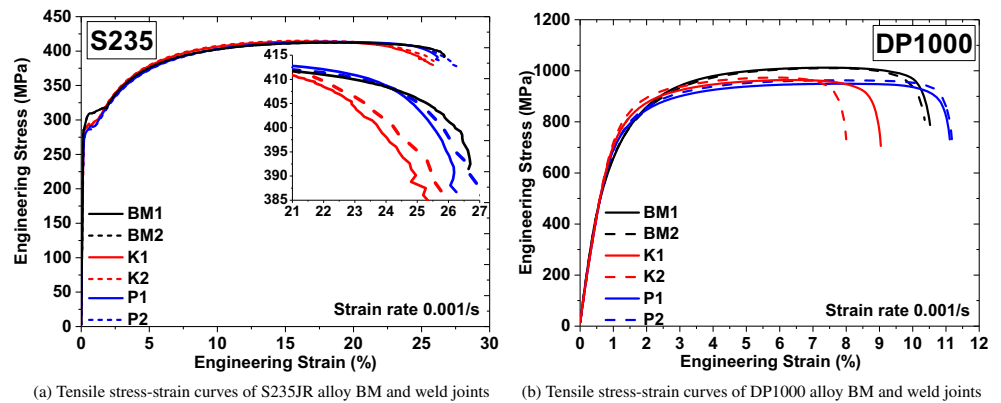
4.3 Microhardness

Vickers microhardness (MH) measurements were carried out to study the influence of temperature on the microstructure of the weld joint. The steep temperature gradients produced during welding result in multiphase microstructures that exhibit heterogeneous mechanical properties. MH is generally correlated to the tensile strength of a material; therefore, it is crucial to understand the distribution of hardness in the weld joint to ascertain the strength of the individual regions and their impact on the overall mechanical behaviour of the weldment.

4.3.1 MH in S235JR weld joints

The MH profiles obtained at positions as indicated in Fig. 2e on the weld cross section are presented in the Fig. 6. The FZ, HAZ and BM can be clearly distinguished from their hardness contours. The hardness of the as-received BM is about 180 $HV_{0.1}$. At Pos 1, it can be seen that, in the FZ, hardness increases from 180 $HV_{0.1}$ to between 375–395 $HV_{0.1}$ and 290–350 $HV_{0.1}$ for stationary and oscillated beam weld joints respectively. The weld joints obtained through beam oscillation exhibit lower hardness in comparison with the stationary beam welded joints. Generally, such high hardness is the consequence of base

metal transformation to α'. The hardness of α' can be associated to the amount of carbon trapped in its lattice. The higher the interstitial carbon content, the higher the hardness. The presence of interstitial carbon in larger atomic fractions leads to greater shearing of the BCC lattice producing a hard and stiff BCT phase. Beam oscillation as discussed earlier introduces lower cooling rates which promote the additional diffusion of carbon out of austenite lattice during the phase transformation. This lowers the hardness of martensite in the FZ. Furthermore, the lower cooling rates also promote grain growth in the FZ, which results in larger grains leading to lower hardness. Additionally, the steep temperature gradients in the FZ lead to the occurrence of carbon-rich/carbon-depleted regions that exhibit inhomogeneous strength. For this reason, considerable fluctuation in hardness can be seen in the FZ. In the HAZ however, irrespective of being produced with stationary or oscillated beam welding, a steep decrease in hardness from over 300 $HV_{0.1}$ to between 190 and 210 $HV_{0.1}$ is seen. Similar observations can also be made at Pos 2 and Pos. 3. Though similar trend in hardness profiles is seen, the weld joints obtained with beam oscillation exhibited higher hardness in both the FZ and the HAZ. This increase in hardness can be correlated to the decreasing power density and lower peak temperatures that yield carbon-rich martensites with high strength.

Fig. 7 Quasi-static tensile response BM and weld joints, BM1 & BM2 refer to specimens of base material; K1& K2 refer to welded specimens produced with oscillated beam welding; P1 & P2 refer to welded specimens produced with stationary beam welding

(a) Tensile stress-strain curves of S235JR alloy BM and weld joints

(b) Tensile stress-strain curves of DP1000 alloy BM and weld joints

4.3.2 MH in DP1000 weld joints

Figure 6d presents the MH profiles of DP1000 weld joints obtained at Pos. 2. The FZ exhibits higher hardness in the range of 400–380HV$_{0.1}$ and 380–360HV$_{0.1}$ respectively for both stationary and oscillated beam weld joints in comparison with its BM, which in the as-obtained state exhibits a hardness of 340 HV$_{0.1}$. With a mechanism similar to that of S235JR alloy, weld joints produced with oscillated beam welding exhibit marginally lower hardness in the FZ. In the HAZ however, unlike S235JR welds, softening phenomenon is seen in the DP1000 weld joints where the hardness is significantly lower than the BM.

According to the Hall-Petch relationship, grain size and hardness are inversely proportional to each other, such that an increase grain size would lead to the reduction in hardness [36]. The grain size of the HAZ was larger than the BM due to the grain growth that took place during welding. It is for this reason that lower hardness is seen in the HAZ of the weld joints. Additionally, tempering of the existing martensite also took place in the HAZ, where the diffusion of trapped carbon out of the martensite lattice relieves the internal stresses and lowers the hardness. This tempering of martensite is unrelated to the welding process, but the

width of HAZ and its temperature distribution are directly controlled by the welding process parameters. It is evident from the hardness plot that the weld joints obtained with beam oscillation consist of a wider HAZ and underwent considerable softening. The MH is at least 40 HV$_{0.1}$ less than that of the BM and is spread over 500 microns in width. Typically, HAZ softening leads to decrease in the local mechanical properties of the weldment; however, due to the smaller weld seams produced in EBW, no critical decrease yield or tensile strength is observed.

4.4 Tensile properties

Tensile characteristics of the weld joints were studied under quasi-static loading conditions at room temperature in order to determine their strength and elongation to failure (see Fig. 7). In the weld samples of both alloys irrespective of being produced with stationary or oscillated beam welding, fracture occurred away from the weld joint as shown in Fig. 8. For comparison, the yield strength, ultimate tensile strength and total elongation of both BM and weld joints are listed in Table 3.

Generally, low-carbon structural steels exhibit yield point elongation during deformation. The engineering stress-strain curve of S235JR steel can be divided into a linear
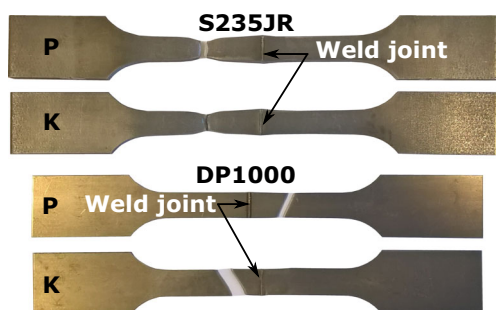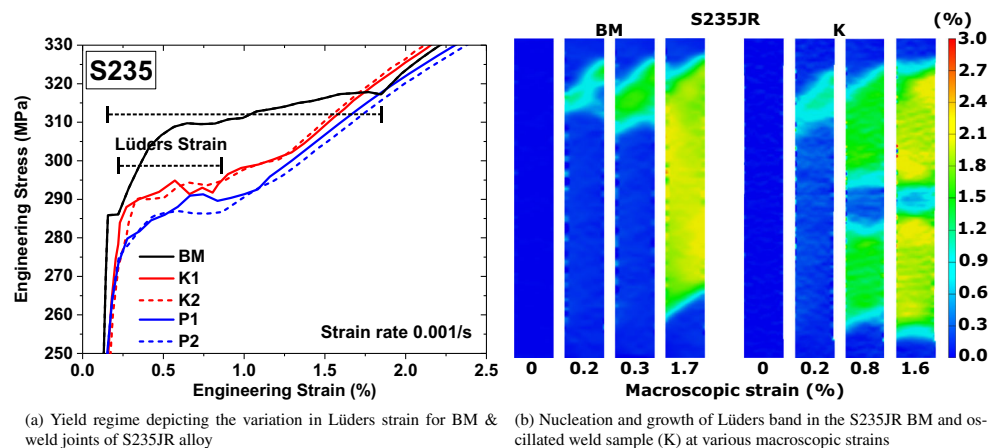

Fig. 8 Tested weld specimens of S235JR and DP1000 alloys depicting failure away from the weld joint. K refers to specimens produced with oscillated beam welding; P refers to specimens produced with stationary beam welding

Table 3 List of yield strength (σ_y), ultimate tensile strength (σ_{UTS}) and total elongation (TE) of S235JR and DP1000 alloy BM and weld joints; K refers to specimens produced with oscillated beam welding; P refers to specimens produced with stationary beam welding

Alloy	Weld	σ_y (MPa)	σ_{UTS} (MPa)	TE (%)
S235JR	BM	310	413	26
	K	295	413	25
	P	290	412	26
DP1000	BM	742	1010	10
	K	762	968	8.5
	P	756	951	11.5

Fig. 9 Comparison of yield point elongation in the S235JR BM and weld joints along with the evolution of Lüders band along the tensile axis. BM1 and BM2 refer to specimens of base material; K1and K2 refer to welded specimens produced with oscillated beam welding; P1 and P2 refer to welded specimens produced with stationary beam welding

(a) Yield regime depicting the variation in Lüders strain for BM & weld joints of S235JR alloy

(b) Nucleation and growth of Lüders band in the S235JR BM and oscillated weld sample (K) at various macroscopic strains

elastic regime until the upper yield point, a yield regime where the stress drops to the lower yield point and stagnates until the Lüders strain and finally a hardening regime with rise in stress until the ultimate tensile stress, after which necking leads to failure [37]. In the S235JR alloy, both stationary and oscillated beam weld joints exhibited minimal reduction in yield strength (σ_y) of about 15 MPa and 20 MPa respectively, but did not show any significant difference in the ultimate tensile strength or total elongation. A closer observation of the yield regime as shown in Fig. 9a, divulged that the BM exhibits a Lüders strain of $\approx$ 1.75% which is more than twice that of the stationary and oscillated beam welded joints ($<$ 0.7%).

The yield point elongation occurs primarily due to the movement of an invariant deformation profile (Lüders band) along the tensile axis. The deformation associated with such Lüders deformation usually exhibits quasi-stationary behaviour with small strains and constant deformation rate that results in a stagnant extension rate with no work hardening. Figure 9a illustrates the propagation of such a Lüders band in the BM until a macroscopic strain of 1.75%. This constant plastic strain can be correlated to the yield point elongation observed in the stress-strain curve of the BM presented in Fig. 7a. The presence of weld joint consisting of hard and strong phases like martensite reduces the effective length of band propagation. As seen in the strain distribution maps shown in Fig. 9b, first instance of a Lüders band nucleates in the BM and propagates until it reaches the weld seam. At the end of first instance, another Lüders band nucleates and propagates with further deformation in the other half of the tensile specimen while the first half of the tensile sample work hardens. This simultaneous occurrence of hardening and yield point elongation can be seen on the flow curve above a macroscopic strain of 0.7%.

Dual-phase (DP) steels offer impressive mechanical properties like the absence of yield point elongation, high work hardening rate and high ultimate tensile strength. The stress-strain curves of the BM and weld joints are presented in Fig. 7b. Compared with the BM, both weld joints exhibited lower ultimate tensile strength. However, the weld joints produced with stationary beam provided marginally

Table 4 Bending strength of the both S235JR and DP1000 alloy weld joints and base material; K refers to oscillated welds; P refers to non-oscillated welds

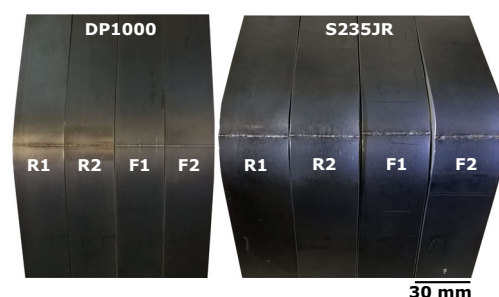| Alloy	Weld	Bend strength (kN)	
		Face	Root
S235JR	BM	2.90 ± 0.05	2.90 ± 0.05
	K	3.00 ± 0.15	2.99 ± 0.02
	P	2.97 ± 0.01	2.92 ± 0.04
DP1000	BM	0.20 ± 0.01	0.20 ± 0.01
	K	0.21 ± 0.01	0.20 ± 0.01
	P	0.19 ± 0.02	0.19 ± 0.03

Fig. 10 Three-point bend specimens of DP1000 and S235JR welds; R1 and F1 refer to root and face bend tests without oscillation; R2 and F2 refer to the root and face bend tests with beam oscillation

longer elongation to failure in comparison with the BM. While the weld joints produced by beam oscillation showed marginal reduction in ductility. Under both conditions of welding, the weld seam did not undergo any deformation and the width of the weld zones played a critical role in the determining the total elongation of the tensile sample. With smaller weld zones and tempered martensite, the stationary beam welds provided similar ductility as that of the BM while the oscillated beam welds despite consisting larger softened HAZ exhibited early failure. Even with the increased thermal softening, the oscillated beam welded joints did not show any considerable reduction in the yield or tensile strength.

4.5 Bending strength

As per standard EN 5173:2010, face and root bend tests were carried out on the weld joints of both S235JR and DP1000 alloys and the results are presented in Table 4. The bent samples as shown in Fig. 10 successfully qualified the bend tests and exhibited good ductility and strength. No surface cracks, tearing of the weld line or fracture was observed in the weld joints regardless of being produced with or without the electron beam oscillation. However, it can be seen that joints of both alloys produced by beam oscillation presented slightly higher bending strength in both face and root tests in comparison with the stationary beam welded joints.

5 Conclusions

In this study, the effect of electron beam oscillations on the microstructure and mechanical properties of low-carbon steels was investigated. The main conclusions drawn are as follows

– Beam oscillations along a circular trajectory produced a stirring effect that improved the heat transfer in the keyhole and resulted in enlarged FZ and HAZ in the weld joints.
– The reduction in the penetration depth achieved through beam oscillation, yielded weld seams with smaller undercuts and better finish.
– The relatively larger thickness of the S235JR weld blanks led to increased entrapment of heat at the weld centre, which altered the melt pool shape and resulted in producing columnar grains that curved towards the centre of the weld.
– Beam oscillations did not particularly affect the morphology of the weld microstructure and no significant observations in the solidification pattern or grain growth could be seen; however, they produced considerable

differences in the mechanical properties of the weld joints.
– Beam oscillation produced lower hardness in the FZ, indicating improvement in the mechanical properties and lower residual stresses. However, in the DP1000 steel, it also resulted in HAZ softening where $HV_{0.1}$ was lower than the BM.
– With beam oscillations of 0.5-mm amplitude, the width of the softened HAZ increased to over 500 µm in the DP1000 steel, while no significant softening effects were seen in the HAZ of the S235JR steel joints.
– No significant decrease in yield or tensile strength was seen during the tensile test of the welded samples. However, beam oscillation resulted in marginally less elongation to failure.
– For improved product life, producing joints with electron beam oscillation is more efficient as they exhibit higher tensile strength, lower hardness and lower residual stresses.
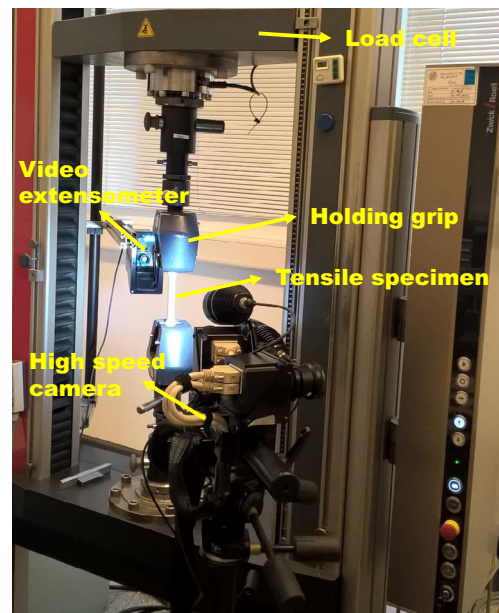
Appendix

Fig. 11 Tensile test setup depicting the load cell, holding grips, tensile specimen and the video extensometer used to measure the elongation; A high-speed camera was also employed to study the nucleation and growth of Lüders band

References

1. Wang P, Chen X, Pan Q, Madigan B, Long J (2016) Laser welding dissimilar materials of aluminum to steel: an overview. Int J Adv Manuf Technol 87(9):3081–3090. https://doi.org/10.1007/s00170-016-8725-y

2. Williams E, Lavery N (2017) Laser processing of bulk metallic glass: A review. J Mater Process Technol 247(Supplement C):73–91. https://doi.org/10.1016/j.jmatprotec.2017.03.034. http://www.sciencedirect.com/science/article/pii/S0924013617301279

3. Verma J, Taiwade RV (2017) Effect of welding processes and conditions on the microstructure, mechanical properties and corrosion resistance of duplex stainless steel weldments - A review. J Manuf Process 25(Supplement C):134–152. https://doi.org/10.1016/j.jmapro.2016.11.003. http://www.sciencedirect.com/science/article/pii/S152661251630158X

4. David SA, DebRoy T (1992) Current issues and problems in welding science. Science 257(5069):497–502. https://doi.org/10.1126/science.257.5069.497. http://science.sciencemag.org/content/257/5069/497

5. Jebaraj AV, Ajaykumar L, Deepak C, Aditya K (2017) Weldability, machinability and surfacing of commercial duplex stainless steel AISI2205 for marine applications - a recent review. J Adv Res 8(3):183–199. https://doi.org/10.1016/j.jare.2017.01.002. http://www.sciencedirect.com/science/article/pii/S2090123217300115

6. Chiumenti M, Cervera M, Dialami N, Wu B, Jinwei L, de Saracibar CA (2016) Numerical modeling of the electron beam welding and its experimental validation. Finite Elem Anal Des 121(Supplement C):118–133. https://doi.org/10.1016/j.finel.2016.07.003. http://www.sciencedirect.com/science/article/pii/S0168874X16301378

7. Kaur A, Ribton C, Balachandaran W (2015) Electron beam characterisation methods and devices for welding equipment. J Mater Process Technol 221(Supplement C):225–232. https://doi.org/10.1016/j.jmatprotec.2015.02.024. http://www.sciencedirect.com/science/article/pii/S0924013615000679

8. Węglowski M, Bacha S, Phillips A (2016) Electron beam welding–techniques and trends–review. Vacuum 130(Supplement C):72–92. https://doi.org/10.1016/j.vacuum.2016.05.004. http://www.sciencedirect.com/science/article/pii/S0042207X16301245

9. International electron beam welding conference: Lectures of the 2nd IEBW conference taking place in aachen on march 26-30 (2012) vol 285, DVS Media GmbH, Dusseldorf

10. Alali M, Todd I, Wynne B (2017) Through-thickness microstructure and mechanical properties of electron beam welded 20mm thick aisi 316l austenitic stainless steel. Mater Des 130(Supplement C):488–500. https://doi.org/10.1016/j.matdes.2017.05.080. http://www.sciencedirect.com/science/article/pii/S0264127517305610

11. Wang Y, Fu P, Guan Y, Lu Z, Wei Y (2013) Research on modeling of heat source for electron beam welding fusion-solidification zone. Chin J Aeron 26(1):217–223. https://doi.org/10.1016/j.cja.2012.12.023. http://www.sciencedirect.com/science/article/pii/S1000936112000313

12. Ziolkowski M, Brauer H (2009) Modelling of seebeck effect in electron beam deep welding of dissimilar metals. COMPEL - Int J Comput Math Electr Electron Eng 28(1):140–153. https://doi.org/10.1108/03321640910918940

13. Rai R, Burgardt P, Milewski JO, Lienert T, DebRoy T (2009) Heat transfer and fluid flow during electron beam welding of 21cr–6ni–9mn steel and ti–6al–4v alloy. J Phys D: Appl Phys 42(2):025503. http://stacks.iop.org/0022-3727/42/i=2/a=025503

14. Chiumenti M, Cervera M, Dialami N, Wu B, Jinwei L, de Saracibar CA (2016) Numerical modeling of the electron beam welding and its experimental validation. Finite Elements Anal Des 121:118–133. https://doi.org/10.1016/j.finel.2016.07.003. http://www.sciencedirect.com/science/article/pii/S0168874X16301378

15. Huang B, Chen X, Pang S, Hu R (2017) A three-dimensional model of coupling dynamics of keyhole and weld pool during electron beam welding. Int J Heat Mass Transf 115:159–173. https://doi.org/10.1016/j.ijheatmasstransfer.2017.08.010. http://www.sciencedirect.com/science/article/pii/S0017931017310608

16. Kar J, Roy SK, Roy GG (2016) Effect of beam oscillation on electron beam welding of copper with aisi-304 stainless steel. J Mater Process Technol 233(Supplement C):174–185. https://doi.org/10.1016/j.jmatprotec.2016.03.001. http://www.sciencedirect.com/science/article/pii/S0924013616300577

17. Babu NK, Raman SGS, Murthy CVS, Reddy GM (2007) Effect of beam oscillation on fatigue life of ti–6al–4v electron beam welments. Mater Sci Eng: A 471(1):113–119. https://doi.org/10.1016/j.msea.2007.03.040. http://www.sciencedirect.com/science/article/pii/S0921509307005357

18. Dinda SK, Sk MB, Roy GG, Srirangam P (2016) Microstructure and mechanical properties of electron beam welded dissimilar steel to fe–al alloy joints. Mater Sci Eng: A 677(Supplement C):182–192. https://doi.org/10.1016/j.msea.2016.09.050. http://www.sciencedirect.com/science/article/pii/S0921509316311108

19. Kar J, Dinda SK, Roy GG, Roy SK, Srirangam P (2018) X-ray tomography study on porosity in electron beam welded dissimilar copper–304ss joints. Vacuum 149:200–206. https://doi.org/10.1016/j.vacuum.2017.12.038. http://www.sciencedirect.com/science/article/pii/S0042207X17314896

20. Trushnikov D, Koleva E, Mladenov G, Belenkiy VY (2013) Effect of beam deflection oscillations on the weld geometry. J Mater Process Technol 213(9):1623–1634. https://doi.org/10.1016/j.jmatprotec.2013.03.028. http://www.sciencedirect.com/science/article/pii/S0924013613001209

21. Wang L, Gao M, Zhang C, Zeng X (2016) Effect of beam oscillating pattern on weld characterization of laser welding of aa6061-t6 aluminum alloy. Mater Des 108(Supplement C):707–717. https://doi.org/10.1016/j.matdes.2016.07.053. http://www.sciencedirect.com/science/article/pii/S0264127516309534

22. Kar J, Roy SK, Roy GG (2017) Effect of beam oscillation on microstructure and mechanical properties of aisi 316l electron beam welds. Metall and Mater Trans A 48(4):1759–1770. https://doi.org/10.1007/s11661-017-3976-2

23. RajaKumar G, Janaki Ram GD, Koteswara Rao SR (2015) Effect of beam oscillation on borated stainless steel electron beam welds. Mater Test 57(6):489–494. https://doi.org/10.3139/120.110740

24. Ferreño D., Carral JP, Calderón RL, Álvarez JA, Gutiérrez-Solana F (2017) Development and experimental validation of a simplified finite element methodology to simulate the response of steel beams subjected to flame straightening. Construct Build Mater 137(Supplement C):535–547. https://doi.org/10.1016/j.conbuildmat.2017.02.001. http://www.sciencedirect.com/science/article/pii/S0950061817301769

25. Lacalle R, Álvarez J, Ferreño D, Portilla J, Ruiz E, Arroyo B, Gutiérrez-Solana F. (2013) Flame straightening application on structural steels: Effects on mechanical and fracture properties, 0. https://doi.org/10.1201/b15963-76

26. Sun X, Choi K, Liu W, Khaleel M (2009) Predicting failure modes and ductility of dual phase steels using plastic strain localization. Int J Plast 25(10):1888–1909. https://doi.org/10.1016/j.ijplas.

2008.12.012. http://www.sciencedirect.com/science/article/pii/S0749641908001897

27. Ramazani A, Mukherjee K, Schwedt A, Goravanchi P, Prahl U, Bleck W (2013) Quantification of the effect of transformation-induced geometrically necessary dislocations on the flow-curve modelling of dual-phase steels. Int J Plast 43:128–152. https://doi.org/10.1016/j.ijplas.2012.11.003. http://www.sciencedirect.com/science/article/pii/S0749641912001684

28. Tasan C, Hoefnagels J, Diehl M, Yan D, Roters F, Raabe D (2014) Strain localization and damage in dual phase steels investigated by coupled in-situ deformation experiments and crystal plasticity simulations. Int J Plast 63:198–210. deformation Tensors in Material Modeling in Honor of Prof. Otto T. Bruhns. https://doi.org/10.1016/j.ijplas.2014.06.004. http://www.sciencedirect.com/science/article/pii/S0749641914001260

29. Minami H, Nakayama K, Morikawa T, Higashida K, Toji Y, Hasegawa K (2011) Effect of tempering conditions on inhomogeneous deformation behavior of ferrite-martensite dual-phase steels. Tetsu-to-Hagane 97(9):493–500. https://doi.org/10.2355/tetsutohagane.97.493

30. Hasegawa K, Toji Y, Minami H, Ikeda H, Morikawa T, Higashida K (2012) Effect of martensite fraction on tensile properties of dual-phase steels. Tetsu-to-Hagane 98(6):320–327. https://doi.org/10.2355/tetsutohagane.98.320

31. Tasan C, Diehl M, Yan D, Bechtold M, Roters F, Schemmann L, Zheng C, Peranio N, Ponge D, Koyama M, Tsuzaki K, Raabe D (2015) An overview of dual-phase steels: Advances in microstructure-oriented processing and micromechanically guided design. Annu Rev Mater Res 45(1):391–431. https://doi.org/10.1146/annurev-matsci-070214-021103

32. Zheng C, Raabe D (2013) Interaction between recrystallization and phase transformation during intercritical annealing in a cold-rolled dual-phase steel: A cellular automaton model. Acta Mater 61(14):5504–5517. https://doi.org/10.1016/j.actamat.2013.05.040. http://www.sciencedirect.com/science/article/pii/S1359645413004187

33. EN-5173:2010+A1:2011 (2010) Destructive tests on welds in metallic materials. bend tests, European committee for Standardization

34. Han R, Lu S, Dong W, Li D, Li Y (2015) The morphological evolution of the axial structure and the curved columnar grain in the weld. J Cryst Growth 431(Supplement C):49–59. https://doi.org/10.1016/j.crysgro.2015.09.001. http://www.sciencedirect.com/science/article/pii/S0022024815005473

35. Lienert T, Siewert T, Babu S, Acoff V (2011) ASM handbook, vol 6A. ASM International, Ohio

36. Komerla K, Naumov A, Mertin C, Prahl U, Bleck W (2018) Investigation of microstructure and mechanical properties of friction stir welded aa6016-t4 and dc04 alloy joints. Int J Adv Manuf Technol 94(9):4209–4219. https://doi.org/10.1007/s00170-017-1022-6

37. Sadowski AJ, Rotter JM, Stafford PJ, Reinke T, Ummenhofer T (2017) On the gradient of the yield plateau in structural carbon steels. J Construct Steel Res 130(Supplement C):120–130. https://doi.org/10.1016/j.jcsr.2016.11.024. http://www.sciencedirect.com/science/article/pii/S0143974X16304771

Affiliations

Krishna Komerla[1] · Stefan Gach[2] · Thomas Vossel[3] · Alexander Schwedt[4] · Andreas Bührig-Polaczek[3] · Uwe Reisgen[2] · Wolfgang Bleck[5]

Stefan Gach
gach@isf.rwth-aachen.de

Thomas Vossel
T.Vossel@gi.rwth-aachen.de

Alexander Schwedt
schwedt@gfe.rwth-aachen.de

Andreas Bührig-Polaczek
sekretariat@gi.rwth-aachen.de

Uwe Reisgen
reisgen@isf.rwth-aachen.de

Wolfgang Bleck
bleck@iehk.rwth-aachen.de

[1] Steel Institute IEHK, RWTH Aachen University, Intzestr. 1, 52072 Aachen, Germany

[2] Welding and Joining Institute ISF, RWTH Aachen University, Pontstr. 49, 52062 Aachen, Germany

[3] The Foundry Institute GI, RWTH Aachen University, Intzestr. 5, 52072 Aachen, Germany

[4] Central Facility for Electron Microscopy GFE, RWTH Aachen University, Ahornstr. 55, 52074 Aachen, Germany

[5] Steel Institute IEHK, RWTH Aachen University, Aachen, Germany

3.2 Publication II

Investigation of Microstructure and Mechanical Properties of Friction Stir Welded AA6016-T4 and DC04 Alloy Joints
K. Komerla, A. Naumov, C. Mertin, U. Prahl, W. Bleck (2018), The International Journal of Advanced Manufacturing Technology 94(9):4209–4219. https://doi.org/10.1007/s00170-017-1022-6

Highlights

- A mode of dissimilar friction stir welding where minimal shear strain accumulation in steel and complete dynamic recrystallization of aluminum was achieved through tool offset

- Bending susceptibility of weld joints due to the application of high axial loads during welding was identified and a force regulator was adapted to enhance the weld joints performance

- A semi-empirical approach to predicting hardness across the various regions of weld joint based on their respective volume weighted grain size calculations was developed

CrossMark

ORIGINAL ARTICLE

Investigation of microstructure and mechanical properties of friction stir welded AA6016-T4 and DC04 alloy joints

Krishna Komerla[1] · Andreas Naumov[2] · Chris Mertin[3] · Ulrich Prahl[1] · Wolfgang Bleck[1]

Abstract In this study, the microstructure and mechanical properties of dissimilar friction stir welded aluminum and steel joints were investigated, in order to understand the role of tool offset in the enhancement of weld properties. Conventional techniques like light-optical microscopy, electron back scatter diffraction, energy dispersive spectroscopy, and indentation tests were utilized to characterize the joints. Tool offset resulted in a mode of welding where minimal shear strain accumulation in steel and complete dynamic recrystallization of aluminum were achieved. Additionally, macroscopically defect and inter-metallic compound free joints were obtained, with only a small fraction of Fe chips embedded in the aluminum matrix. Through plastic deformation and thermal effects, significant differences in grain size and micro-hardness were observed in the various regions of the welded joint. Due to high temperatures and strain rates, dynamic recrystallization was activated in aluminum. The kernel average misorientation map revealed the lack of stored deformation energy in the microstructure, indicating the presence of fully recrystallized grains. Due to its high thermal stability, steel did not recrystallize but, exhibited marginal grain growth in both thermomechanically affected zone and heat-affected zone. It also contained a highly refined grain structure in the weld zone. The texture maps plotted for the weld zone of Fe alloy showed weak shear texture indicating minimal shear strain accumulation. A good correlation between the experimental and predicted hardness was observed in steel. In the aluminum alloy, however, prediction was overestimation as the additional softening due to dynamic recrystallization and dissolution or coarsening of precipitates was not taken into account by the model.

✉ Krishna Komerla
  kkomerla@iehk.rwth-aachen.de

  Andreas Naumov
  naumov@isf.rwth-aachen.de

  Chris Mertin
  mertin@ibf.rwth-aachen.de

  Ulrich Prahl
  ulrich.prahl@iehk.rwth-aachen.de

  Wolfgang Bleck
  wolfgang.bleck@iehk.rwth-aachen.de

1 Steel Institute IEHK, RWTH Aachen University, Intzestr. 1, 52072 Aachen, Germany

2 Welding and Joining Institute ISF, RWTH Aachen University, Pontstr. 49, 52062 Aachen, Germany

3 Institute of Metal Forming IBF, RWTH Aachen University, Intzestr. 10, 52056 Aachen, Germany

1 Introduction

Today the production of stronger and lighter products using energy efficient and eco-friendly materials has become essential in the manufacturing industry. The automotive sector in its attempt to reduce weight while maintaining strength, has substituted some parts of steel structures with lighter aluminum alloys [1, 2]. However, the distinct physical and chemical properties of aluminum and steel led to new challenges in welding and joining both materials together. The fundamental problem with welding these

⌷ Springer

materials using conventional techniques is the occurrence of detrimental inter-metallic compounds (IMCs), that are prone to micro-cracking [3–7]. Under such circumstances, friction stir welding (FSW), a solid-state welding technique, has proven to be an effective solution in joining such difficult-to-weld materials with low energy input and better repeatability [8]. In this method, joints can be created at temperatures below the melting point of materials and thus the formation of IMCs can be prevented.

FSW technology has proven to be advantageous in diverse fields of application. In the automotive industry, it is used in welding components like drive shafts, cylinder heads, engine blocks, chassis cradles, tailor welded blanks, etc. Recently, Honda integrated this technology in the assembly lines for welding a vehicles suspension system, claiming enhanced mechanical properties and reduced production costs [9]. In the railway sector, hollow profiles and T-stiffer extrusions used in structural construction of train cars are being friction stir welded to reduce distortion and shrinkage. Hitachi were among the first to use friction stir welded aluminum floor elements in their high-speed train coaches to reduce weight. In the aviation sector, FSW process offered tremendous potential for low cost joining of lightweight aluminum airframes. The European aeronautic defense and space company presented data showing that the mechanical properties of these welds were close to their parent materials [10]. Beside the advantages, FSW also faces considerable limitations such as low welding speed, necessity for rigid clamping, the key hole at the end of each weld etc. Hence, there is a strong need for further research and development in this field to overcome such limitations.

The process of FSW involves a cylindrical tool comprising a shoulder and a profiled pin which is rotated and slowly plunged into workpieces that are butted or lapped together. This non-consumable rotating tool not only generates enough frictional heat needed to soften the workpieces but also causes a stirring effect that leads to material flow about the path the tool traverses. Tool geometry and the contact load are considered to be the prime factors that control the material flow and heat input, and in turn the quality of weld. Kumar et al. [11] presented a detailed study on the influence of the welding tool on material flow and weld formation. It was reported that with increasing axial load, the defect size was reduced and, beyond a critical value of the axial load, defects were completely eliminated. During welding, material on the surface and subsurface is pushed downwards under the action of the tool shoulder while material is pushed upwards from the cavity by the pin. As the tool advances, material from the leading edge fills the space created behind the pin in the form of stacked layers. A dynamic balance must be established between the downward flow of material from the surface and subsurface with the upward flow of material in the weld cavity to produce defect free

welds. High axial loads along with tool offsetting were found to be beneficial in controlling the fraction of IMCs and in production of defect free joints during FSW of dissimilar metals [12, 13]. Offsetting restricts the pin stirring action and reduces the base materials mixing and consequently inhibits the formation of brittle IMCs. However, recently, Pourali et al. [14] have shown that the presence of Fe-rich intermetallics like FeAl or Fe_3Al were not detrimental to the weld strength. It has also been reported that a backward tool tilt can further enhance the flow of material along the trailing edge under the shoulder and thereby eliminate defects [15].

Typically, the weld morphology comprises a weld zone (WZ) where large plastic deformation and heat result in fine recrystallized and equiaxed grains, the thermo-mechanically affected zone (TMAZ) with elongated grains and the heat-affected zone (HAZ). The HAZ typically shows thermal softening without any plastic deformation resulting in grain growth and over-aging of particles especially in precipitation hardened alloys.

In their previous study, authors combined high axial load, tool tilt and offset toward the retreating side together with different rotational speeds and feed rates in an attempt to obtain optimally welded joints [16]. As a result, defect free and IMCs free joints with a tensile strength ratio of 85% in comparison to the aluminum base material were obtained. The reason for the improved strength can be attributed to the post-weld microstructure and to the underlying metallurgical phenomena. In order to obtain sustainable joints, it is critical to understand the impact of various microstructural aspects such as grain size, morphology, dislocation density, precipitates and texture on the final mechanical properties of the weldments.

The aim of this present work is to study the microstructural features and their impact on the final welded joint properties. Light optical microscopy (LOM), electron backscatter diffraction (EBSD), energy dispersive X-ray spectroscopy (EDS), and Vickers micro-hardness indentation were used to characterize the butt welds of AA6016-T4 and DC04 alloys. Micro voids or crack free weld cross sections with only a few embedded Fe fragments in the aluminum matrix were obtained. A mode of welding with complete dynamic recrystallization in aluminum and minimal shear strain accumulation in steel was achieved. Grain refinement and growth through plastic deformation and diffuse heat were evident from the LOM and EBSD results. The optical micrographs were analyzed and the variation of grain size among the different weld regions were presented in the form of cumulative probability distribution (CPD) plots. Also, a semi-empirical approach to hardness prediction was presented. A model based on the average grain size was used to predict the hardness. It provided a good correlation between predicted and experimental results in steel but,

Table 1 Chemical composition (in weight %) of DC04 and AA6016-T4 alloys

element	C	Si	Mn	P	S	Mg	Cr	Cu	Al	Ti	Fe
Al6016-T4	–	1.31	0.06	–	–	0.32	0.001	0.009	98.07	0.01	0.19
DC04	0.008	0.008	0.19	0.008	0.005	–	0.015	0.007	0.037	0.029	99.6

overestimated hardness in the aluminum alloy. The model was unable to account for the additional softening caused recrystallization in aluminum. EBSD results revealed minimal shear strain accumulation in steel due to the applied tool offset. Thermal softening, dissolution, or coarsening of precipitates were also discussed as reasons for the variation of Vickers hardness in the weld regions.

2 Materials and methods

2.1 Materials

The sheet materials investigated in this study were a deep drawing mild steel (DC04) with a thickness of 0.96 mm and a solution heat treated and aged aluminum AA6016-T4 alloy with a thickness of 1.12 mm. The chemical composition of both alloys is presented in Table 1 for reference.

2.2 Experimental methods

The dissimilar blanks of Fe-Al were butt-welded using a position-controlled friction stir welding machine. The setup comprises a conventional three-axis NC-controlled milling machine with a maximum spindle power of 7.5 kW, a tungsten carbide rotation tool cemented with cobalt, and a special clamping system. A schematic drawing of the weld setup depicting the tool position, tilt, and welding direction is presented in Fig. 1. The tool geometry and design are shown in Fig. 2a. An inward curvature between the tool pin and shoulder was provided to stop material sliding out, from underneath the tool during welding. As reported by Tanaka

et al. [17] in case of dissimilar FSW of hard and soft materials, the tool plunges into the softer material placed on the retreating side, as it is well known that much of material flow occurs along the retreating side [18]. Therefore, aluminum was positioned on the retreating side, while steel was placed on the advancing side. A rotational speed of 900 rpm, a tilt angle of 1°, a lateral displacement of +3 mm on the retreating side and a feed rate of 250 mm/min were utilized.

A wire shaped thermo-couple with a diameter of 1 mm was placed in grooves made on the work bench in order to observe the temperature evolution. Due to the axial pressure exerted by the tool, both sheets were pressed against the thermo-couple and the measurement was performed directly under the weld seam. An image of the work bench with thermo-couple is shown in Fig. 2b. A peak temperature of 515 °C, as seen in Fig. 2c was observed directly underneath the tool pin. It is about 90% of the melting temperature of the Al6016-T4 alloy.

For microscopy, few samples were cut across the weld line and were mechanically polished up to 1 μm with diamond paste for 20 ± 1 min and then up to 0.1 μm with colloidal silica particles to minimize topology and surface relief. For EBSD measurements, samples were further electro-polished and anodized to smooth out any remaining artefacts. EBSD maps were acquired on a Schottky field emission gun scanning electron microscope (SEM), JEOL JSM-7000F (JEOL Ltd.) equipped with a Hikaki camera and TSL OIM software. An accelerating voltage of 20 kV, step size of 100 nm on a hexagonal grid and dwell time of 7 ms were used for the measurement. After dynamic background subtraction, the intensity of diffraction patterns was normalized and points with a confidence index less than 0.1
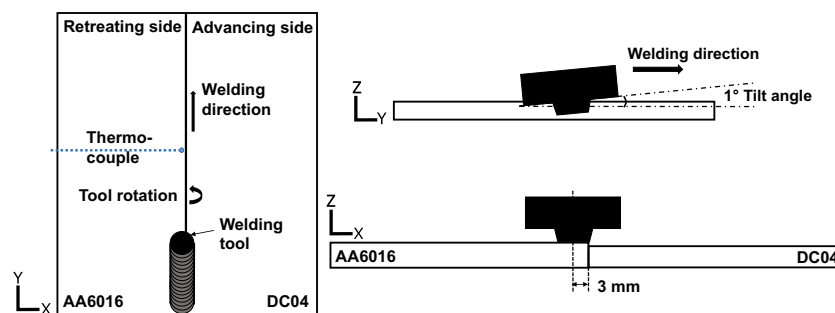

Fig. 1 Schematic representation showing (left) work-pieces in butt-weld configuration with aluminum on the retreating side and steel on the advancing side, welding direction, tools rotational direction and thermo-couple position for temperature measurement. Tool (right) off-set of 3 mm on the retreating side and tilt of 1° to the top surface [16]
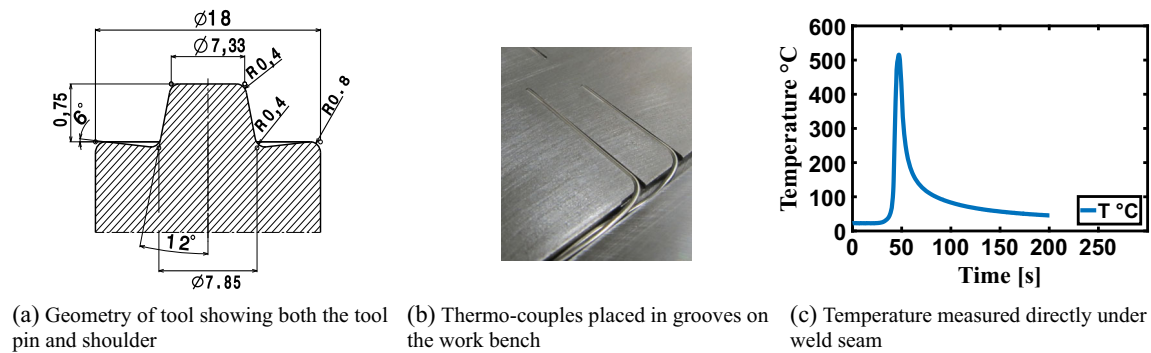
(a) Geometry of tool showing both the tool pin and shoulder

(b) Thermo-couples placed in grooves on the work bench

(c) Temperature measured directly under weld seam

Fig. 2 Tool geometry; embedded thermo-couples; temperature profile measured by the embedded thermocouple underneath the weld seam

were discarded. Grains were delimited to a 5° misorientation criterion and the kernel average misorientation (KAM) was calculated from the misorientation over a distance of 100 nm.

Micro-hardness was measured in the various regions of the welded joint on the transverse section, with an indentation load of 50 g and dwell time of about 15 s. The hardness values were obtained to observe the hardening and softening across the various regions of the welded joint.

2.3 Grain size analysis

The grain size distributions were plotted by analyzing the optical micrographs taken from various regions of the welded joint. Figure 3 depicts the processed image of a micrograph obtained from the HAZ of Al alloy. The grain boundaries were retraced and the image was converted to binary mode, where grain boundaries were represented in white and grain interiors in black. This image processing was performed to facilitate the measurement of grain size using the Matlab software image processing tool box. Grains with partially visible grain boundaries were discarded for the sake of accuracy.

Gundersen et al. presented a point-sampled intercept length method to calculate the grain size which was later extended, to include a direction based volume-weighted averaging scheme by Lehto et al. [19–21]. A Matlab implementation of the extended approach is utilized to analyze

the binary image data and quantify the average grain size. In this method, the grain size (d_i) for each grain is measured by taking the length of a linear intercept drawn for a test point chosen at random in the grain interior. A randomly chosen black pixel in the grain interior forms the test point and length of all the pixels measured along a line to the left and right of the test point put together forms the length of the intercept. This process is repeated numerous times covering at least 25% of the total points in a grain with intercepts drawn in four different directions (0°, 45°, 90°, 135°) to ensure accuracy and to obtain a densely measured grain size.

A stereological relationship between the surface area fraction and the volume fraction was assumed to weight the grain size, as shown below

$$\frac{A_i}{A_T} \approx \frac{V_i}{V_T} \tag{1}$$

where A_i and V_i are the surface area and volume of the grain i, A_T and V_T are the total surface area and total volume of all the included grains. The volume weighted average grain size (d_v) is then calculated as

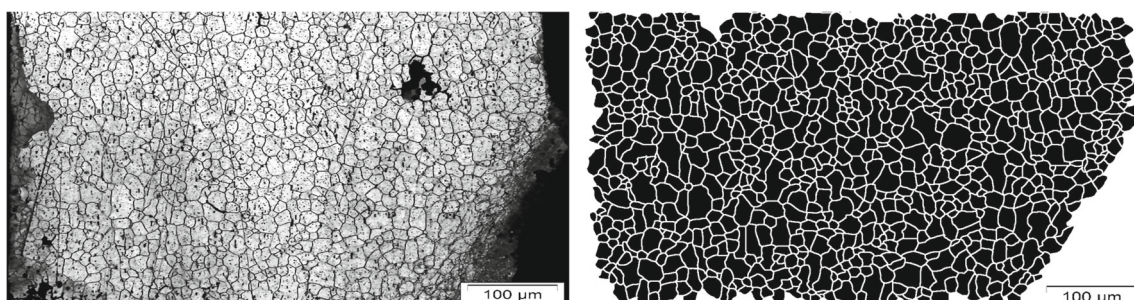$$d_v = \frac{1}{V_T} \sum_{i=1}^{n} V_i d_i \tag{2}$$

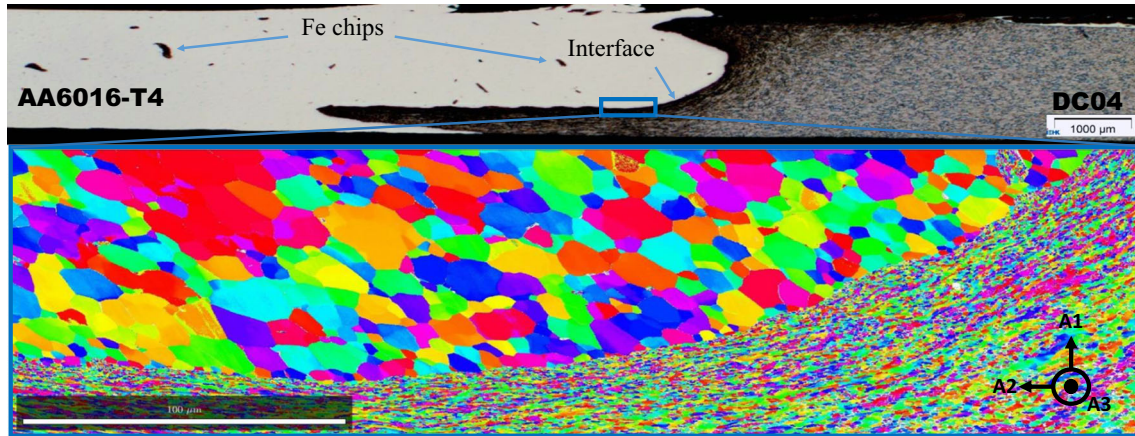**Fig. 3** Optical micrograph obtained from the HAZ of the Al alloy and the processed image

Fig. 4 Transverse sectional micrograph showing the interface, embedded Fe chips and EBSD map of the interface containing deformed Fe grains and recrystallized Al grains; The reference coordinate system showing the transverse direction (A1), normal direction (A2) and welding direction (A3)

3 Results and discussion

3.1 Weld microstructure

In accordance with the standard AWS D17.3/D17.3M:2010 for friction stir welding of aluminum alloys, there is are no inner and outer defects at produced weld seams, like significant flash, incomplete joint penetration, cavity or surface-breaking voids. The conventional optical micrograph and EBSD map of the weld interface with deformed Fe grains and recrystallized Al grains is presented in Fig. 4. It includes the stir zone, interface, and chips of Fe (DC04) embedded in the aluminum matrix. Abbasi et al. [5] presented the adverse effects of such embedded fragments on the joint. It was reported that such fragments act as discontinuities and stress concentration points that are detrimental to the static and dynamic load bearing capacity of the joint.

In dissimilar FSW, embedded chips are created when material from the surface of the harder material is removed, transported and pressed into the softer matrix by the tool shoulder. Therefore, minimizing the interaction of the tool shoulder with the hard material could potentially reduce the fraction of embedded chips. By offsetting the tools placement away from the Fe alloy, such minimized tool interaction was achieved. As a result, only smaller fractions of Fe chips were transported to the Al alloy. The presence of embedded Fe chips in the joint can only be reduced but not entirely avoided. High axial load, rotational speed, and excessive plastic deformation make their occurrence inevitable. The tool offset not only resulted in fewer and smaller Fe chips being embedded in the aluminum matrix but also in micro-crack free, void free and IMC free weld cross sections. A selected area at the interface with higher magnification, as shown in Fig. 5, together with the EDS measurement confirmed the absence of IMCs. The joint was

solely formed by interlocking of the asperities as aluminum was smeared atop steel under the force exerted by the tool.

3.2 Grain size

Grain size has a significant influence on the mechanical properties of polycrystalline materials. With enough stress and thermal energy, dislocations glide through the lattice distorting the crystal until their motion is impeded at the grain boundaries. The repulsive force generated by the subsequent pile up of such dislocations at the grain boundary reduces the energy barrier for dislocation motion across the grain boundary. Decreasing the grain size decreases the amount of pile up and increases the applied stress required to drive dislocations across the grain boundaries. Fine sized grains exhibit increased strength due to such hardening
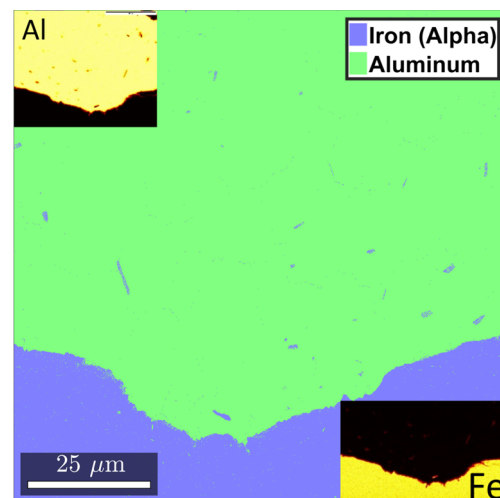

Fig. 5 EBSD phase map with EDS of the interface showing both Al and Fe distribution
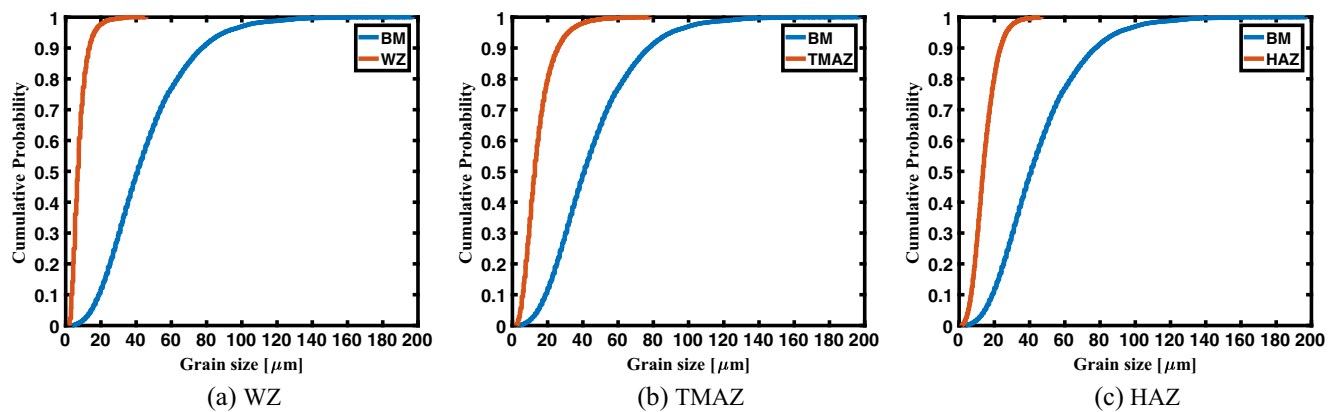
Fig. 6 Cumulative probability distribution of grain size (μ*m*) in the various weld regions of aluminum

effect where greater ratios of grain boundary to dislocations are seen. In the friction stir welding process, depending on the welding parameters, a wide range of grain sizes are produced in the welded sections. To achieve optimal strength and uniform elongation, it is imperative to understand the grain size distribution and its influence on the mechanical properties of the welded joint.

The microstructure of AA6016-T4 consisted of equiaxed grains with an average grain size of 40 μm in the as obtained state. However, significantly smaller grain sizes were observed in the post-weld microstructure. The tool offset imposed extensive tool contact in the Al alloy, resulting in large plastic deformation and high peak temperature. The effect of tool is evident from the cumulative probability distribution (CPD) of grain size of the various regions of the welded joint. The plots shown in Fig. 6 present the CPD of grain size in the WZ, TMAZ, and HAZ of the Al alloy. For comparison, the grain size distribution of its base material (BM) was also added to each of the plots. A shift in the CPD to the left of the BM can be clearly seen. An average grain size of 14 μm in the HAZ and TMAZ and about 8 μm in the WZ were observed.

In comparison, the CPD of the Fe alloy presented in Fig. 7 shows a very different trend. The initial microstructure of DC04 alloy contained ferritic grains with an average size of 20 μm. After welding, the regions close to the effective pin surface (WZ) contained very fine grains with an average grain size of 1.5 μm. Away from the interface in the TMAZ and HAZ, marginal increase in grain size was observed. A shift in the CPD of grain size beyond the BM can be clearly seen. Grain refinement was dominantly seen only in the upper layers of the workpiece close to the tool shoulder, while most part of the inner layers remained unaffected by the tool. However, with sufficient thermal activation, due to diffuse heat from welding, grains grew in size. This effect is especially seen in the HAZ, where the average grain size was up to 3 μm bigger than the base material.

Despite significant influence of the welding tool, the WZ of the Al alloy showed grains larger than that of Fe alloy, suggesting dominant thermal kinetics along with plastic deformation. Recrystallization and grain growth are probable causes for the increased grain size in the WZ. They are usually thermal driven mechanisms, achieved in materials
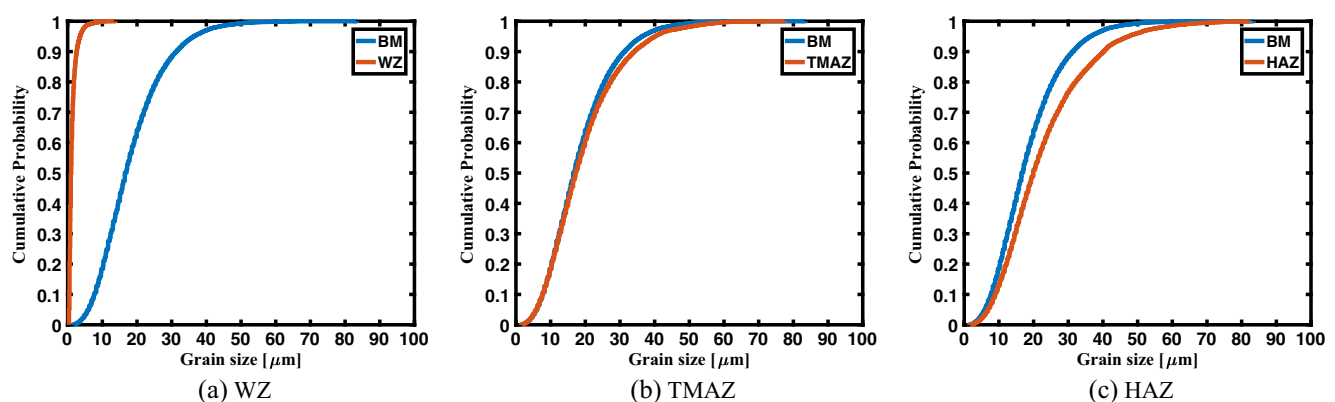

Fig. 7 Cumulative probability distribution of grain size (μ*m*) in the various weld regions of steel
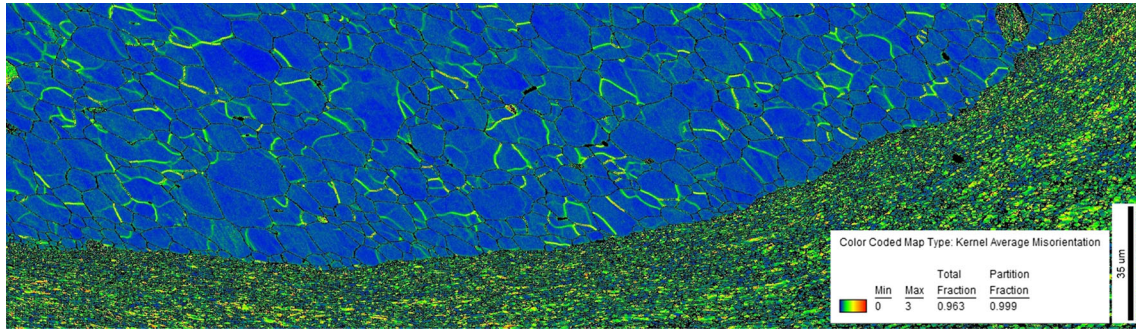
Fig. 8 EBSD kernel average misorientation (KAM) map of the Al-Fe interface

at temperatures higher than 40% of their melting temperature (T_m). The combined effect of stirring and frictional heat caused dynamic recrystallization of microstructure in the Al alloy. New defect free grains nucleated and grew consuming the deformed grains. With the help of EBSD, recrystallized grains were detected by observing the lack of any visible deformation within the grains [22]. The KAM map presented in the Fig. 8 shows that the misorientation between the aluminum grains is small and less than 1° degree. Merely a small fraction of the deformation energy was stored within these crystals, hence it is safe to consider them to be recrystallized grains.

On the other hand, the DC04 alloy due to its high melting temperature and the tool offset limiting the fraction of diffuse heat, exhibited better thermal stability. It is evident from the KAM map that recrystallization did not take place in the Fe alloy. However, the tools axial force and stirring effect introduced severe plastic deformation in the WZ, which in turn generated enormous amounts of dislocations. These large number of dislocations rearranged themselves in to energetically stable structures such as geometrically necessary boundaries (GNBs) to minimize the strain energy produced during deformation [23]. The original grain was thus subdivided by these GNBs into smaller grains. The density of GNBs increased with the plastic strain while the size of the grains subdivided decreased. Thus, very fine grains were produced in the WZ.

3.3 Micro-hardness

Vickers micro-hardness was measured in order to study the effects of plastic deformation and diffuse heat on the microstructure. Hardness measurements were carried out along two different directions as indicated in the Fig. 9.

1. Perpendicular to the tool axis across the weld
2. Parallel to the tool axis along the sheet thickness

3.3.1 Micro-hardness in DC04 alloy

In the Fe alloy, higher work hardening was observed in layers directly in contact with the effective tool surface. Hardness measured in the individual regions of the welded joint, parallel to the tool axis is presented in Fig. 10a. High hardness was seen close to the top surface in the WZ, which then decreases drastically as the distance from the top surface along the thickness increases. Such a variation of hardness indicates susceptibility of the joint to bending loads, micro-cracks could develop on the surface and grow inward resulting in failure. A similar decreasing trend was also observed in the TMAZ where higher hardness was seen close to the top surface. It is evident that the tooling forces introduce high degree of deformation in the upper layers which could lead to potential failure. The HAZ, however, exhibited a linear hardness profile with values close to the BM.
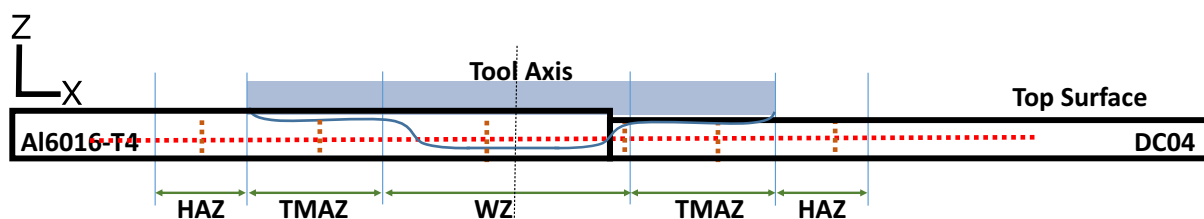

Fig. 9 A schematic representation, showing tool in plunged position, tool axis and weld regions. The dotted lines indicate the position where indentation measurements were made in the weld regions (both perpendicular and parallel to the tool axis)

Fig. 10 MH profiles measured parallel to tool axis in various weld zones of Fe and Al alloys

(a) MH along thickness in Fe alloy

(b) MH along thickness in Al alloy
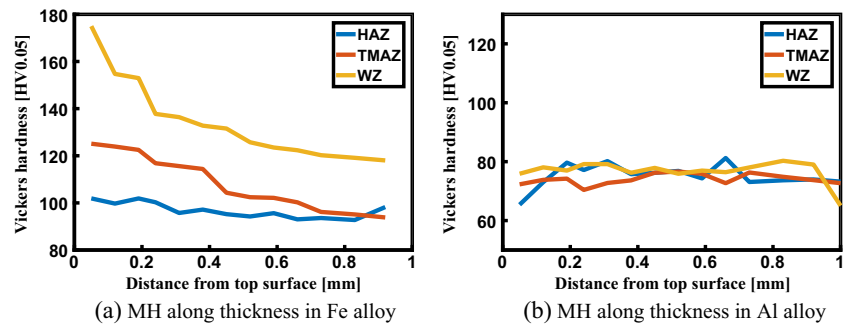
Perpendicular to the tool axis, a decreasing MH profile was observed from WZ to the HAZ as seen in Fig. 11. The hardness across the HAZ was similar to BM. Influence of plastic deformation and resulting strain hardening was evident from the higher hardness in the WZ and TMAZ. In the HAZ, no significant difference in strength was observed due to the lack of tool induced deformation and softening by frictional heat.

3.3.2 Micro-hardness in AW6016-T4 alloy

Generally grain refinement due to plastic deformation results in enhanced strength due to hardening arising from increased dislocation density. However, deformation under the tool's influence at high strain rates combined with high temperature forced the dynamic recrystallization of microstructure where new grains nucleated and grew at the expense of the deformed grains.

Al alloy acquired its strength by virtue of precipitation hardening through the ageing process. It involves solution treatment, followed by natural aging to facilitate the formation of particles of a second phase that impedes the dislocation movement and force dislocations to either cut through or circumvent them and thus strengthens the alloy [24]. During welding, with peak temperatures above 500 °C the dissolution of precipitates begins and with sufficient time the precipitates would be completely re-solutionized. The decrease in precipitate density also reduces the strength of the alloy. Despite dynamic recrystallization and dissolution of precipitates, Al alloy showed no significant variation in the hardness measured along both directions from BM to WZ, as seen in Figs. 10b and 11. The decrease in strength due to thermal effects could have been compensated by the reduced grain size in the post-weld microstructure and re-precipitation of secondary phase particles during cooling. Further study needs to be conducted to thoroughly understand the precipitation kinetics taking place during the heating and cooling cycles of the welding process.

3.4 Prediction of hardness

A semi-empirical approach to calculating hardness is presented here. In general, materials hardness can be directly related to grain size on the basis of Hall-Petch relationship [25, 26].

$$H = H_0 + \frac{K_{hv}}{\sqrt{d_{avg}}} \quad where \begin{cases} H_0 \ \& \ K_{hv} \ \text{are material constants} \\ d_{avg} \ \text{is the average grain size} \end{cases} \quad (3)$$

However, a relationship based only on the average grain size of the microstructure was found to be unsuitable when quantifying heterogeneous microstructures, as it fails to realize that a small number of large grains with low strength still occupy a significant material volume [27–32]. Therefore, a volume-weighted approach as discussed in Section 2.3 has been considered in analyzing the optical micrographs obtained from different regions of the welded joint.

A comparison of predicted hardness calculated from the volume-weighted average grain size and mean hardness values of the different weld regions obtained experimentally was presented in Table 2. A linearly increasing hardness profile that fits with the experimental observation was predicted for the Fe alloy. However, the prediction was underestimated with an error fraction of 10% in the
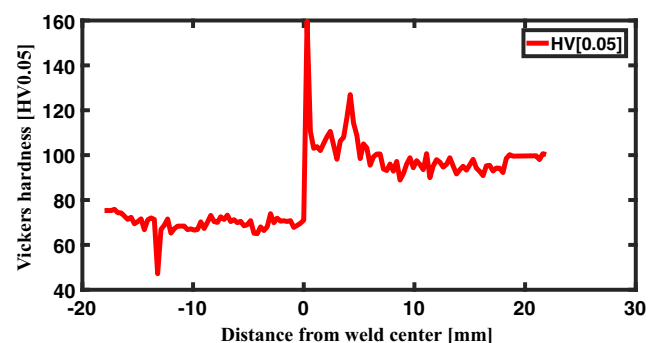

Fig. 11 MH measured perpendicular to the tool axis across the weld joint

Table 2 List of volume-weighted average grain sizes, experimental and predicted Vickers hardness obtained from various regions of the welded joint

| Zone	BM	HAZ	TMAZ	WZ
	Al6016-T4	$K_{hv} = 70.0$	$H_0 = 64.5$	
d_{avg}	45.2	14.5	14.6	7.9
$HV_{Predicted}$	75.0	82.9	82.8	89.4
$HV_{Experimental}$	75.0	75.3	74.0	76.8
	DC04	$K_{hv} = 65.0$	$H_0 = 80.0$	
d_{avg}	18.4	22.67	19.4	1.5
$HV_{Predicted}$	95.2	93.6	94.7	133.1
$HV_{Experimental}$	95.8	95.7	104.5	134.6

TMAZ. In this region, under the influence of the tool shoulder, the layers close to the surface and subsurface were severely deformed and therefore contained smaller grains with large dislocation densities. The average grain size though volume weighted still could not sufficiently represent the microstructural state, therefore such a difference with the experimental result was seen. While in the Al alloy the prediction was over estimated and showed a linearly increasing profile, as only grain size variation in the weld was accounted. The hardness prediction model in its current state is insufficient and must be further modified to consider the additional softening/hardening produced by plastic deformation, dynamic recrystallization and dissolution or coarsening of precipitates for better accuracy.

3.5 Texture analysis

The stirring effect observed in the WZ and TMAZ causes a shear mode of deformation that varies in direction as a function of position across the weld. The tool rotation primarily pushes the material to flow in a direction tangential to the rotation. Along with the tangential deformation, material is also pushed forward parallel to the welding direction as the tool traverses through the material. The resultant of these two movements forces the material to orient itself at an angle of about 45° to the weld line. Fonda et al. [33] presented the ideal orientations associated with simple shear for FCC and BCC crystals. At each point, the shear direction (SD) is tangential to the tool's rotation and the shear orientations are aligned with effective tool surface. However, shear deformation is not the only factor influencing the texture. The downward flow of material under the action of tool shoulder, grain refinement, and resultant thermal gradients also play a crucial role. Due to offset, major part of the effective tool surface was in contact with the Al alloy and as such, strong shear texture must be evident from the EBSD results. However, because of dynamic recrystallization, new grains were nucleated, which then grew with random orientations, as a result no definite shear texture was observed in the WZ of the Al alloy.

On the other hand, DC04 alloy exhibited better thermal stability and severe plastic deformation in the WZ, which suggests the presence of shear texture. Abbasi et al. [5] reported such an observation of strong shear deformation with a texture intensity of 9.9 in the Fe phase. For the identification of shear texture, the individual local orientations must be rotated to align the shear direction (SD) and shear normal (SN) along the local shear coordinate system. The rotational matrix and the alignment system were defined according to the method presented by Abbasi et al. [5, 34]. Euler angles (ϕ_2, ϕ, ϕ_1) of individual grains obtained from EBSD measurement in the WZ were rotated about the A3 axis indicated in Fig. 4 to align the SD and its normal (SN) along the local shear co-ordinate system. A shear texture with a maximum intensity of 2 was observed only when the local orientations were rotated by 83° to the weld line. The pole figures for shear in the Fe alloy about the {111} and {101} planes are plotted in Fig. 12 [35]. This clearly indicates that due to the offset, the material flow in the Fe alloy was more along tangential direction rather than the SD. From such weak texture, it can be

Fig. 12 Pole figures about {101} and {111} planes presenting shear texture of the Fe alloy in the WZ
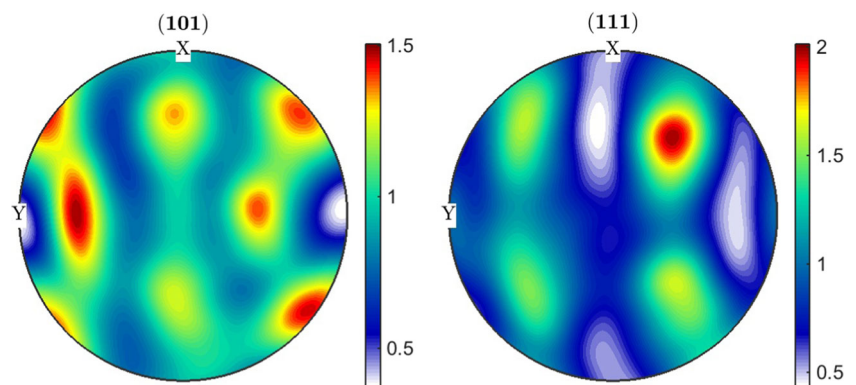
concluded that minimal shear strain was accumulated in the WZ.

4 Conclusion

– The microstructure of dissimilar friction stir welded AA6016-DC04 joints were characterized with conventional techniques. Grain size, micro-hardness, and texture were primarily examined. A mode of friction stir welding with minimal shear strain accumulation in steel and full dynamic recrystallization of aluminum was achieved. Micro-cracks, voids, or other defects were not observed. Fewer dispersed Fe chips were found embedded in the aluminum matrix. The EBSD phase map at the interface confirmed the absence of IMCs. The grain sizes in the form of CPD were plotted for various regions of the welded joint in both alloys and were compared with the distribution of their respective base materials.

– The CPD of grain size of Fe alloy showed fine grain sizes in the WZ and marginal grain growth in the TMAZ and HAZ. Due to the direct mechanical interaction with the tool only the upper layers of the alloy showed considerable grain refinement, while most of the inner layers remained unaffected. Very high hardness was observed in the WZ close to the upper surface in the Fe alloy indicating its susceptibility to bending failures. Limited diffuse heat and relatively high melting temperature of steel provided greater thermal stability. Marginal grain growth was however seen in the TMAZ and HAZ but no recrystallization of the microstructure was observed.

– In the Al alloy, the CPD of grain size showed fine grain microstructure in all of the weld regions. Complete dynamic recrystallization of microstructure due to plastic deformation and diffuse heat was evident from the KAM maps. The hardness of various weld regions was found to be similar to that of BM. Nucleation and growth of smaller grains compensated for the loss of strength in WZ and TMAZ due to dissolution or coarsening of strengthening precipitates during welding.

– A good correlation of the measured mean hardness to the predicted values was seen. In the Fe alloy, hardness was underestimated while in the Al alloy it was overestimated as the effects of dynamic recrystallization and dissolution or coarsening of precipitates were unaccounted for in the prediction.

References

1. Mallick P (2010) 8 - joining for lightweight vehicles. In: Mallick P (ed) Materials, design and manufacturing for lightweight vehicles, woodhead publishing series in composites science and engineering. Woodhead Publishing, pp 275–308. https://doi.org/10.1533/9781845697822.2.275. http://www.sciencedirect.com/science/article/pii/B9781845694630500080

2. Benedyk J (2010) 3 - aluminum alloys for lightweight automotive structures. In: Mallick P (ed) Materials, design and manufacturing for lightweight vehicles, woodhead publishing series in composites science and engineering. Woodhead Publishing, pp 79–113. https://doi.org/10.1533/9781845697822.1.79. http://www.sciencedirect.com/science/article/pii/B9781845694630500031

3. Schwabe J (2014) Entwicklung von dichtereduzierten Feinblechstählen für Automobilanwendungen. Ph.D. thesis, RWTH Aachen University. http://publications.rwth-aachen.de/record/444902

4. Springer H, Kostka A, dos Santos J, Raabe D (2011) Influence of intermetallic phases and Kirkendall - porosity on the mechanical properties of joints between steel and Aluminium alloys. Mater Sci Eng A 528(13–14):4630–4642. https://doi.org/10.1016/j.msea.2011.02.057. http://www.sciencedirect.com/science/article/pii/S0921509311002218

5. Abbasi M, Dehghani M, Guim H-U, Kim D-I (2016) Investigation of Fe-rich fragments in aluminum-steel friction stir welds via simultaneous Transmission Kikuchi Diffraction and ED. Acta Mater 117:262–269. https://doi.org/10.1016/j.actamat.2016.06.064. http://www.sciencedirect.com/science/article/pii/S1359645416304955

6. Shahverdi H, Ghomashchi M, Shabestari S, Hejazi J (2002) Microstructural analysis of interfacial reaction between molten aluminium and solid iron. J Mater Process Technol 124(3):345–352. https://doi.org/10.1016/S0924-0136(02)00225-X. http://www.sciencedirect.com/science/article/pii/S092401360200225X

7. Peyre P, Sierra G, Deschaux-Beaume F, Stuart D, Fras G (2007) Generation of aluminium and steel joints with laser-induced reactive wetting. Mater Sci Eng A 444(1–2):327–338. https://doi.org/10.1016/j.msea.2006.09.111. http://www.sciencedirect.com/science/article/pii/S0921509306021411

8. Thomas W, Nicholas E, Needham J, Murch M, Temple-Smith P, Dawes C (1995) Friction welding, us patent 5,460,317. http://www.google.com/patents/US5460317

9. Kusuda Y (2013) Honda develops robotized fsw technology to weld steel and aluminum and applied it to a mass production vehicle. Industrial Robot: An International Journal 40(3):208–212. https://doi.org/10.1108/01439911311309889

10. Amini A, Asadi P, Zolghadr P (2014) 15 - Friction stir welding applications in industry. In: Givi MKB, Asadi P (eds) Advances in friction-stir welding and processing, woodhead publishing series in welding and other joining technologies. Woodhead Publishing, pp 671–722. https://doi.org/10.1533/9780857094551.671. http://www.sciencedirect.com/science/article/pii/B978085709454450015X

11. Kumar K, Kailas SV (2008) The role of friction stir welding tool on material flow and weld formation. Mater Sci Eng A 485(1):367–374. https://doi.org/10.1016/j.msea.2007.08.013. http://www.sciencedirect.com/science/article/pii/S0921509307015419

12. Sahu PK, Pal S, Pal SK, Jain R (2016) Influence of plate position, tool offset and tool rotational speed on mechanical properties and microstructures of dissimilar Al/Cu friction stir welding joints. J Mater Process Technol 235:55–67. https://doi.org/10.1016/j.jmatprotec.2016.04.014. http://www.sciencedirect.com/science/article/pii/S0924013616301042

13. Galvão I, Loureiro A, Verdera D, Gesto D, Rodrigues DM (2012) Influence of tool offsetting on the structure and morphology of dissimilar aluminum to copper friction-stir welds. Metall Mater Trans A 43(13):5096–5105. https://doi.org/10.1007/s11661-012-1351-x

14. Pourali M, Abdollah-zadeh A, Saeid T, Kargar F (2017) Influence of welding parameters on intermetallic compounds formation in dissimilar steel/aluminum friction stir welds. J Alloys Compd 715:1–8. https://doi.org/10.1016/j.jallcom.2017.04.272. http://www.sciencedirect.com/science/article/pii/S0925838817314822

15. Elyasi M, Derazkola HA, Hosseinzadeh M (2016) Investigations of tool tilt angle on properties friction stir welding of a441 aisi to aa1100 aluminium. Proc Inst Mech Eng B J Eng Manuf 230(7):1234–1241. https://doi.org/10.1177/0954405416645986

16. Bambach M, Göttmann A, Mertin C, Mosecker L, Naumov A (2013) Properties of friction stir welded blanks made from dc04 mild steel and aluminum aa6016. In: WGP Congress 2013, vol 769 of Advanced Materials Research, Trans Tech Publications, pp 237–244. https://doi.org/10.4028/www.scientific.net/AMR.769.237

17. Tanaka T, Morishige T, Hirata T (2009) Comprehensive analysis of joint strength for dissimilar friction stir welds of mild steel to aluminum alloys. Scr Mater 61(7):756–759. https://doi.org/10.1016/j.scriptamat.2009.06.022. http://www.sciencedirect.com/science/article/pii/S1359646209004308

18. DebRoy T, Bhadeshia HKDH (2010) Friction stir welding of dissimilar alloys – a perspective. Sci Technol Weld Join 15(4):266–270. https://doi.org/10.1179/174329310X12726496072400

19. Lehto P, Romanoff J, Remes H, Sarikka T (2016) Characterisation of local grain size variation of welded structural steel. Welding in the World 60(4):673–688. https://doi.org/10.1007/s40194-016-0318-8

20. Gundersen HJG, Jensen EB (1985) Stereological estimation of the volume-weighted mean volume of arbitrary particles observed on random sections. J Microsc 138(2):127–142. https://doi.org/10.1111/j.1365-2818.1985.tb02607.x

21. Gundersen HJG, Jensen EB (1983) Particle sizes and their distributions estimated from line- and point-sampled intercepts, Including graphical unfolding. J Microsc 131(3):291–310. https://doi.org/10.1111/j.1365-2818.1983.tb04256.x

22. Dingley D (2004) Progressive steps in the development of electron backscatter diffraction and orientation imaging microscopy. J Microsc 213(3):214–224. https://doi.org/10.1111/j.0022-2720.2004.01321.x

23. Shimokawa T, Yamashita T, Niiyama T, Tsuji N (2016) Grain subdivision mechanism related to partial disclinations in severe plastic deformation: a molecular dynamics study. Mater Trans 57(9):1392–1398. https://doi.org/10.2320/matertrans.MH201518

24. Jaafar A, Rahmat A, Hussain Z, Zainol I (2011) Effect of Mg, Si and Cu content on the microstructure of dilute 6000 series aluminum alloys. J Alloys Compd 509(35):8632–8640. https://doi.org/10.1016/j.jallcom.2011.05.061. http://www.sciencedirect.com/science/article/pii/S0925838811011571

25. Hakamada M, Nakamoto Y, Matsumoto H, Iwasaki H, Chen Y, Kusuda H, Mabuchi M (2007) Relationship between hardness and grain size in electro-deposited copper films. Mater Sci Eng A 457(1-2):120–126. https://doi.org/10.1016/j.msea.2006.12.101

26. Taha AS, Hammad FH (1990) Application of the hall-petch relation to microhardness measurements on al, cu, al-md 105, and al-cu alloys. Phys Status Solidi (a) 119 (2):455–462. https://doi.org/10.1002/pssa.2211190207

27. Lehto P, Remes H, Saukkonen T, Hänninen H, Romanoff J (2014) Influence of grain size distribution on the Hall–Petch relationship of welded structural steel. Mater Sci Eng A 592:28–39. https://doi.org/10.1016/j.msea.2013.10.094. http://www.sciencedirect.com/science/article/pii/S0921509313012094

28. Baudoin P, Magnier V, Bartali AE, Witz J-F, Dufrenoy P, Demilly F, Charkaluk E (2016) Numerical investigation of fatigue strength of grain size gradient materials under heterogeneous stress states in a notched specimen. Int J Fatigue 87:132–142. https://doi.org/10.1016/j.ijfatigue.2016.01.022. http://www.sciencedirect.com/science/article/pii/S0142112316000323

29. Khadyko M, Marioara C, Ringdalen I, Dumoulin S, Hopperstad O (2016) Deformation and strain localization in polycrystals with plastically heterogeneous grains. Int J Plast 86:128–150. https://doi.org/10.1016/j.ijplas.2016.08.005. http://www.sciencedirect.com/science/article/pii/S0749641916301401

30. Dunstan D, Bushby A (2014) Grain size dependence of the strength of metals: The Hall-Petch effect does not scale as the inverse square root of grain size. Int J Plast 53:56–65. https://doi.org/10.1016/j.ijplas.2013.07.004. http://www.sciencedirect.com/science/article/pii/S074964191300140X

31. Nicaise N, Berbenni S, Wagner F, Berveiller M, Lemoine X (2011) Coupled effects of grain size distributions and crystallographic textures on the plastic behaviour of IF steels. Int J Plast 27(2):232–249. https://doi.org/10.1016/j.ijplas.2010.05.001. http://www.sciencedirect.com/science/article/pii/S0749641910000665

32. Berbenni S, Favier V, Berveiller M (2007) Impact of the grain size distribution on the yield stress of heterogeneous materials. Int J Plast 23(1):114–142. https://doi.org/10.1016/j.ijplas.2006.03.004. http://www.sciencedirect.com/science/article/pii/S074964190600043X

33. Fonda RW, Knipling KE (2011) Texture development in friction stir welds. Sci Technol Weld Join 16(4):288–294. https://doi.org/10.1179/1362171811Y.0000000010

34. Abbasi M, Nelson TW, Sorensen CD (2012) Transformation and deformation texture study in friction stir processed API X80 pipeline steel. Metall and Mater Trans A 43(13):4940–4946. https://doi.org/10.1007/s11661-012-1356-5

35. Bachmann F, Hielscher R, Schaeben H (2010) Texture analysis with MTEX-free and open source software toolbox. Solid State Phenom 160:63–68. https://doi.org/10.4028/www.scientific.net/SSP.160.63

3.3 Publication III

Finite Element Simulation of Residual Stress Induced by High Energy Beam Welding in Dual Phase Steel
K. Komerla, S. Gach, F. Akyel, T. Vossel, U. Reisgen, W. Bleck (2020), Lasers in Manufacturing and Materials Processing. https://doi.org/10.1007/s40516-020-00112-4

Highlights

- A Novel volumetric heat source model involving the superposition of conical and spherical thermal fluxes, that can accurately predict steep temperature gradients occurring during high energy beam welding was developed

- A metallurgical framework, wherein the evolution of different phase fractions, their corresponding thermal and transformation strains was introduced. With the help of this framework, residual stress during the electron beam welding of dual phase steels was predicted

- The massive misfit strains that are generated during the cooling cycle of welding was found to have significant influence on the magnitude of residual stress. High tensile stresses along the longitudinal direction in the fusion zone and moderate compressive stress in the transverse direction were observed

Finite Element Simulation of Residual Stress Induced by High Energy Beam Welding in Dual Phase Steel

Krishna Komerla[1] · Stefan Gach[2] · Fatma Akyel[2] · Thomas Vossel[3] ·
Uwe Reisgen[2] · Wolfgang Bleck[4]

Abstract

In this study, the residual stresses that arise during the high energy beam welding of dual phase steels were investigated using a sequentially coupled 3D finite element model. To accurately predict the sharp temperature gradients across the different weld zones, a moving volumetric heat source model, combining a spherical and a conical thermal flux distribution was developed. The temperature profiles computed with this heat source model were found to be in excellent agreement with the measured temperatures. Additionally, the simulated weld geometry was compared to the optical micrographs of the weld cross section to validate the heat source model parameters. The time-temperature history recorded at each node of the FE mesh served as input for the metallurgical and mechanical analyses, where the kinetics of phase transformations, the volumetric dilatations and thereby, the residual stresses in the weld joint were calculated. A metallurgical framework that includes the effect of volumetric strains occurring due to the phase transformations on the residual stresses was presented. The results show that the solid-solid phase transition occurring during cooling in a weld procedure can have a large influence on the magnitude of the residual stress. Furthermore, a comparison of the predicted welding residual stresses with the experimental drill-hole test results in both the weld seam and the base material was also reported.

Introduction

In the manufacturing industry, fusion welding is extensively used in the fabrication of structural parts and assemblies. It involves the application of a concentrated heat

---

✉ Krishna Komerla
    kkomerla@iehk.rwth-aachen.de

Extended author information available on the last page of the article.

source in order to locally melt and join two work pieces together. The rapid heating and subsequent cooling cycles introduce steep temperature gradients, that significantly alter the microstructure of the welded regions. Metallurgical phenomena such as localized melting, material flow, solidification and solid state phase transformations that occur during welding are responsible for the generation of complex thermal strains, residual stresses and distortion in the weldaments, adversely affecting their structural integrity and load bearing capacity. Tensile residual stresses are known to increase the susceptibility of the weld to fatigue damage, stress assisted corrosion and fracture [1–3]. Therefore, an accurate quantification of the welding residual stresses is necessary, especially for safety critical components.

Typically, material in the fusion zone (FZ) and in the adjacent heat affected zone (HAZ) experiences different thermal conditions and as a result exhibits contrasting microstructures and mechanical properties. The FZ corresponds to temperatures above liquidus temperature and undergoes melting during the heating, and solidification during the subsequent cooling cycle. While the HAZ corresponds to temperatures below the solidus temperature and exhibits austenization in regions present close to the fusion line and away from the fusion line, grain coarsening and softening of microstructure could occur. In both the weld zones, the decomposition of austenite during the cooling step plays a critical role in controlling the welding residual stresses and distortion. Factors like the chemical composition, peak temperature, grainsize, the rate of heating and cooling etc. define the onset of various solid state phase transformations. In general, the metallurgical transformation in welding are categorized as reconstructive and displacive transformations [4, 5]. In reconstructive processes, due to the diffusion of all the elements, strains are generated from the change in density while, in the displacive processes like the formation of martensite, the composition of the parent phase remains identical to the product phase but, a change in the crystal is achieved by the deformation of its structure leading to an increase in the volume. The magnitude of volumetric expansion depends on the fraction of various phases formed.

Several researchers have reported on the evolution and spatial distribution of various phases and their impact on the generation of residual stresses during and after the welding process. Deng and Murakawa [6] developed a three dimensional finite element (FE) model to simulate the temperature fields and the welding residual stresses in the multi pass, girth welding of austenitic stainless steel pipe sections. It was reported that, close to the weld line, tensile residual stresses were produced on the inner surface and compressive residual stresses on the outer surface, while away from the weld center, the direction of residual stresses was found to be reversed. Deng [7] also presented a FE model considering the martensite phase transformation in low carbon steels and showed that, the phase transformation has a significant impact on the residual stress and distortion in the weldament due to the large volumetric dilatation of the martensite phase. Kumar et al. [8] quantified the welding residual stress with neutron diffraction technique and reported on the influence of strains associated with the martensite transformation during laser welding. Hamelin et al. [9] proposed a model to predict the solid state phase transformation kinetics in the tungsten inert gas welding of ferritic steels, where phase related hardness profiles were predicted and validated with micro hardness measurements. Ni et al. [10]

implemented a phase transformation kinetics based framework in an FE software to predict the microstructure development during welding [11–13]. The phase transformation kinetics in their framework was based on gibbs free energy description of the materials and the decomposition of austenite into ferrite, bainite and martensite phases were thoroughly accounted. Wang et al. [14] studied the evolution of residual stresses in high strength ferritic steels by accounting for the plastic deformation arising from the transformation strains during welding. An improvement in the prediction of welding residual stresses was also reported. However a comprehensive study considering the high heating and cooling rates on the metallurgy of the dual phase steel during high energy beam welding is yet to be reported.

In this study, a sequentially coupled FE model was developed to predict thermal, metallurgical and mechanical characteristics of dual phase steels during electron beam welding. To accurately calculate the temperature fields during welding, a volumetric heat source model was developed and validated with experimental results. Though the model is applicable to any fusion welding process, within the scope of this study, the presented model and its parameters were tailored to suit the electron beam welding (EBW) process. A phase transformation model comprising the austenization, melting, solidification and martensite phase transformation occurring during the rapid heating and cooling processes was used to predict the spatial distribution of various phases during the welding process. Furthermore, the phase dependent volumetric dilatations accounting for the thermal and transformation strains during welding were calculated to predict the welding residual stresses in the weld joint. Finally the predicted temperature distribution and residual stresses were validated with experimental results. The variation of grain size across the weld joint also plays a crucial role in controlling the mechanical properties of the different weld zones. In this current study the impact of grain size on the phase transformations and the residual stress were not considered. However, the authors plan to extend the current framework by coupling thermally activated grain growth with existing phase transformation models in the next study.

Materials and Experimental Methods

Materials

In this study, a 1 mm thick cold rolled dual phase steel (DP1000) was considered. In the as obtained state, its microstructure consisted approximately 40% martensite and 60% ferrite phase fractions. The composition of the steel is presented in Table 1. It is an advanced high strength steel that derives strength from its complex microstructure

Table 1 Chemical composition of dual phase steel in weight %

Element	C	Si	Mn	P	S	Cr	Ni	Cu	Al	Ti	N	C_{eq}
DP1000	0.09	0.315	2.50	0.0145	0.002	0.685	0.022	0.101	0.032	0.076	0.0141	0.15

Fig. 1 Schematic showing weld blanks, thermocouple positions and welding direction
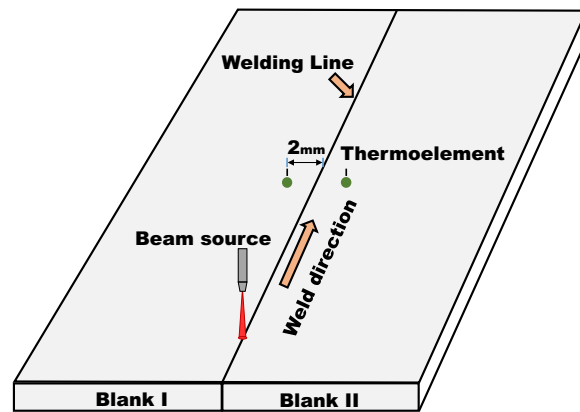
consisting of ferrite and martensite phases. It offers impressive mechanical properties like the absence of yield point elongation, high work hardening and high ultimate tensile strength [15–17]. These unique characteristics of DP steels are vastly sought after in the automotive industry, to reduce weight and improve passenger safety [18, 19].

Electron Beam Welding

Several prepared steel blanks ($150 \times 100 \times 1$ mm) were butt welded (in the PA position as per the DIN EN ISO 6497 norm) using a universal chamber electron beam welding machine of type K7 manufactured by pro-beam. Autogeneous welding was carried out, the beam was focussed on the surface of work piece to produce welds in a single pass. Preheating, welding consumables, additional fixtures and weld tacks were not utilized during welding. However, as the sheet material was cut using a shearing machine, the edges of the work pieces were grinded to remove any irregularities and ensure a correct fit between them. A typical weld setup is presented in the Fig. 1 and the applied welding parameters are listed in the Table 2. Temperature was recorded with the help of wire shaped thermoelements that were spot welded at a distance of 2 mm from the weld center as shown in Fig. 1 Welding was carried out in vacuum and no external cooling was employed in the chamber.

Dilatometer Analysis

Heat treatments were carried out using a Baehr DIL-805A/D dilatometer, with the aim of studying the phase transformation kinetics during continuous heating and cooling processes. Specimens of dimension $2 \times 7 \times 1$ mm obtained from the base material were subjected to heating rates of 1 - 100 °K/s and varying cooling rates ranging from 10 - 500 K/s. These cooling rates were achieved by flooding the test

Table 2 EBW parameters used in welding dual phase steel blanks

Chamber pressure (hPa)	Accelerating voltage (kV)	Beam current (mA)	Welding speed (mm/s)
10^{-4}	120	6	40

chamber with various gases like helium, argon etc. The relative change in length of the specimen was acquired with the help of a laser measurement system, that records the non-linear expansion or contraction of samples during solid state phase transformations.

Hole Drilling Method

Hole drilling is a destructive testing method applied in order to analyze residual stresses in the weld joints. It involves drilling a blind hole in the specimen and measuring strain in the vicinity of the hole [20]. Figure 2b presents the position of different blind holes drilled on the test specimens. Electronic speckle pattern interferometry was employed to track distortion inside the hole, that arose from the relaxation of internal stresses after material was removed by drilling. The specimen surface was illuminated with coherent laser light and analyzed by a camera system. The surface roughness naturally projects a speckled pattern, as light reflected from a rough surface interferes either constructively or destructively creating a speckled pattern of bright and dark areas in the image. A change in this speckle pattern due to stress relaxation creates a shift in the image that enables the measurement of strain. The stress is measured by correlating the strains (ϵ), the elastic modulus (E) and the poisson's coefficient (v) as below

$$\sigma_{ij} = \frac{E}{(1+v)}\epsilon_{ij} - \frac{vE}{(1+v)(1-2v)}\delta_{ij}\epsilon_{kk} \tag{1}$$

$$\epsilon_{ij} = \begin{bmatrix} \epsilon_{11} & \epsilon_{12} & \epsilon_{13} \\ \epsilon_{21} & \epsilon_{22} & \epsilon_{23} \\ \epsilon_{31} & \epsilon_{32} & \epsilon_{33} \end{bmatrix}$$

The elastic modulus and the Poisson's coefficient for steel are taken as 210 GPa and 0.3 respectively

Finite-Element Analysis

The evolution of temperature and residual stresses during EBW were investigated by means of a three dimensional finite element (FE) model. The moving heat source and the metallurgical models were integrated into the commercial FE software *Abaqus* [21] with the help of user subroutines. As the internal heat generation arising from the plastic dissipation and the mechanical work done, is insignificant in comparison to the thermal flux produced during EBW, the thermo-mechanical behavior of the welded structure was simulated using a sequentially coupled formulation. The transient temperature distribution was solved independently from the mechanical stress problem. It is a challenging task to precisely map the temperature distribution during EBW, especially at points present in close proximity to the keyhole. Therefore, a moving volumetric heat source model that is representative of the electron beam was developed. The mathematical description of the heat source encompasses a distributed heat flux in order to obtain the temperature distribution. *Dflux* routine was

utilized in defining the thermal flux distribution over a section of the FE model. Furthermore, the time-temperature history and the evolution of various phase fractions recorded at each node in the FE mesh (see Fig. 2) during the uncoupled heat transfer analysis were employed as thermal load and initial material state in the subsequent residual stress analysis. The thermal and transformation strains calculated in the *uexpan* subroutine were then returned to the solver as thermal expansion coefficients during the stress analysis.

Heat Source Model

Goldak et. al. [22] introduced a volumetric heat source model capable of describing the thermal history of shallow and deep penetration welding. The thermal flux distribution in the model was divided into leading and trailing quadrants to accommodate the difference in temperature gradients observed between the front and rear of the heat source. The double ellipsoidal heat flux distribution described as a function of spatial coordinates *(x, y, z, t)* is given by

$$Q_V = \frac{6\sqrt{3} f_i Q}{abc_i \pi \sqrt{\pi}} \exp\left(\frac{-3x^2}{a^2} + \frac{-3y^2}{b^2} + \frac{-3[z - v(\Delta t)]^2}{c_i^2} \right) \tag{2}$$

where a, b, c_i are the width, depth and length of the front/rear quadrant, f_i is the absorption coefficient, v is the weld speed and Δt is the time interval. However, for deep and narrow groove or key hole welding methods, the sharp gradient of temperature generally observed at the root of weld between the FZ and HAZ could not be reproduced, as the keyhole effect was not included in the description. In high energy beam welding processes, a narrow and focused beam is incident on the surface of work piece causing rapid melting and partial vaporization. The intense recoil pressure exerted by the vapour flux leads to the formation of a deep cavity or keyhole. To repli-
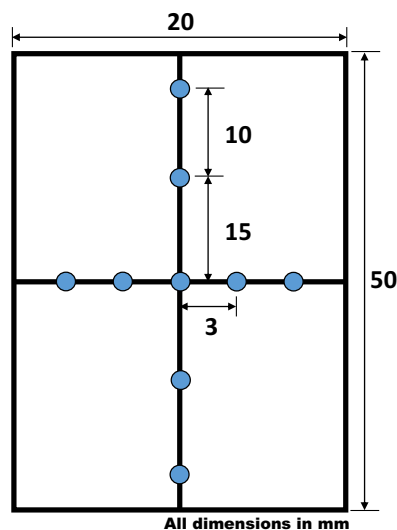
(a) Marked positions for hole drilling tests to measure longitudinal residual stress
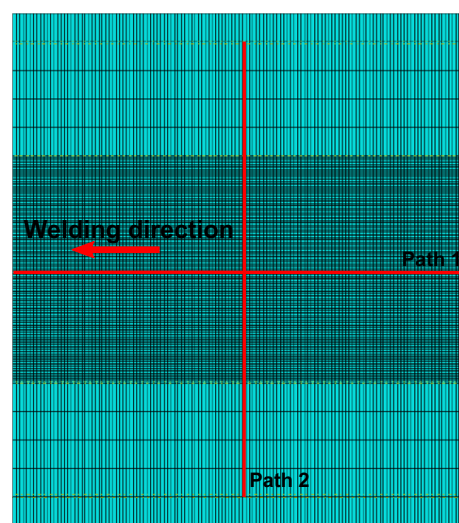
(b) Top view of finite element mesh depicting fine mesh in welded zone along with paths for residual stress measurement

Fig. 2 Depiction of positions for the experimental measurement of longitudinal residual stress on the welded sheet (**a**); The two paths about which stress was obtained from the finite element mesh (**b**)

cate such a behavior, the heat source model must include a larger power distribution near the surface and a flux decay along the penetration depth. In this study a modified Goldaks heat source model capable of describing the varying heat input inside a keyhole was proposed. The total power density of the electron beam is divided into spherical and conical parts as shown in the Fig. 3a.

$$Q_{EB} = Q_{Spherical} + Q_{Conical} \tag{3}$$

The flux density distribution within the spherical domain can be described by a Gaussian function as presented in Eq. 2.

$$Q_{Spherical} = (1 - \psi) \frac{6\sqrt{3}Q}{R_g^3 \pi \sqrt{\pi}} \exp\left[-3\left(\frac{x^2}{R_g^2} + \frac{y^2}{R_g^2} + \frac{[z - v(\Delta t)]^2}{R_g^2}\right)\right] \tag{4}$$

where Q is the product of acceleration voltage (U), beam current (I) and energy absorption coefficient (η), while R_g is the radius of sphere. The high energy electrons impinging the work piece penetrate only the surface and rapidly transfer their kinetic energy to the surrounding material in the form of heat. This heat causes the material to melt and evaporate, leading to the formation of a gas channel at the center of melt. However, the penetration depth of the electrons is less than an order of magnitude. As such, the power density of the beam is larger at the surface and decreases with increasing depth of the keyhole. Therefore, the flux distribution in the conical domain was built such that the volume of thermal flux decreases linearly with the increasing penetration depth. The Fig. 3b presents the distribution of combined heat flux as a function of position, where the flux is maximum at the center of grid and decays to 0 with increasing distance away from the center.

$$Q_{Conical} = \frac{3\psi Q}{\pi H R_0^2} \exp\left[-3\left(\frac{x^2}{R_0^2} + \frac{(z - v\Delta t)^2}{R_0^2}\right)\right] \overbrace{\left[1 + 0.01\left(\frac{H - y}{H}\right)\right]}^{\textbf{S}} \text{step}(H, y) \tag{5}$$

$$\text{step}(H, y) = \begin{cases} 0 \text{ if } H - y < 0.0 \\ 1 \text{ if } H - y \geq 0.0 \end{cases}$$

(a) Combined spherical & Conical heat source model

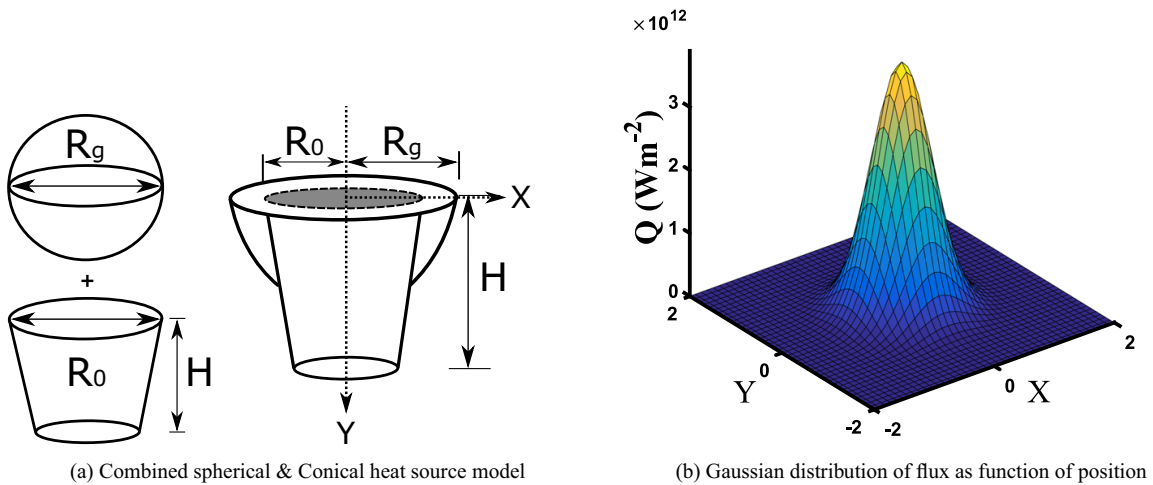(b) Gaussian distribution of flux as function of position

Fig. 3 Illustration of the volumetric heat source model along with the Gaussian distribution of its thermal flux

In the Eq. 5, H is the thickness of the workpiece and R_0 is the base radius of the cone. The term 'S' provides the negative slope where, with increasing y the available flux decreases linearly. Thereby the bottom portion of the cone contains lower flux density in comparison to the surface. Additionally, to strike a balance between the spherical and conical domains while accounting for the overlap of both fluxes, the term ψ was introduced in the equations such that the total fraction of thermal flux remains 1.0.

Metallurgical Model

Phase transformations in steels are driven by the difference in Gibbs free energy between the parent and product phases. This free energy for transformation can be defined as function of composition, stress/strain state and temperature [23]. Majority of phase transformations occurring in steels are thermally activated and are accompanied by the diffusional movement of atoms, also known as reconstructive/diffusional transformations. Under rapid cooling conditions however, such diffusional movement of atoms can be hindered and transformation can proceed in a displacive manner where the coordinated movement of atoms in the lattice produces a product phase with identical composition as the parent phase. These diffusional or displacive phase transformations are always accompanied by volumetric dilatations that arise from heterogeneities in the distribution of alloying elements and create local stress fields in the welded structures. High peak temperatures produce dendrites in the FZ, coarse to fine grained microstructures in the HAZ.

Austenization

Austenization is a non-isothermal process that occurs during the welding thermal cycles. When DP steels are heated above their Ac_1 temperature, face centered cubic structured austenite nucleates in the martensite phase, preferentially at the lath boundaries and continues to grow until the Ac_3 temperature is reached. Assuming that the transformation occurs by the nucleation and growth of a new phase, the kinetics of transformation and the evolution of phase fractions can be postulated using the Johnson-Mehl-Avrami-Kolmogrov (JMAK) approach [24].

$$V_\gamma = 1 - \exp\left[-kt^n\right] \tag{6}$$

where V_γ is the austenite fraction, k and n are the material parameters and t is the time. Caballero et al. [25] introduced a heating rate dependent austenization model for two phase microstructures that is also based on the nucleation and growth of a new phase. Though the model was developed for ferrite and pearlite steels, it can be adopted to DP steels. The nucleation and growth of austenite in martensite phase can be described as

$$V_\gamma^m = V_{m_0}\left[1 - \exp\left(\frac{4\pi}{3\dot{T}^4}\dot{N}G^3\Delta T^3\right)\right] \tag{7}$$

where V_{m_0} is the initial martensite fraction and $\dot{T}$ is the heating rate obtained during welding. The nucleation rate $\dot{N}$ and growth rate G were expressed as a function of their respective activation energies (Q_N, Q_G) as below

$$\dot{N} = f_N \exp\left(\frac{-Q_N}{k \Delta T}\right) \quad \& \quad G = f_G \exp\left(\frac{-Q_G}{k \Delta T}\right) \tag{8}$$

The fitting parameters f_N, f_G along with the activation energies for dual phase steels were taken from the study published by Thiesen et al. [26]. The kinetics of ferrite to austenite transformation after the conversion of martensite is expressed as

$$V_\gamma^\alpha = \begin{cases} V_{\alpha_0}\left[1 - \frac{5.6\dot{T}}{6\times10^{-12}V_{\alpha_0}(T-T_C)^{5.6}+5.6\dot{T}}\right] & \text{for} \quad T_C < T < T_D \\[3mm] V_{\alpha_0} - \frac{(V_{\alpha_0}-V_D^\alpha)\dot{T}^2}{\dot{T}^2+1.2\times10^{-3}(V_{\alpha_0}-V_D^\alpha)[(T-T_C)^2-(T_D-T_C)^2]} & \text{for} \quad T \geq T_D \end{cases}$$

where V_{α_0} is the initial ferrite fraction, T is the current temperature and T_C & T_D are the transformation temperatures determined experimentally by means of dilatometric analysis as shown in Fig. 4a.

Melting & Solidification

In a typical phase diagram, above the solidus line and below the liquidus line, there exists a two phase region where at different temperatures varying fractions of solid and liquid phases can be seen (see Fig. 4b). In the welding process, the cooling rates are too rapid to allow substantial diffusion of alloying elements in the solid phase therefore, a local equilibrium can be assumed at the solid-liquid interface. Thus the
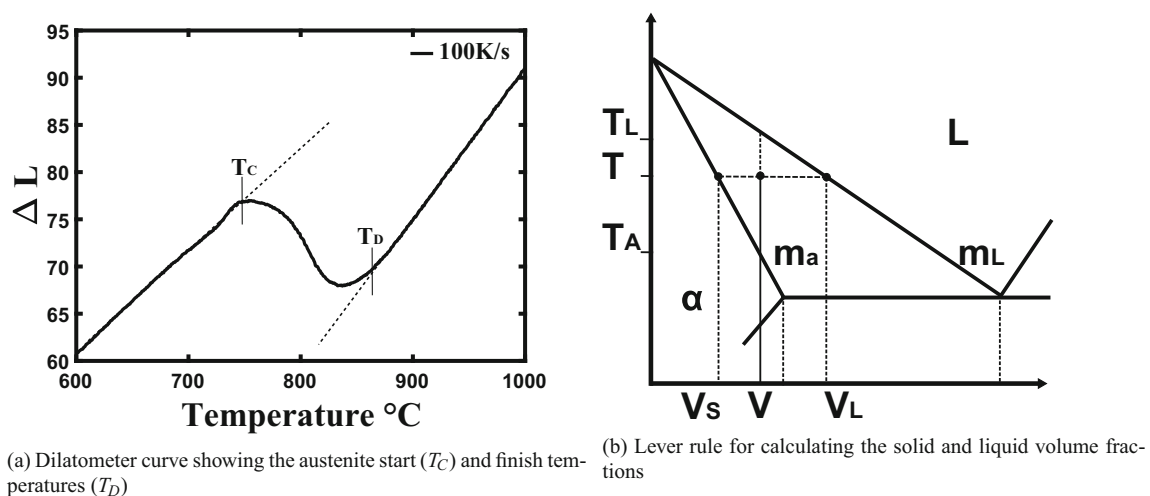

(a) Dilatometer curve showing the austenite start (T_C) and finish temperatures (T_D)

(b) Lever rule for calculating the solid and liquid volume fractions

Fig. 4 The dilatometer curve showing the austenizaiton of dual phase steel at a heating rate of 100K/s (**a**); The lever rule to calculate the solid and liquid fractions at any temperature in the two phase region (**b**)

well known lever rule was employed to predict the volume fractions of liquid and austenite at temperature (T) during melting and solidification as shown below

$$V_L(T) = \frac{(T - T_A)/m_a}{(T_A - T)/m_a + (T_L - T)/m_l} \qquad (9)$$

$$V_S(T) = \frac{(T_L - T)/m_l}{(T_A - T)/m_a + (T_L - T)/m_l} \qquad (10)$$

where V_l, V_s are the liquid and solid volume fractions, T_l, T_a are the liquidus and solidus temperatures, m_l, m_a are the slopes of the liquidus and solidus lines obtained from the Fe-C phase diagram.

The melting function however, does not contribute towards the prediction of residual stresses. In molten state, the weld does not contain any considerable stresses. Nevertheless, it aid in estimating the dimensions of melt pool and also in establishing a verification function where, the sum of all the phase fractions at any instance must equal 1.0. As the different equations in the metallurgical framework are not explicitly coupled, it is necessary to perform such checks at regular intervals during the simulation.
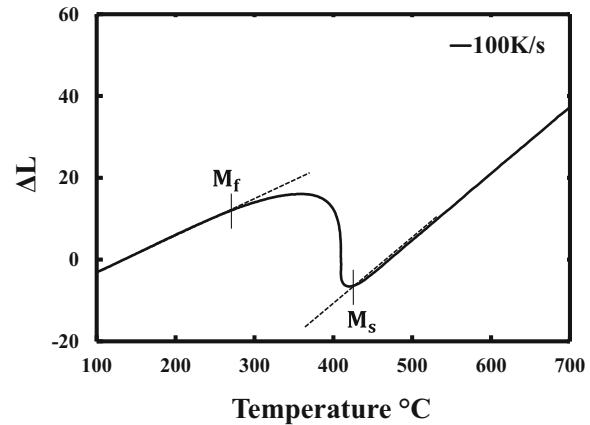
Martensite Transformation

During the rapid cooling process the face centered cubic austenite phase does not have sufficient time to rearrange itself into body centered cubic lattice, therefore in an attempt to lower its free energy state, the austenite lattice shears into a body centered tetragonal structure trapping the interstitial carbon atoms in the process. This austenite to martensite transformation is athermal in nature and is accompanied by large volumetric dilatation. This is one of the prime reasons for the generation of residual stresses in the weld joint. The level of residuals can be directly correlated to the volume fraction of martensite formed in the weld. The well known Koistinen–Marburger relationship [27] was used to describe the martensite transformation.

$$V_m = V_\gamma(1 - \exp[-b(M_s - T)]) \qquad (11)$$

where V_m is the martensite volume fraction, V_γ is the existing austenite fraction, T is the temperature, M_s and M_f are the martensite start and finish temperatures. The M_s and M_f were obtained from the dilatometer test (see Fig. 5) where samples were heated to a temperature that is 50 °C above the AC_3 and then quenched in the test chamber with Argon gas. To obtain the start and finish temperatures of just the martensite phase such a test was carried out. However, martensite in dual phase steel is obtained after an inter critical annealing treatment and it exhibits different carbon solubility. As a result the M_s and M_f temperatures might vary in comparison to the experimental results.

Fig. 5 Dilatometer curve
showing the martensite start
(M_s) and finish (M_f)
temperature during quenching in
argon gas

Thermal-Metallurgical-Mechanical Coupling

The estimation of welding induced residual stress using finite element methods has been gaining attention because of its ability to consider realistic boundary conditions, temperature dependent material properties and complex weld joint geometries. An adequate representation of the heat source model and accurate estimation of the temperature fields is paramount to predicting the kinetics of phase transformations and the evolution of thermo-mechanical strains during the heating and cooling cycles of the welding process. Assuming an isotropic simulation domain with temperature dependent heat transfer, the heat flux introduced by the moving volumetric heat source was resolved using Fourier's law [21]

$$\frac{\delta}{\delta x}\left(k\frac{\delta T}{\delta x}\right) + \frac{\delta}{\delta y}\left(k\frac{\delta T}{\delta y}\right) + \frac{\delta}{\delta z}\left(k\frac{\delta T}{\delta z}\right) + Q = \rho c \frac{\delta T}{\delta t} \qquad (12)$$

where Q is heat flux per unit volume, k is conductivity, T is temperature, ρ is density and c is specific heat capacity of the material. The thermo-physical data of dual phase steels is listed in the Appendix. The time-temperature data obtained during heat transfer simulation was utilized to study the influence of peak temperature, heating and cooling rates on the various phase transformations taking place during welding. The metallurgical models presented in this paper considered the above mentioned factors in describing the evolution of various phases. The total volumetric dilatations arising from the thermal and transformation strains of each phase were captured in the form of a dilatation coefficient as follows

$$\beta = V_\alpha \beta_\alpha + V_{\alpha'} \beta_{\alpha'} + V_\gamma \beta_\gamma \qquad (13)$$

The term β represents the combined thermal and transformation strains arising from all the existing phases. V_α, $V_{\alpha'}$ and V_γ are the volume fractions of ferrite, martensite and austenite phases calculated from the metallurgical models as discussed previously. Pan et al. [28] reported on the thermal stress and volume change of carbon steels. The dilatation during phase transformations was computed according to their study. It was reported that the austenite dilatation ($\beta_\gamma = 23 \times 10^{-6}$) remains constant with temperature, while the volumetric dilatation of martensite was found to increase
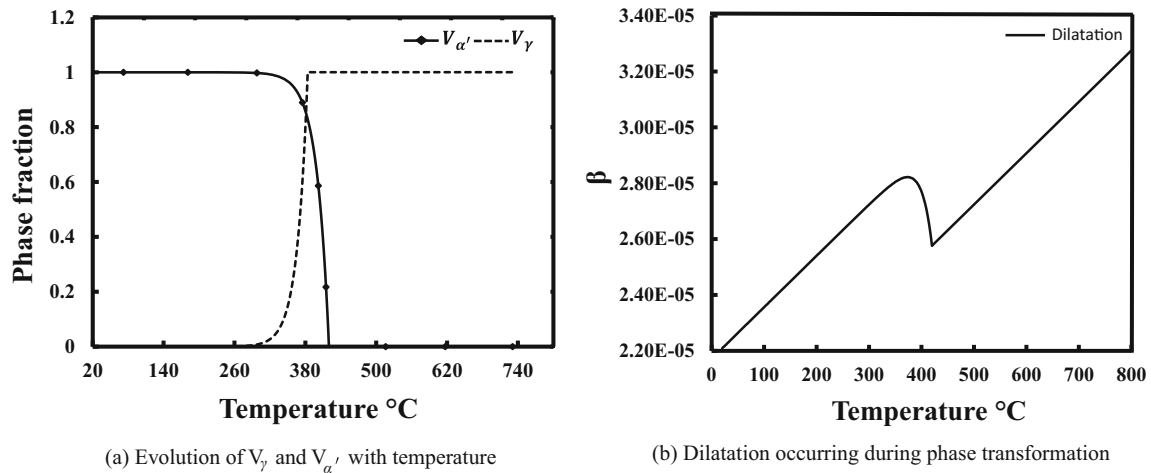
(a) Evolution of V_γ and $V_{\alpha'}$ with temperature

(b) Dilatation occurring during phase transformation

Fig. 6 Computed evolution of austenite and martensite phase fractions during cooling (**a**); Corresponding dilatation computed during austenite to martensite phase transformation (**b**)

with increasing temperature and decreasing carbon content. For low carbon steels an average value of $\beta_{\alpha'} = 15 \times 10^{-6}$ for martensite and $\beta_\alpha = 12 \times 10^{-6}$ for ferrite phases were suggested. As stated earlier the total volumetric strain depends significantly on the temperature and the chemical composition of an alloy. The thermal strains are assumed to vary linearly with temperature change, however the transformation strains are non-linear in nature and tend to vary as the phase change progresses. In order to demonstrate such behaviour, the expansion coefficients calculated at a single point during the cooling cycle are presented below. As seen in Fig. 6a and b, the overall dilatation decreases continuously until the M_s temperature is reached. V_γ decreases drastically below the M_s, while the $V_{\alpha'}$ increases rapidly. As the austenite to martensite transition is a non diffusive process, their respective dilatation coefficients are constant. Below the M_f, the dilatation resumes its continuous descent until the ambient temperature.

Furthermore, the formation of martensite, is accompanied by plastic accommodation of laths within the martensite islands. This deformation however is insignificant in comparison to the strains induced in the BM adjacent to the weld regions. Therefore, it can be assumed that the deformation of martensite in the FZ and HAZ is only elastic in nature while, in rest of the BM, especially the ferrite phase undergoes significant plastic deformation. Authors have investigated the temperature dependent elasto-plastic properties of DP steels with the aid of hot tensile tests in their previous study [29]. The stress-strain data obtained from those experiments were utilized in the current study to estimate the residual stresses in the weld joint.

Results and Discussion

Temperature Distribution

An uncoupled transient heat transfer analysis was carried out by integrating the proposed volumetric heat source model into an FE solver to study the temperature

Table 3 Heat source model parameters fitted by trial and error method

R_g (m)	R_0 (m)	ψ	U (V)	I (A)	η	v (m/s)	H (m)
800E-6	650E-6	0.87	120E3	6E-3	0.62	40E-3	1.0E-3

distribution in the weld joint. In order to reduce the computational effort, symmetry of the domain was taken into account and only one half of the weld joint was simulated.

As the electron beam welding process takes place in vacuum, only radiation boundary conditions were imposed. The 3D simulation domain was discretized into hexahedral elements (DCC3D8T) with temperature degree of freedom to form the finite element mesh. The process of single pass welding was simulated in two steps, a heating step where the equivalent heat source traverses along the welding direction for 2 seconds and a cooling step lasting 100 seconds allowing for the removal of heat.

To validate the heat source model, the temperature evolution on the surface of the weld blank was measured using K-type wire thermocouples that were spot welded at a distance of 2 mm, away from the weld line. As the welded sheets were only 1 mm thick, the heat conduction was homogeneous in the work piece. However, when welding thicker sheet materials additional measurement points are needed in order to observe the variation of temperature in the weld pieces along different directions. Additionally, to validate the model one measurement point was sufficient as the mathematical flux description of the heat source model yields a constant thermal flux. As such, similar temperature profiles would be observed at different points in the FE mesh. The fitted model parameters are presented in the Table 3. A comparison of the thermocouple data and the predicted thermal response is presented in the Fig. 7b.
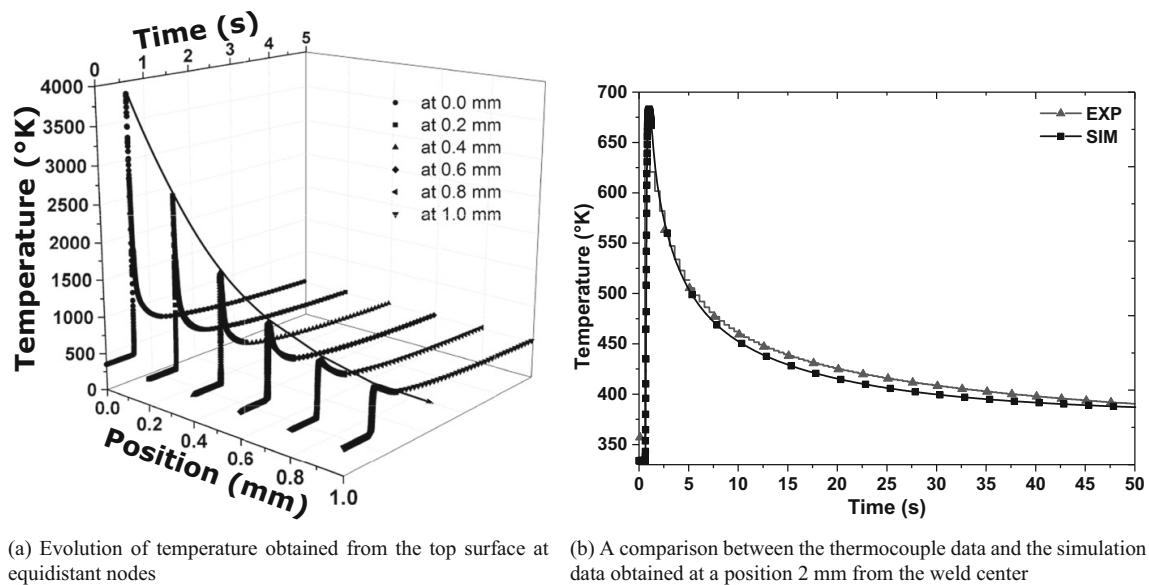

(a) Evolution of temperature obtained from the top surface at equidistant nodes

(b) A comparison between the thermocouple data and the simulation data obtained at a position 2 mm from the weld center

Fig. 7 The temperature evolution obtained from the thermal analysis depicting a steep drop in temperature from the weld center towards the BM along the transverse direction (**a**); A comparison of the experimental and simulated temperature data to validate the heat source model (**b**)
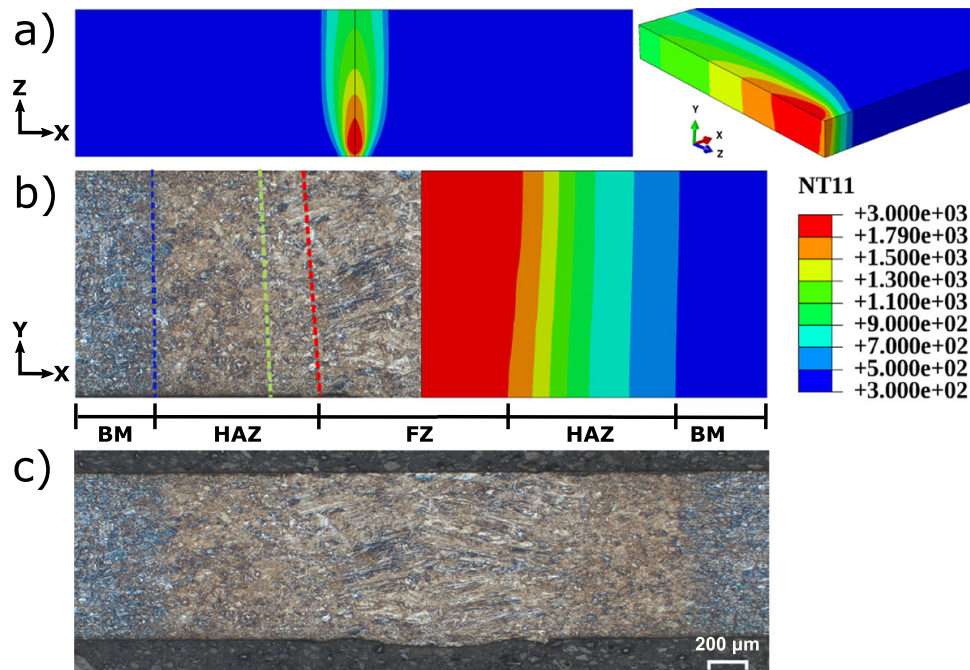
Fig. 8 Typical tear drop geometry of the melt pool observed during high speed welding (**a**); Temperature distribution in the DP1000 weld joint along with the depiction of different weld zones marked based on their peak temperature (**b**); Bead geometry of the weld in etched condition (**c**)

It can be seen that the proposed heat source model provides a good description of the temperature distribution during both heating and cooling cycles of the welding process. Below 500 K during the cooling cycle, the simulated temperature curve deviates from the experimental with a constant error of $< 10\%$. This indicates a need for further optimization of the radiation boundary conditions. However, considering that martensite formation in dual phase steel begins at about 673 K and proceeds athermally until its finish temperature, a marginal variation in M_s/M_f does not significantly alter the phase transformation kinetics in the model. Additionally, the weld bead geometry as seen in the Fig. 8c, corresponds to that of the melt pool obtained from the simulation.

Figure 8 shows the calculated temperature distribution in the weld joint. The various regions of the weld joint are marked with respect to the temperature observed during welding. The zones with temperature above and below the liquidus temperature (1790 K) represent the fusion zone and the heat affected zone respectively. The peak temperature in the fusion zone was approximately 3000 K while a steep gradient of temperature ranging from solidus to below Ac_1 can be seen in the heat affected zone (see Fig. 7a). According to the ASM hand book of welding [30] at high welding speeds the melt pool takes the shape of an elongated tear drop with a large trailing quadrant, similiar melt pool shape observed during the welding step is presented in the Fig. 8a.

Evolution of Phases and their Volume Fractions

The kinetics of phase transformation during welding was investigated using the metallurgical models presented in the previous section. At any instant of the welding
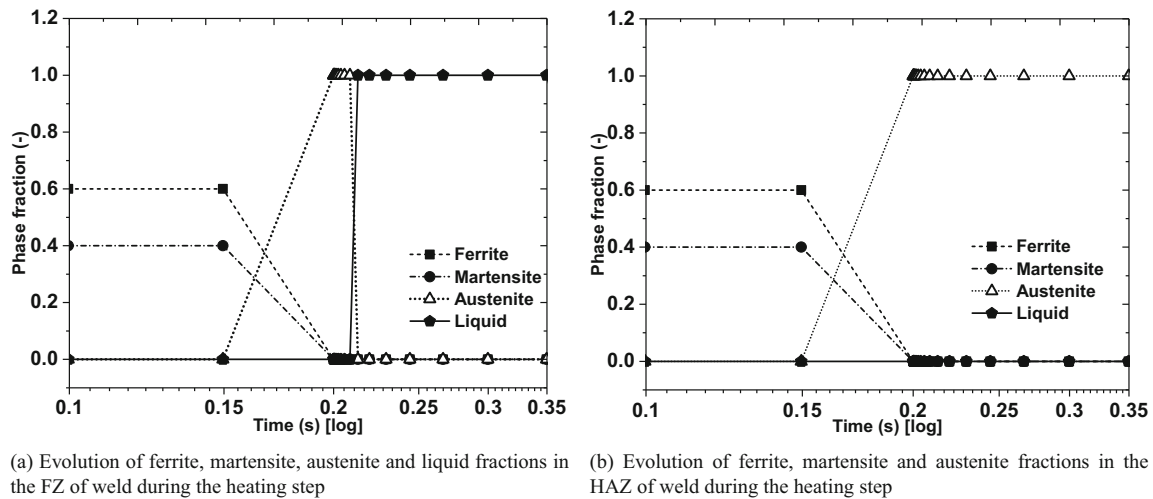
(a) Evolution of ferrite, martensite, austenite and liquid fractions in the FZ of weld during the heating step

(b) Evolution of ferrite, martensite and austenite fractions in the HAZ of weld during the heating step

Fig. 9 The evolution of various phases measured at distinct points in the FZ and HAZ during the heating cycle of welding expressed over log scale of time

process, the spatial distribution of individual phases can be obtained from the FE analysis. Fig. 9a & b illustrates the growth of austenite, the dissolution of martensite and ferrite phases above the Ac_1 temperature. Nakada et al. [31, 32] reported on the transition from diffusive to displacive reversion of austenite at high heating rates in low alloy steels. Applied austenization framework includes the effect of heating rate on the nucleation and growth of the austenite phase. The start and finish temperatures of any phase depend mainly on the alloying content and the grain size of the microstructure, however in this study the influence of grain size and distribution of alloying elements on the kinetics of phase transformation have not been taken into account. It will be a part of the authors future work. A homogeneous distribution of alloying elements in the weld microstructure is assumed. With further increase in temperature, depending on the vicinity of the point of interest to the locus of the heat source either melting or varying extent of austenization takes place. However, points away from the heat source that do not experience temperature changes above the Ac_1 do not undergo any phase transformations. Above the solidus temperature, melting of the material takes place and the liquid fraction starts to grow until the liquidus temperature, above which fully liquid phase exists. This region where the melting takes place forms the fusion zone while the regions surrounding it form the heat affected zone after the completion of welding. The evolution phases during the heating cycle in the fusion zone and the heat affected zones are presented in the Fig. 9

In general the phase diagram (see Appendix) can provide data on the transformation path under equilibrium conditions. During continuous cooling, depending on the composition of alloy, delta ferrite/austenite phase nucleates in the liquid and grows until the solidus temperature. This is followed by solid state phase transformations that lead to the decomposition of austenite into phases like ferrite, cementite and pearlite etc. However, welding is a rapid and non equilibrium process that produces phases such as bainite and martensite. Along with the rate of cooling, alloying elements like C, Mn, Cr etc. also have a significant influence on the transformation temperature of such phases. The presence of large fractions of Mn in the dual phase
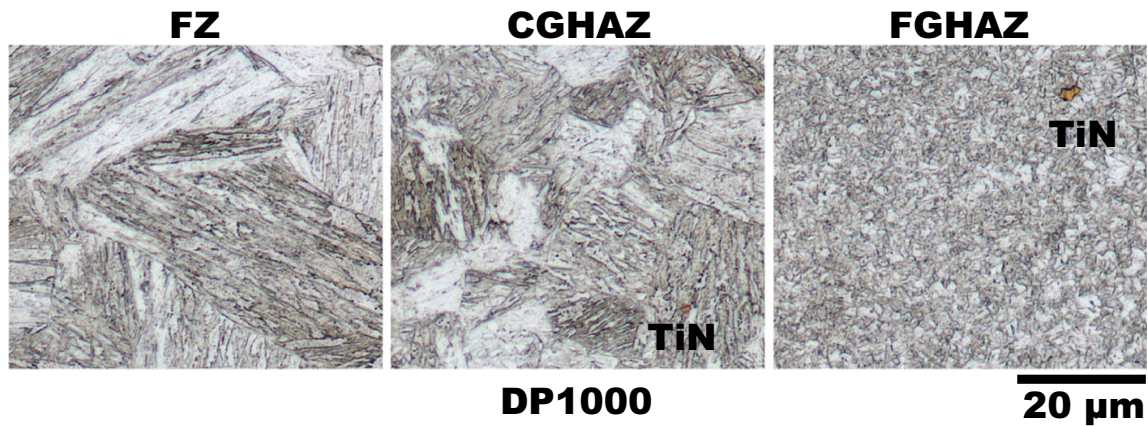
Fig. 10 Martensitic microstructure as seen in the micrographs taken from various regions of the weld joint

steel (refer to the Table 1) stabilized the austenite phase and the high rates of cooling that are typical to the electron beam welding of thin sheets, resulted in a fully martensitic microstructure in the FZ and the HAZ of the weld. In coarse grained
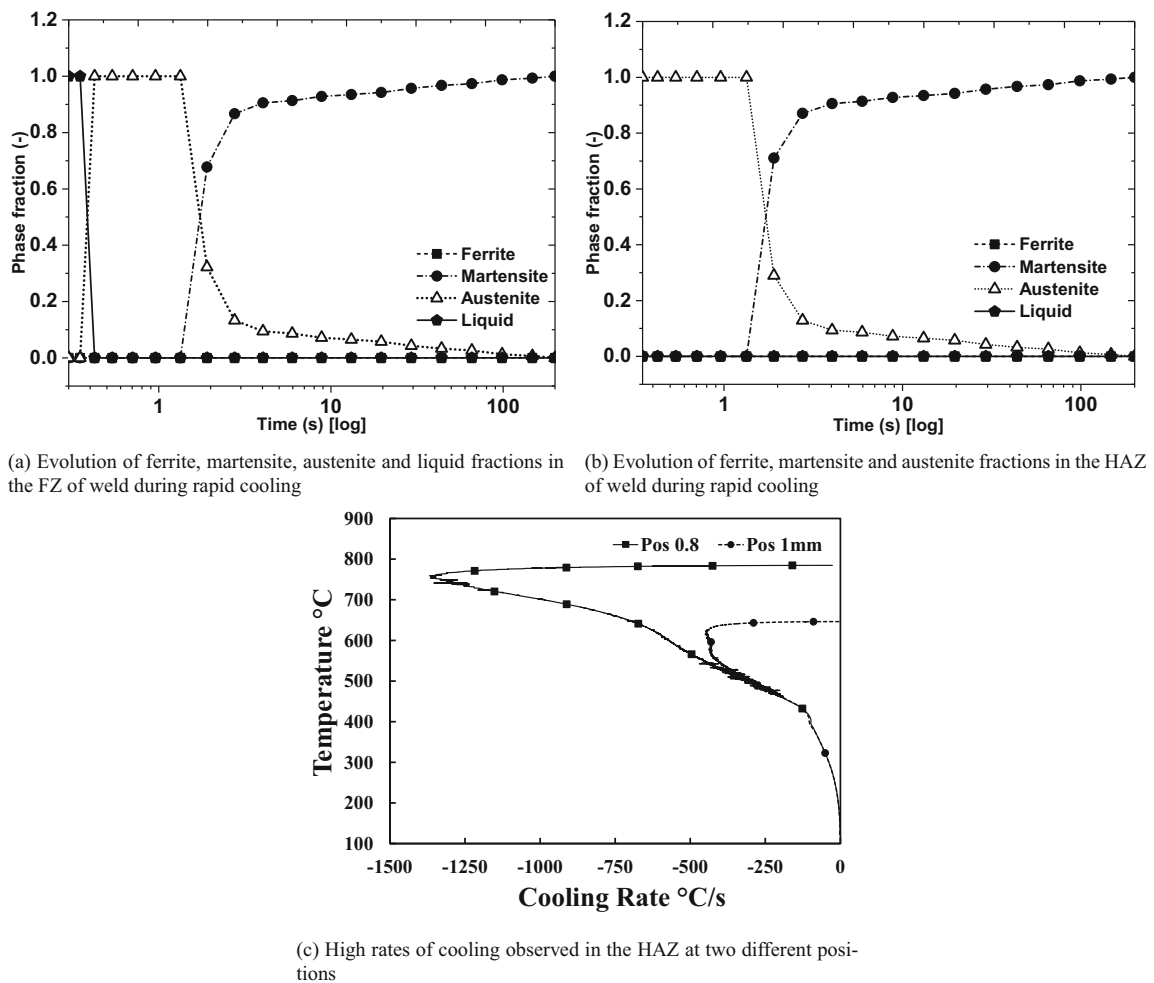

(a) Evolution of ferrite, martensite, austenite and liquid fractions in the FZ of weld during rapid cooling

(b) Evolution of ferrite, martensite and austenite fractions in the HAZ of weld during rapid cooling

(c) High rates of cooling observed in the HAZ at two different positions

Fig. 11 The evolution of various phase fractions measured at distinct points in the FZ and HAZ during the cooling cycle of welding expressed over log scale of time along (**a**), (**b**); High rates of cooling observed in the HAZ that lead to formation of fully martensitic microstructure in the weld joint (**c**)
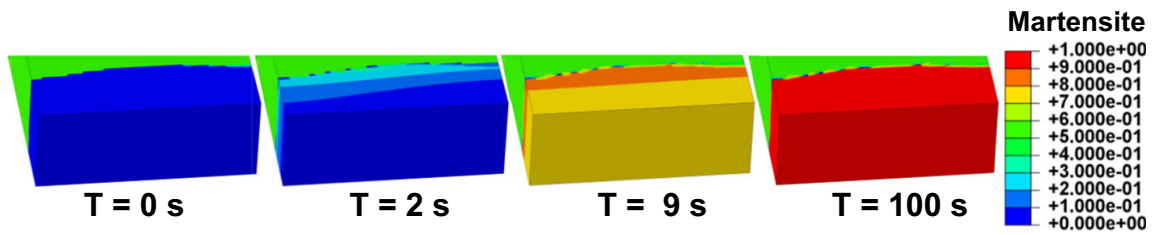
Fig. 12 Evolution and distribution of martensite fraction during the cooling cycle of the weld as observed in the FE simulation

and recrystallized zones of the HAZ, austenite usually decomposes into phases like martensite and bainite. Nearer to the fusion zone where, cooling rate is the highest and prior austenite grain size is the largest, HAZ exhibits predominantly martensitic microstructure. In the partially transformed zoned where, the cooling rate drops and prior austenite grain sizes are smaller, the HAZ can contain other softer phases. In this case however, the welding process parameters and smaller sheet thickness lead to cooling rates (see Fig. 11c) that surpassed the cooling rate needed to form bainite and resulted only in the formation martensite. The optical micrographs of the weld cross sections as shown in Fig. 10 confirmed the presence of a complete martensitic microstructure.

The Fig. 11 presents the evolution of martensite in both FZ and HAZ of the weld. The FZ exhibited solidification, where austenite nucleated and grew in the liquid phase. While the heat affected zone exhibited the transformation of parent phase into austenite during heating and then decomposed into martensite while cooling. The evolution of martensite fraction during the cooling cycle is presented in the Fig. 12. A near 100% martensite volume fraction can be seen in the simulated weld joint. In the transition region between BM and HAZ, increased presence of ferrite fraction can also be seen. The predicted result is in good agreement with the experimental observations.

Residual Stress

Residual stress refers to the stresses that remain in the weld joint after the welding process is completed. This stress induced by the thermal cycle(s) and metallurgical transformations is localized in the FZ and the HAZ of the weld seam. It springs from the misfit between the different phases or regions of the weld, that occurs due to the inhomogeneous thermal strain. In order to investigate such local residual stresses, finite element simulations were utilized. The thermo-metallurgical coupling as described in the previous section was applied in calculating the combined thermal and transformation strains that occur during welding. The Fig. 13a and b provide a comparison of the longitudinal residual stress obtained from both simulated and experimentally welded joints, along two different paths. The path 1 and path 2 (see Fig. 2) are positioned such that, the stress distribution could be adequately captured across the weld joint. Path 1 lies in the center of weld and is oriented along the direction of welding while, path 2 is oriented perpendicular to the weld line.
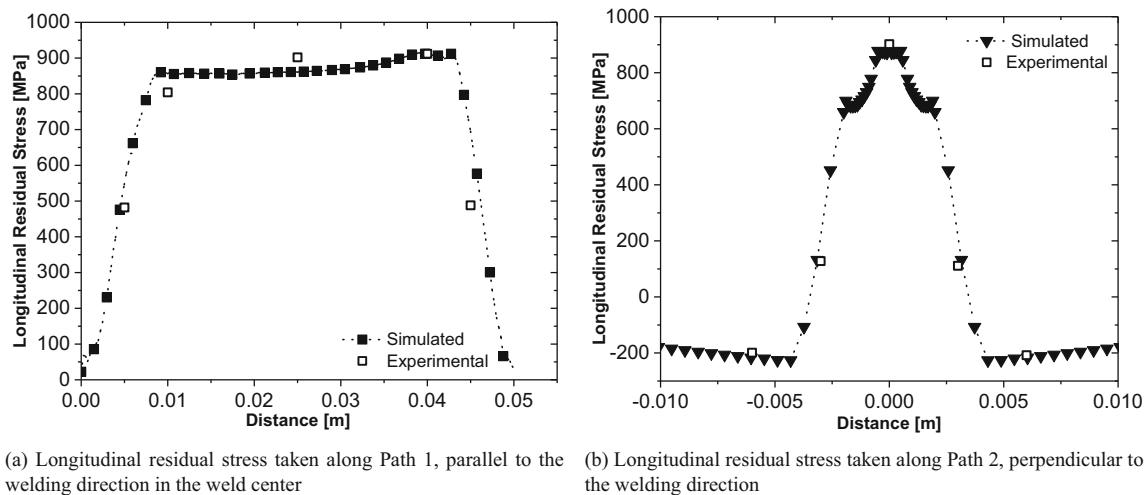
(a) Longitudinal residual stress taken along Path 1, parallel to the welding direction in the weld center

(b) Longitudinal residual stress taken along Path 2, perpendicular to the welding direction

Fig. 13 Comparison of the experimental and simulated longitudinal residual stress of the welded joint obtained along two different paths

A constant plateau of longitudinal tensile stress can be seen in the Fig. 13a along the weld line in the FZ until the free edges of the work pieces. This indicates that the heat input during the electron beam welding process was constant and as such resulted in high tensile residual stresses with magnitude over 850 MPa along the direction of welding. The magnitudes of maximum residual stresses are located in the FZ. This is the well-known evolution, that has been described for beam welding residual stresses [33–35]. These observations are due to the higher and lower temperatures generated respectively in the FZ and in the HAZ, leading to a temperature gradient occurring in a narrower zone hence generating higher residual stresses.

Directed outwards from the weld center, martensite expansion resulted in a significant mismatch of lattice between the weld regions and the BM. When induced stress on the lattice exceeds its yield strength, material plastically deforms and thereby lowers the mechanical stress. However, as the weld regions consisted of martensite in a predominantly quenched state with higher yield strength, larger elastic stresses were produced. Furthermore, thermal shrinkage introduced in the weld during cooling was also compensated by the increasing martensite fraction. Despite the compensation further increase in martensite volume fraction led to partial yielding and larger elastic straining. Along path 2 perpendicular to the welding line away from the weld center, compressive stresses were observed in the BM as seen in the Fig. 13b.

Experimental and numerical results showed the same trend of residual stresses in the studied zones. However, considerable differences between the experimental and simulated results can be clearly seen. These differences arose from the limitation of test methods applied. In the hole drilling method, material is removed from the surface and relaxation of the lattice is measured to estimate the residual stress. Representation of the same in a simulation where the removal of exact volume of elements from the model and estimation of mesh relaxation is a difficult task. For an exact comparison of the data with the FE simulation, advanced techniques like neutron diffraction or x-ray diffraction methods need to be applied which can precisely calculate the residual stress at defined positions in the welded samples.

Conclusions

– A sequentially coupled thermal-metallurgical and mechanical analysis was carried out to study the residual stress in dual phase steel subjected to electron beam welding.

– A modified 3 dimensional moving heat source model, combining conical and spherical thermal flux distributions, capable of accurately predicting the sharp temperature gradients observed across the various weld regions during high energy beam welding was developed and validated.

– A metallurgical framework wherein, the evolution of various phase fractions, the thermal and transformation strains was introduced. It was evident from the simulations that, the electron beam welding process provides a constant heat input along the weld line which resulted in high longitudinal tensile residual stress along the direction of welding.

– The martensite transformation that took place in the fusion zone and heat affected zone during the rapid cooling cycle of welding induced a massive volumetric misfit in weld regions close to the base material. As a consequence, high longitudinal residual stress in the weld centre and compressive residual stress in the transverse direction were observed.

– The experimental and simulated results exhibited similar trend in terms of residual stress with marginal differences, which arose due to the limitation of the quantification methods applied.

Appendix

Table 4 Thermal properties of dual phase steel as obtained from JmatPro [36]

Temperature ($^\circ$K)	Conductivity (W/mK)	Density kg/m^3	Specific Heat (J/kg)
298.15	34.70585	7840	448.25
373.15	36.49009	7791	481.44
473.15	37.60437	7759.05	525.58
573.15	37.33364	7725.29	576.48
673.15	36.03873	7689.66	642.95
973.15	29.7307	7595.88	1041.05
1073.15	26.85804	7620.78	1008.88
1173.15	27.79551	7573.3	613.4
1273.15	29.02907	7517.92	631.32
1373.15	30.26199	7463.09	647.5

Table 4 (continued)

Temperature (°K)	Conductivity (W/mK)	Density kg/m^3	Specific Heat (J/kg)
1473.15	31.49267	7409.04	663.6
1573.15	32.72451	7354.92	678.03
1773.15	34.17097	7100.72	8198.55
1873.15	35.21316	6886.66	826.19
1973.15	37.06	6803.04	826.41
2073.15	38.9065	6717.32	826.6
2173.15	40.75266	6629.73	826.73
2273.15	42.59848	6540.5	826.76
2373.15	44.44396	6449.84	826.78
2473.15	46.2891	6357.98	826.8
2573.15	48.1339	6265.12	826.82
2673.15	49.97837	6171.46	826.84
2773.15	51.82251	6077.19	826.85
2873.15	53.66631	5982.5	826.87
2973.15	55.50978	5887.55	826.88
3073.15	57.35291	5792.51	826.89

Table 5 Latent heat of fusion taken from [37]

Latent Heat (J/kg)	Solidus Temperature (°K)	Liquidus Temperature (°K)
246000	1741	1787
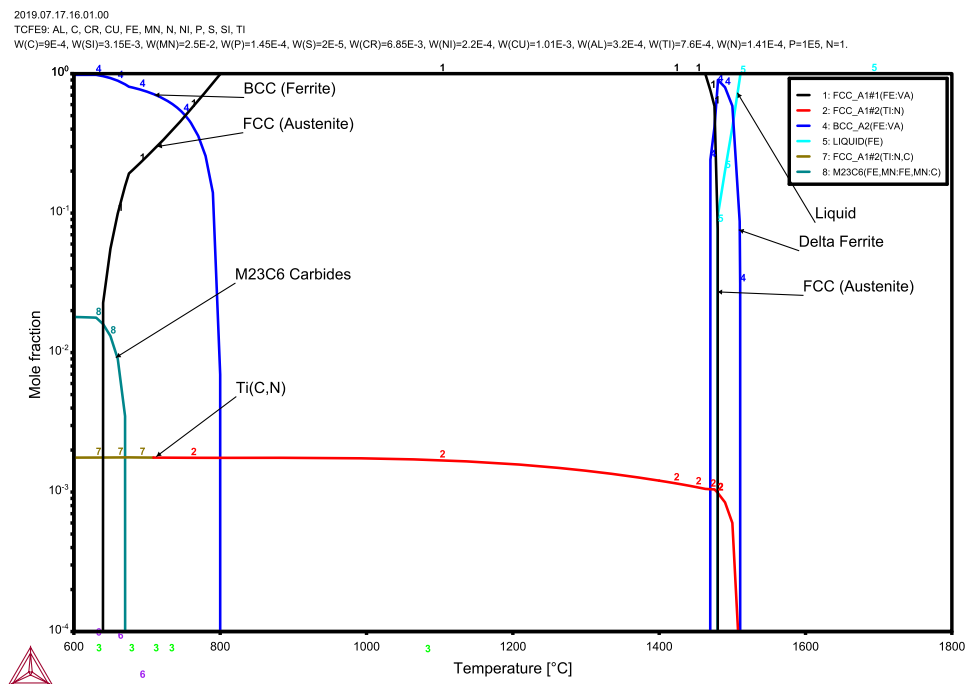
Fig. 14 Equilibrium phase diagram of dual phase steel calculated using the Calphad based tool Thermo-Calc

References

1. Flint, T., Francis, J., Smith, M., Balakrishnan, J.: Extension of the double-ellipsoidal heat source model to narrow-groove and keyhole weld configurations. Journal of Materials Processing Technology **246**(Supplement C), 123–135 (2017). https://doi.org/10.1016/j.jmatprotec.2017.02.002. http://www.sciencedirect.com/science/article/pii/S0924013617300468

2. Pamnani, R., Vasudevan, M., Jayakumar, T., Vasantharaja, P., Ganesh, K.: Numerical simulation and experimental validation of arc welding of dmr-249a steel. Defence Technology **12**(4), 305–315 (2016). https://doi.org/10.1016/j.dt.2016.01.012. http://www.sciencedirect.com/science/article/pii/S2214914716300010

3. Mi, G., Zhan, X., Wei, Y., Ou, W., Gu, C., Yu, F.: A thermal–metallurgical model of laser beam welding simulation for carbon steels. Modelling and Simulation in Materials Science and Engineering **23**(3), 035010 (2015). http://stacks.iop.org/0965-0393/23/i=3/a=035010

4. Xia, J., Jin, H.: Numerical modeling of coupling thermal–metallurgical transformation phenomena of structural steel in the welding process, Advances in Engineering Software, https://doi.org/10.1016/j.advengsoft.2017.08.011. http://www.sciencedirect.com/science/article/pii/S0965997817303952

5. Bhadeshia, H., Wayman, C.: 9 - phase transformations: Nondiffusive. In: Laughlin, D.E., Hono, K. (eds.) Physical Metallurgy, vol. 5, pp. 1021–1072. Elsevier, Oxford (2014). https://doi.org/10.1016/B978-0-444-53770-6.00009-5. https://www.sciencedirect.com/science/article/pii/B9780444537706000095

6. Deng, D., Murakawa, H.: Numerical simulation of temperature field and residual stress in multi-pass welds in stainless steel pipe and comparison with experimental measurements. Computational Materials Science **37**(3), 269–277 (2006). https://doi.org/10.1016/j.commatsci.2005.07.007. http://www.sciencedirect.com/science/article/pii/S0927025605002624

7. Deng, D.: FEM prediction of welding residual stress and distortion in carbon steel considering phase transformation effects. Materials and Design **30**(2), 359–366 (2009). https://doi.org/10.1016/j.matdes.2008.04.052. http://www.sciencedirect.com/science/article/pii/S0261306908001556

8. Kumar, S., Kundu, A., Venkata, K., Evans, A., Truman, C., Francis, J., Bhanumurthy, K., Bouchard, P., Dey, G.: Residual stresses in laser welded astm a387 grade 91 steel plates. Materials Science and Engineering: A **575**(Supplement C), 160–168 (2013). https://doi.org/10.1016/j.msea.2013.03.046 . http://www.sciencedirect.com/science/article/pii/S092150931300316X

9. Hamelin, C.J., Muránsky, O., Smith, M.C., Holden, T.M., Luzin, V., Bendeich, P.J., Edwards, L.: Validation of a numerical model used to predict phase distribution and residual stress in ferritic steel weldments. Acta Materialia **75**(Supplement C), 1–19 (2014). https://doi.org/10.1016/j.actamat.2014.04.045. http://www.sciencedirect.com/science/article/pii/S1359645414002961

10. Ni, J., Wahab, M.A.: A numerical kinematic model of welding process for low carbon steels. Computers and Structures **186**(Supplement C), 35–49 (2017). https://doi.org/10.1016/j.compstruc.2017.03.009. http://www.sciencedirect.com/science/article/pii/S0045794917300445

11. Khan, S., Bhadeshia, H.: Kinetics of martensitic transformation in partially bainitic 300m steel. Materials Science and Engineering: A **129**(2), 257–272 (1990). https://doi.org/10.1016/0921-5093(90)90273-6. http://www.sciencedirect.com/science/article/pii/0921509390902736

12. Jones, S., Bhadeshia, H.: Kinetics of the simultaneous decomposition of austenite into several transformation products. Acta Materialia **45**(7), 2911–2920 (1997). https://doi.org/10.1016/S1359-6454(96)00392-8. http://www.sciencedirect.com/science/article/pii/S1359645496003928

13. Takahashi, M., Bhadeshia, H.K.D.H.: A model for the microstructure of some advanced bainitic steels. Materials Transactions JIM **32**(8), 689–696 (1991). https://doi.org/10.2320/matertrans1989.32.689

14. Wang, Q., Liu, X., Wang, P., Xiong, X., Fang, H.: Numerical simulation of residual stress in 10ni5crmov steel weldments. Journal of Materials Processing Technology **240**(Supplement C), 77–86 (2017). https://doi.org/10.1016/j.jmatprotec.2016.09.011. http://www.sciencedirect.com/science/article/pii/S0924013616303338

15. Sun, X., Choi, K., Liu, W., Khaleel, M.: Predicting failure modes and ductility of dual phase steels using plastic strain localization. International Journal of Plasticity **25**(10), 1888–1909 (2009). https://doi.org/10.1016/j.ijplas.2008.12.012. http://www.sciencedirect.com/science/article/pii/S0749641908001897

16. Ramazani, A., Mukherjee, K., Schwedt, A., Goravanchi, P., Prahl, U., Bleck, W.: Quantification of the effect of transformation-induced geometrically necessary dislocations on the flow-curve modelling

of dual-phase steels. International Journal of Plasticity **43**, 128–152 (2013). https://doi.org/10.1016/j.ijplas.2012.11.003. http://www.sciencedirect.com/science/article/pii/S0749641912001684

17. Tasan, C., Hoefnagels, J., Diehl, M., Yan, D., Roters, F., Raabe, D.: Strain localization and damage in dual phase steels investigated by coupled in-situ deformation experiments and crystal plasticity simulations. International Journal of Plasticity **63**, 198–210 (2014). deformation Tensors in Material Modeling in Honor of Prof. Otto T. Bruhns. https://doi.org/10.1016/j.ijplas.2014.06.004. http://www.sciencedirect.com/science/article/pii/S0749641914001260

18. Minami, H., Nakayama, K., Morikawa, T., Higashida, K., Toji, Y., Hasegawa, K.: Effect of tempering conditions on inhomogeneous deformation behavior of ferrite-martensite dual-phase steels. Tetsu-to-Hagane **97**(9), 493–500 (2011). https://doi.org/10.2355/tetsutohagane.97.493

19. Hasegawa, K., Toji, Y., Minami, H., Ikeda, H., Morikawa, T., Higashida, K.: Effect of martensite fraction on tensile properties of dual-phase steels. Tetsu-to-Hagane **98**(6), 320–327 (2012). https://doi.org/10.2355/tetsutohagane.98.320

20. Gach, S., Olschok, S., Francis, J.A., Reisgen, U.: Confirmation of tensile residual stress reduction in electron beam welding using low transformation temperature materials (LTT) as localized metallurgical injections – Part 2: Residual stress measurement. Materials Testing **59**(7-8), 618–624 (2017). https://doi.org/10.3139/120.111046

21. Hibbit, Karlsson, Sorensen: ABAQUS/Standard Analysis User's Manual. Hibbit, Karlsson, Sorensen Inc., USA (2017)

22. Goldak, J., Chakravarti, A., Bibby, M.: A new finite element model for welding heat sources. Metall. Trans. B **15**(2), 299–305 (1984). https://doi.org/10.1007/BF02667333

23. Ronda, J., Oliver, G.: Consistent thermo-mechano-metallurgical model of welded steel with unified approach to derivation of phase evolution laws and transformation-induced plasticity. Computer Methods in Applied Mechanics and Engineering **189**(2), 361–418 (2000). https://doi.org/10.1016/S0045-7825(99)00461-2. http://www.sciencedirect.com/science/article/pii/S0045782599004612

24. Deng, D., Murakawa, H.: Finite element analysis of temperature field, microstructure and residual stress in multi-pass butt-welded 2.25cr–1mo steel pipes. Computational Materials Science **43**(4), 681–695 (2008). https://doi.org/10.1016/j.commatsci.2008.01.025. http://www.sciencedirect.com/science/article/pii/S0927025608000219

25. Caballero, F.G., Capdevila, C., Andres, C.G.D.: Modelling of kinetics of austenite formation in steels with different initial microstructures. ISIJ Int. **41**(10), 1093–1102 (2001). https://doi.org/10.2355/isijinternational.41.1093

26. Thiessen, R.G.: Physically-based modelling of material response to welding. Ph.D. thesis, Delft University of Technology (2006)

27. Wilson, E., Medina, S.: Application of koistinen and marburger's athermal equation for volume fraction of martensite to diffusional transformations obtained on continuous cooling 0·13%c high strength low alloy steel. Mater. Sci. Technol. **16**(6), 630–633 (2000). https://doi.org/10.1179/026708300101508397

28. Pan, H.H., Weng, G.J.: Thermal stress and volume change during a cooling process involving phase transformation. J. Therm. Stresses **15**(1), 1–23 (1992). https://doi.org/10.1080/01495739208946117

29. Motaman, S.A.H., Komerla, K., Storms, T., Prahl, U., Brecher, C., Bleck, W.: Experimental and numerical investigation of dual phase steels formability during laser-assisted hole-flanging. AIP Conference Proceedings **1960**(1), 060005 (2018). https://aip.scitation.org/doi/abs/10.1063/1.5034894

30. Lienert, T., Siewert, T., Babu, S., Acoff, V.: ASM handbook, Vol. 6A, ASM International (2011)

31. Nakada, N., Tsuchiyama, T., Takaki, S., Miyano, N.: Temperature dependence of austenite nucleation site on reversion of lath martensite, in: THERMEC 2009, Vol. 638 of Materials Science Forum, Trans Tech Publications, 2010, pp. 3424–3429. https://doi.org/10.4028/www.scientific.net/MSF.638-642.3424

32. Nakada, N., Tsuchiyama, T., Takaki, S., Ponge, D., Raabe, D.: Transition from diffusive to displacive austenite reversion in low-alloy steel. ISIJ Int. **53**(12), 2275–2277 (2013). https://doi.org/10.2355/isijinternational.53.2275

33. Kouadri-Henni, A., Seang, C., Malard, B., Klosek, V.: Residual stresses induced by laser welding process in the case of a dual-phase steel dp600: Simulation and experimental approaches. Materials and Design **123**, 89–102 (2017). https://doi.org/10.1016/j.matdes.2017.03.022. http://www.sciencedirect.com/science/article/pii/S0264127517302617

34. ul Abdein, M.Z., Nelias, D., Jullien, J.-F., Deloison, D.: Prediction of laser beam welding-induced distortions and residual stresses by numerical simulation for aeronautic application. Journal of Materials

Processing Technology **209**(6), 2907–2917 (2009). https://doi.org/10.1016/j.jmatprotec.2008.06.051. http://www.sciencedirect.com/science/article/pii/S0924013608005542

35. Xia, M., Biro, E., Tian, Z., Zhou, Y.N.: Effects of heat input and martensite on haz softening in laserwelding of dual phase steels. ISIJ International **48**(6), 809–814 (2008). https://www.jstage.jst.go.jp/article/isijinternational/48/6/48_6_809/_pdf

36. Saunders, N., Guo, U.K.Z., Li, X., Miodownik, A.P., Schillé, J.P.: Using jmatpro to model materials properties and behavior. JOM **55**(12), 60–65 (2003). https://doi.org/10.1007/s11837-003-0013-2

37. Li, X., Wang, L., Yang, L., Wang, J., Li, K.: Modeling of temperature field and pool formation during linear laser welding of dp1000 steel. J Mater. Process. Technol. **214**(9), 1844–1851 (2014). https://doi.org/10.1016/j.jmatprotec.2014.03.030. http://www.sciencedirect.com/science/article/pii/S092401361 4001216

Affiliations

Krishna Komerla[1] [iD] **· Stefan Gach[2] · Fatma Akyel[2] · Thomas Vossel[3] · Uwe Reisgen[2] · Wolfgang Bleck[4]**

Stefan Gach
gach@isf.rwth-aachen.de

Fatma Akyel
akyel@isf.rwth-aachen.de

Thomas Vossel
T.Vossel@gi.rwth-aachen.de

Uwe Reisgen
reisgen@isf.rwth-aachen.de

Wolfgang Bleck
bleck@iehk.rwth-aachen.de

[1] Steel Institute IEHK, RWTH Aachen University, Intzestr. 1, 52072 Aachen, Germany

[2] Welding and Joining Institute ISF, RWTH Aachen University, Pontstr. 49, 52062 Aachen, Germany

[3] The Foundry Institute GI, RWTH Aachen University, Intzestr. 5, 52072 Aachen, Germany

[4] Steel Institute IEHK, RWTH Aachen University, Aachen, Germany

4 Discussion

4.1 Influence of beam oscillations on weld geometry, microstructure and mechanical properties

As discussed in the previous chapter, besides the chemical composition and initial microstructure of the base materials, the welding process parameters largely influence the final microstructure of welds and their mechanical properties. From the industry point of view, it has been common practice to correlate the weld metal properties with heat input provided during welding. Although this approach seems very practical, it does not properly assess, the effect of individual welding process parameters. It has been found that under identical heat input conditions, the weld metal exhibits different microstructures when process parameters are varied [35].

In the case of EBW, this idea was adopted to enhance the weld metal properties (see section 3.1). The overall heat input which is a function of acceleration voltage (U), beam current (I), the energy absorption coefficient (η) and the welding speed (v), was kept constant during the different welding trials. However, in some of the trials beam oscillations were adopted as a process parameter. With frequencies as low as 500 Hz, beam oscillation along the chosen circular trajectory created a variation in the dynamic distribution of power around the stationary position of the beam. This resulted in a significant change of thermal flux in the keyhole. It is for this reason that the usual nail like weld geometry was replaced by a more homogeneous conical shape as shown in the Fig. 4.1.

For the identical heat input, just by introducing beam oscillations, an increased interaction volume of the beam with the work piece was achieved, which led to wider fusion and heat affected zones. There are multiple advantages with adopting beam oscillation as a viable process parameter. Firstly, the homogeneity of the weld metal properties were greatly improved due to increased soaking time and reduced cooling rate. Secondly, oscillations created a kind of stirring effect, where the melt pool was churned, allowing for better material mixing and reduced the formation segregations in the FZ. Furthermore, by redistributing the electron bombardments via beam oscillation, the formation of crowns and under cuts in the welds were reduced. As the keyhole expands due to the oscillations, the associated power density at the bottom of the keyhole was lowered which resulted in reduced penetration depth of the beam. However, this reduction was only minimal and did not affect the weld quality. Clean joints with complete through welds were obtained.

4.1.1 Weld microstructure

Alloy composition, metallurgical processes like melting, solidification, solid-state phase transformations, grain refinement and dynamic recrystallization etc. that take place during welding are directly responsible for the development of weld
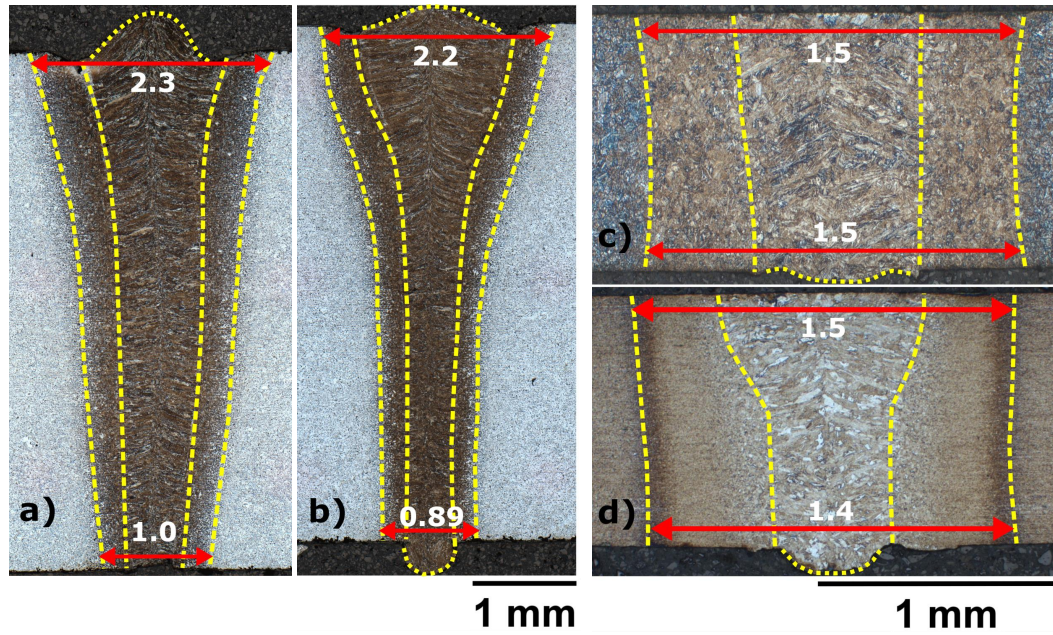
Figure 4.1: Micrographs of S235JR (a & b) and DP (c & d) steel weld joints obtained with oscillated & stationary beam welding [12]

microstructures and thus also affect the final mechanical properties of the weldments. Many of these metallurgical processes are triggered by thermal and external loads applied during welding. By understanding the impact of these metallurgical phenomena on the final weld behaviour, enhanced and durable joints can be produced. During EBW, the intense heat induced by the bombardment of electrons resulted in a variety of microstructural states across the different weld regions. The FZ experiences the highest temperature, above the liquidus and exhibits solidification microstructure. A competitive growth of weld metal grains occurred along the highest temperature gradients and the easy crystallographic orientation which for cubic metals is the [100] direction. According to the ASM handbook on welding [26], at high welding speeds, the melt pool takes the shape of an elongated tear drop where the S/L interface is straight and results in the axial growth of columnar grains from the fusion line towards the centre of weld. In the FZ, such a behaviour was observed where, spontaneous epitaxial solidification took place such that large columnar grains nucleated from the fusion line and grew towards the centre of the melt pool. However, this tendency varied slightly for thicker weldments. Despite higher welding speeds, increased thickness led to the entrapment of heat at the weld centre and altered the melt pool dynamics. This difference was clearly seen between the thin DP1000 and thicker S235JR steel alloys. The melt pool in the case of thicker weldments took a more circular shape and produced a curvature in the S/L interface line. As seen in the previous results section, for thicker sections the columnar grains curved towards the weld line at centre of the weld.

On the other hand, HAZ corresponds to temperatures that are high enough to cause metallurgical transformations, but are too low to cause melting. A wide range of peak temperatures were seen across the various CGHAZ, FGHAZ and the intercritical zones. Peak temperature in the HAZ increased with the decreasing distance

to the weld centre. Grain growth in crystalline materials is a function of time and temperature; therefore, CGHAZ as the name suggests, exhibited the maximum grain size. With beam oscillations, more heat is trapped in the weld which dissipates slower than usual leading to lower cooling rates in the CGHAZ and the other HAZ regions. As such grains were exposed to higher temperatures for longer durations leading to coarsening and other solid-state phase transformations. The microstructure of S235JR weld joints consisted primarily of martensite, small fraction of bainite and ferrite phases. While DP steel joints consisted a fully martensitic microstructure in the FZ and the HAZ. This behaviour is dependent primarily on the alloy composition and the welding thermal treatment. In regions where temperature exceeded the AC_1 during the heating cycle of welding, FCC austenite phase forms and decomposes into either martensite or bainite depending upon the rate of cooling. Under rapid quenching which is typically the case in welding, the austenite lattice doesn't have sufficient time to rearrange itself into BCC ferrite, instead it shears into a BCT structure trapping the interstitial carbon atoms that were dissolved previously in the austenite phase. This martensite transformation is non-diffusional and occurs solely due to the coordinated rearrangement of the austenite lattice. Bainite formation however, involves both shear and diffusional processes. In any case, such shearing of lattice is almost always accompanied by massive volumetric dilatations. This is one of the major reasons for the generation of residual stresses in weld joints. Microstructure under stress tends to deform in order to minimize its internal forces, but the lack of slip planes in such sheared lattices restricts their plastic deformation leading to the build up of excess elastic stresses.

4.1.2 Mechanical properties

Process parameters have a significant impact on the mechanical behaviour of weld joints. It is clearly seen in the results presented in the previous chapter. Microhardness, tensile tests and in some cases bending tests were applied to study the weld joints performance.

4.1.2.1 Microhardness

In the case of EBW joints, the microhardness maps exhibited a clear distinction in hardness between the various weld regions. Beam oscillations resulted in lower hardness in comparison to the stationary beam welds. As the microstructure in both the alloys was dominantly martensitic, it is clear that the hardness can be associated to the entrapment of carbon at the interstitial sites in lattice. The higher the carbon fraction, the higher is the hardness, as larger interstitial atomic presence leads to greater shearing and produces stiffer BCT phases. Beam oscillations as discussed earlier, result in entrapment of heat across the weld, leading to lower cooling rates, i.e, the locally in weld zones temperature drops slower than usual. As a consequence, an indirect tempering takes place that significantly lowers the hardness of welds. Besides carbon fraction, grain size also plays a crucial role. According to the Hall-Petch relationship, grain size and hardness are inversely proportional to each other. With longer exposure time to heat, grains coarsen or grow larger leading to reduced hardness in the FZ and CGHAZ. Larger grains tend to promote additional

pile up of dislocations at grain boundaries or lath boundaries which lowers the energy barrier for dislocation propagation. This complacency is evident from the lower hardness values. Furthermore, because welding is a transient thermal process and the heat transfer across the weld is heterogeneous, carbon rich /depleted zones are created. This is the reason for such a gradient in strength of different weld regions. In addition to the above, softening of martensite in the HAZ regions close to the BM was also seen. An indirect tempering of existing martensite during welding lowers the hardness further in these regions. This tempering is undesired but the beam oscillation created the conditions for such softening by enlarging the HAZ and varying the temperature distribution.

4.1.2.2 Tensile and bending strength

Tensile and bending characteristics of weld joints are studied in order to determine their strength and ductility. It is of paramount importance that the weld joints exhibit over matching strength, i.e, weld joints are stronger and more resilient than the base materials. Generally in welding, the microstructure of the welded region is drastically different from the base material and as such they possess unique mechanical properties. S235JR is a typical structural steel that exhibits yield point elongation during deformation. Its engineering stress-strain curve can be divided into a linear elastic regime until the upper yield point, a yield regime where the stress drops to the lower yield point and stagnates until the Lüders strain and finally a hardening regime with rise in stress until the ultimate tensile stress, after which necking leads to failure. The yield point elongation in these steel grades occurs primarily due to the movement of an invariant deformation profile (Lüders band) along the tensile axis. The deformation associated with such Lüders deformation usually exhibits quasi-stationary behaviour with small strains and constant deformation rate that results in a stagnant extension rate with no work hardening. The yield regime of the weld joint revealed that the BM exhibits a Lüders strain which is more than twice that of the stationary and oscillated beam welded joints. The reason for this decrease is simply the presence of weld joint consisting of hard and strong phases like martensite, that reduce the effective length of band propagation. As seen in the Fig. 4.2, a first instance of Lüders band nucleates in the BM of the tensile specimen which then propagates until it reaches the weld seam. At the end of which another Lüders band nucleates and propagates in the other side of the weld seam while the first half undergoes hardening. With this half already approaching necking, the complete deformation potential of the other half remains untapped. This is the reason for the drop in yield point elongation behaviour of these welds. Beam oscillation inherently broaden the weld seam which further affects the length of the band, leading to a decrease in the overall elongation of the weld. In the DP steels however, no such behaviour can be seen. Simply because DP steels do not undergo yield point elongation. However, the effect of beam oscillation is still similar to the S235JR steels. The overall elongation of the weld specimens depended solely on the width of the weld seam.

Three point bending tests were carried out on the weld joints in order to study their resilience to bending loads. Typically, both tensile and compressive loads are introduced into the samples during a bending test. In both materials, oscillated

(a) Yield regime depicting the variation in Lüders strain for BM & weld joints of S235JR alloy

(b) Nucleation and growth of Lüders band in the S235JR BM and oscillated weld sample (K) at various macroscopic strains
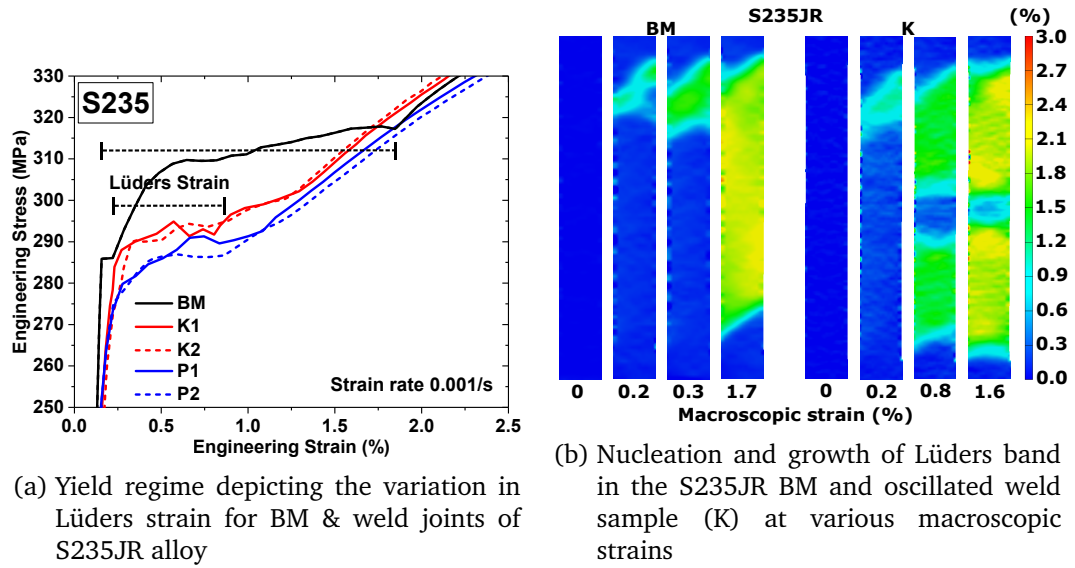
Figure 4.2: Comparison of yield point elongation in S235JR BM and weld joints along with the evolution of Lüders band in the tensile direction [12]

beam welded joints exhibited good ductility and strength. They also helped in reducing the hardness of welds and thus improved their load bearing capability.

4.2 Influence of tool offset on dissimilar friction stir welding of Fe-Al joints

A detailed study has been reported for FSW in the section 3.2. Generally, the process of friction stir welding involves, a cylindrical tool comprising a shoulder and a profiled pin, which is rotated and slowly plunged into work pieces that are butted or lapped together. It is a practice to place the tool in the centre of the weld line to maintain a uniform heat input in both the weld pieces. But for dissimilar welding of steel and aluminum together, such a strategy resulted in the formation of detrimental inter-metallic Al-Fe compounds, that underwent brittle failure. Tool geometry and contact loads are the prime factors that controlled the material flow and heat input across the weld. By adopting tool offset i.e., by displacing the tool centre towards the retreating side more heat was input in aluminum than in steel. This resulted in dynamic recrystallization, grain coarsening and growth in the Al alloy. Additionally, due to the axial load and rotational movement of the tool shoulder, material from the surface and subsurface was pushed downward, while in layers around the cavity created by the pin, material flow was directed upwards. As the tool advanced, material from the leading edge filled the space created behind the pin in the form of stacked layers. A dynamic balance was established between the downward flow of material from the surface with the upward flow of material from the cavity to produce a defect free weld. High axial load along with tool offsetting reduced defect size and limited the amount of chips that were embedded in the joint. Kumar et al. [36] also reported a similar observation upon the influence of axial loads on the defect size and reported that beyond a critical value of axial load,

defects were completely eliminated. Furthermore, the rotational forces exerted by the shoulder scraped away steel from the surface in the form of chips that get embedded in the weld during material transport. These chips act as discontinuities and weaken the established bonding. Because of the tool position offsetting however, the interaction of tool shoulder with steel was reduced and fewer chips of steel were removed and embedded in the weld joint.

4.2.1 Dynamic recrystallization and grain size

In contrast to fusion welding methods, the metallurgical phenomena occurring during FSW are very different. As the process inherently does not involve melting but rather significantly deforming the work pieces, phenomena such as strain hardening, dynamic recrystallization become more relevant. Grain size has a significant influence on the mechanical properties of the crystalline materials. With enough driving force and thermal energy, dislocations glide through the lattice, distorting the crystal until their motion is impeded at the grain boundaries. The repulsive force generated by the subsequent pile up of such dislocations reduces the energy barrier for dislocation motion across the grain boundary. Decreasing the grain size decreases the amount of pile up and increases the applied stress required to drive the dislocations across the grain boundaries. Therefore, fine grained microstructures exhibit increased strength due to such hardening effect where greater ratios of grain boundary to dislocations are seen.

During FSW, depending on the welding parameters a wide range of grain sizes can be produced. The microstructure of the Al alloy consisted of equiaxed grains with an average grain size of $40\ \mu m$ in the cold rolled state. The position offsetting, led to extensive contact of the tool with Al alloy and as a result most of the frictional heat and deformation induced were localized in the Al alloy. As a consequence, significantly smaller grains were observed in WZ, TMAZ and HAZ. As shown in the Fig. 4.3, the CPD of grain size clearly demonstrates the variation of grain size across the various regions of the weld in the Al alloy. Despite the significant influence of the tool, the WZ contained equiaxed grains with over $8\ \mu m$ sizes. The misorientation between the grains was found to be less than $1°$ revealing that most of the deformation energy gained during welding was expended. This suggests significant thermal kinetics. Recrystallization and grain growth were observed as the causes for this behaviour. They are thermally driven mechanisms, achieved in materials at temperatures higher than 40% of their melting temperature (T_m). The combined effect of stirring and friction heat generated the necessary temperature and strain conditions for dynamic recrystallization of microstructure to occur in the Al alloy. New defect free grains nucleated and grew, consuming the deformed grains. While in the Fe alloy, a very different trend was observed. Severe plastic deformation was seen in the WZ, where grains were drastically refined and severely bent. Average grain size in the WZ of the Fe alloy was found to be around $1.5\ \mu m$ (see Fig. 4.4). Away from the weld line in the TMAZ and HAZ however, no significant variation in the microstructure was observed. This can be attributed to the very minimal influence of tool on the Fe alloy placed along the ascending side.
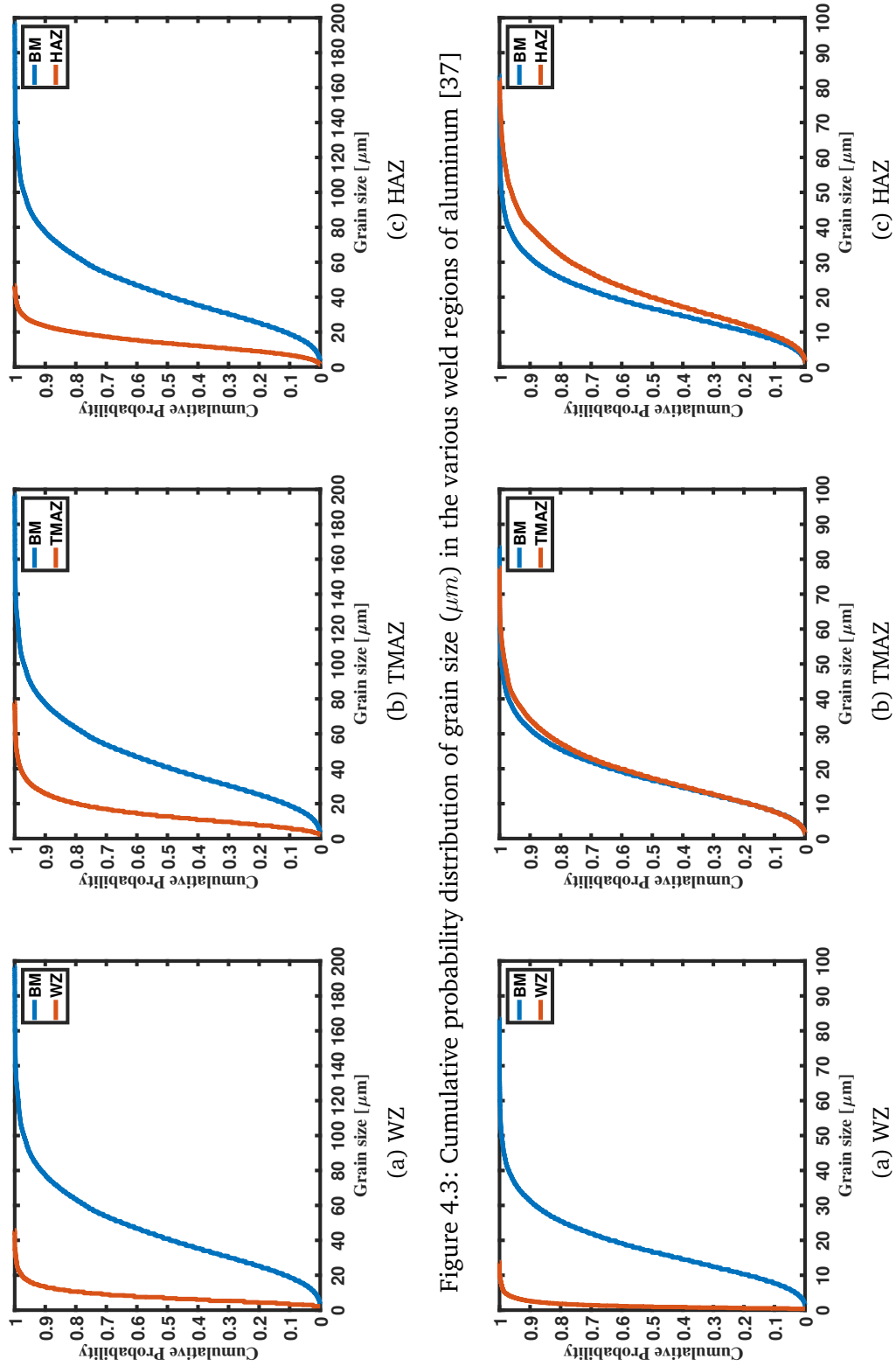
Figure 4.3: Cumulative probability distribution of grain size (μm) in the various weld regions of aluminum [37]

Figure 4.4: Cumulative probability distribution of grain size (μm) in the various weld regions of steel [37]

4.2.2 Microhardness

In the case of FSW, hardness is a function of grain refinement/coarsening, strain hardening and thermal softening. In the steel alloy, despite the minimal contact with the tool, layers that were close to the surface exhibited severe plastic deformation and contained a fine grained microstructure. Therefore higher hardness was seen at the surface which then drastically decreased with increasing distance along the thickness. This indicates a strong susceptibility of the weld to bending failure. Micro-cracks could develop at the surface and grow inward resulting in premature fracture. This risk can however be reduced by controlling the axial load levied on the ascending side; adjusting the tool tilt or by introducing a load control unit. While in the aluminum alloy, completely different tendency was seen. Deformation with high strain rates and high temperature resulted in the dynamic recrystallization of the microstructure, where all of the store strain energy was expended. With new grains and reduced dislocation density, the over strength of the weld region was lowered. Also, inherently the aluminum alloy through the ageing process contained fine precipitates, which provided the additional secondary particle strengthening. During the welding process these precipitates were either dissolved or coarsened resulting in a decrease of their density and homogeneity of distribution. Dynamic recrystallization combined with precipitate coarsening must lead to a decrease in the hardness of the weld, however hardness observed was similar to the BM. This is due to the fact that new precipitates nucleated in the weld during the cooling phase and relatively smaller grain sizes present in the weld compensated for any loss of strength that occurred due to the thermal processes.

4.3 Finite element thermal analysis

High energy beam welding technologies result in deep seams with narrow weld profiles, small heat affected zones and minimal distortion [38]. The intense heat adsorbed by the material causes rapid liquefaction followed by subsequent solidification in the fusion zone. It is imperative to study the thermal distribution in the weld joint to understand the microstructure arising from the various metallurgical phenomenon taking place during welding. However, it is a challenging task to precisely map the time-temperature history of the weld experimentally, especially at points that are in close proximity to the key hole. It is for this reason that numerical simulation methods are vastly sought after. The FE thermal analysis of the welding process can precisely provide the temperature distribution in the weld joint, through which, distortions and residual stresses can be predicted.

4.3.1 Heat source modelling

Welding is a complex thermo-chemo-mechanical process, under transient and non-equilibrium conditions, multiple metallurgical phenomena occur either sequentially or simultaneously. Severe distortions and high levels of residual stresses, that drastically reduce the resistance of weld structures against fracture, buckling, corrosion and others are the direct consequence of the thermal cycle caused by localized intense heat input. The thermal history, particularly soaking time at high temper-

atures and cooling below the Ac_3 temperatures up to about $500°$C determine the microstructure and mechanical properties for any given composition. Cooling from $400°$C to $100°$C is critical in controlling the diffusion of hydrogen and cold cracking of welds [38]. In order to obtain an optimal microstructure, it is imperative to obtain optimized process parameters but, experimental determination of these parameters is both time consuming and expensive. Hence there is a strong need for numerical models to predict the thermal history.

[39] first applied Fourier theory of heat flow to develop a moving heat source model that assumed either a point, line or plane of heat source. However the prediction of temperature near the FZ and HAZ were found to be erroneous. The infinite temperature at the heat source assumed in the model along with the materials thermal sensitivity increased the error fraction. [40] proposed a Gaussian distribution flux that was combined with FEM achieved improved power distribution in the FZ and HAZ but failed to accommodate complex geometries of the real weld pool. [38] introduced a moving volumetric heat source model capable of analysing the thermal history of shallow and deep penetration welds. The thermal distribution in the model was divided into leading and trailing quadrants to accommodate the difference in temperature gradients observed in the front and the back of the heat source. Fig. 4.5 depicts the heat source moving along the Z axis. The double ellipsoidal heat flux distribution was described as function of time in spatial coordinates *(x, y, z, t)*

$$q(x,y,z,t) = \frac{6\sqrt{3}f_iQ}{abc_i\pi\sqrt{\pi}}\exp(\frac{-3x^2}{a^2} + \frac{-3y^2}{b^2} + \frac{-3[z-v(\Delta t)]^2}{c_i^2}) \qquad (4.1)$$

where a, b, c_i are the width, depth and length of the front/rear quadrant; v is the weld speed and Δt the time interval.

[41, 42] developed a surface heat source model based on Gaussian distribution. [43] presented an adaptive rotary volumetric heat source model constructed by superimposing a number of Gaussian plane heat sources with different power densities along the thickness. [44] simulated the laser butt welding using a combination of double ellipsoidal and 3D Gaussian heat source models. The conical power density at any plane perpendicular to the weld line is given as

$$\mathbf{Qr} = \mathbf{Q_0}\exp\left(\frac{-r^2}{r_0^2}\right) \qquad (4.2)$$

where $r = \sqrt{x^2 + y^2}$ and $r_0 = r_e - \frac{(r_e-r_i)(z_e-z_i)}{(z_e-z_i)}$. Despite the efforts, the sharp temperature gradients observed at the root of welds between the FZ and HAZ could not be accurately reproduced through the existing models as the keyhole effect was not explicitly considered in them. In high energy beam welding processes, a narrow and focused beam is incident on the surface of work piece causing rapid melting and partial vaporization. The intense recoil pressure exerted by the vapour flux leads to the formation of a deep cavity or keyhole. To replicate such a behaviour, the heat source model must include a larger power distribution near the surface and a flux decay along the penetration depth. In this study a modified Goldaks heat source model capable of describing the varying heat input inside a keyhole was proposed. The total power density of the electron beam is divided into spherical and conical
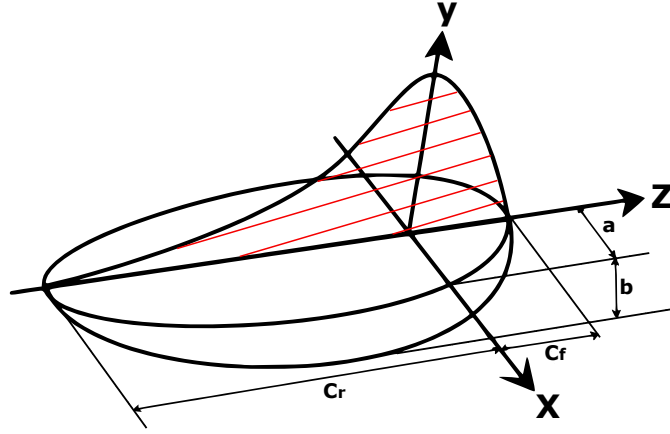
Figure 4.5: Double ellipsoid heat source configuration

parts as shown in the Fig. 4.6. The total flux distribution can be written as the sum or superposition of two different fluxes

$$Q_{EB} = Q_{Spherical} + Q_{Conical} \tag{4.3}$$

The flux density distribution within the spherical domain can be described by a Gaussian function as presented in Eq. (4.1).

$$Q_{Spherical} = (1 - \psi)\frac{6\sqrt{3}Q}{R_g^3 \pi \sqrt{\pi}} \exp\left[-3(\frac{x^2}{R_g^2} + \frac{y^2}{R_g^2} + \frac{[z - v(\Delta t)]^2}{R_g^2})\right] \tag{4.4}$$

where Q is the product of acceleration voltage (U), beam current (I) and energy absorption coefficient (η), while R_g is the radius of sphere. The high energy electrons impinging the work piece penetrate only the surface and rapidly transfer their kinetic energy to the surrounding material in the form of heat. This heat causes the material to melt and evaporate, leading to the formation of a gas channel at the centre of melt. However, the penetration depth of the electrons is less than an order of magnitude. As such, the power density of the beam is larger at the surface and decreases with increasing depth of the keyhole. Therefore, the flux distribution in the conical domain was built such that the volume of thermal flux decreases linearly with the increasing penetration depth. The Fig. 4.6b presents the distribution of combined heat flux as a function of position, where the flux is maximum at the centre of grid and decays to 0 with increasing distance away from the centre.

$$Q_{Conical} = \frac{3\psi Q}{\pi H R_0^2} \exp\left[-3(\frac{x^2}{R_0^2} + \frac{(z - v\Delta t)^2}{R_0^2})\right] \overbrace{\left[1 + 0.01(\frac{H - y}{H})\right]}^{\text{s}} \text{step}(H, y) \tag{4.5}$$

$$\text{step}(H, y) = \begin{cases} 0 & \text{if } H - y < 0.0 \\ 1 & \text{if } H - y \geq 0.0 \end{cases}$$
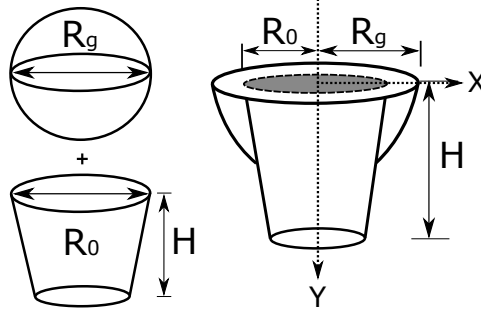
(a) Combined spherical & Conical heat source
   model
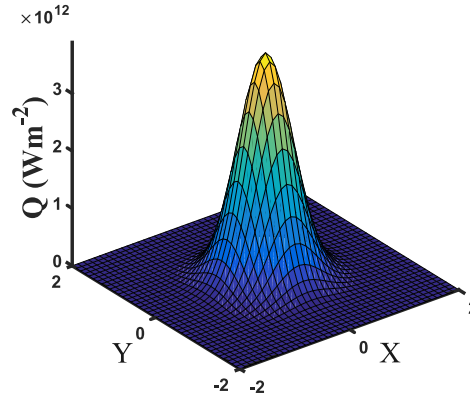
(b) Gaussian distribution of flux as function of
   position

Figure 4.6: Illustration of the volumetric heat source model along with the Gaussian
distribution of its thermal flux [45]

In the Eq. (4.5), H is the thickness of the work piece and R_0 is the base radius of the cone. The term '**S**' provides the negative slope where, with increasing y the available flux decreases linearly. Thereby the bottom portion of the cone contains lower flux density in comparison to the surface. Additionally, to strike a balance between the spherical and conical domains while accounting for the overlap of both fluxes, the term ψ was introduced in the equations such that the total fraction of thermal flux remains 1.0.

   As seen from the results, the thermal flux distribution model, provided an accurate description of the temperature during welding. It was however observed that during the cooling cycle, as temperature falls below 500 K, the time-temperature curve deviated from the experimental data with a constant error fraction of about 10 %. This suggests a need for the optimization of radiation boundary conditions. In the case of DP steel, as the martensite start and finish temperatures are above 500 K, this deviation does not influence the results. However, for cases where the martensite finish temperature is pushed below the 500 K limit. This could lead to erroneous prediction of the martensite phase fraction. This would also lead to the incorrect estimation of residual stresses in the weld joint.

4.4 Residual stress analysis

Residual stresses are locked-in stresses present in the engineering components even when there is no external load and these develop primarily due to non-uniform volumetric change in metallic component irrespective of manufacturing processes such as heat treatment, machining, mechanical deformation, casting, welding, coating etc. However, maximum value of residual stresses does not exceed the elastic limit of the metal because stresses higher than elastic limit leads to plastic deformation and thus residual stresses greater than elastic limit are accommodated in the form of distortion of components. Residual stresses can be tensile or compressive depending up on the location and type of non-uniform volumetric change taking place due to differential heating and cooling like in welding and heat treatment or localized stresses like in contour rolling, machining and shot peening etc.

During heating primarily compressive residual stresses were developed in the regions of HAZ due to thermal expansion. This thermal expansion was restricted by the surrounding base material that is at a lower temperature, where no significant expansion takes place. After attaining a peak value, these compressive residual stresses gradually decreased owing to softening of metal being heated. It eventually reduces to zero in the regions of weld where melting starts. A reverse trend was observed during the cooling stage. During cooling as metal starts to shrink, tensile residual stresses develop (only if shrinkage is not allowed either due to metallic continuity or constraint from job clamping) and their magnitude keeps on increasing until room temperature is attained. In general, greater the degree of constraint higher will be the value of residual stress. As stated earlier, residual stresses in the weld joints developed mainly due to the differential volumetric expansion and contraction of metal around the weld zone. This volumetric expansion or contraction occurs both at macroscopic and microscopic level. Macroscopic volumetric changes occurring during welding contribute to major part of residual stress development and are caused by a) varying expansion and contraction and b) different cooling rate experienced by top and bottom surfaces of weld & HAZ. Microscopic volumetric changes mainly occur due to metallurgical transformation (austenite to martensitic transformation) during cooling. Further, it is important to note that whenever residual stresses develop beyond the yield point limit, the plastic deformation sets in the component. If the residual stress magnitude is below the elastic limit then a stress system having both tensile and compressive stresses for equilibrium is developed.

The different temperature conditions lead to varying strength and volumetric changes in base metal during welding. As the heat source came closer to the point of interest, its temperature increased leading to the reduction in the yield strength of material and simultaneously caused thermal expansion. However, surrounding low temperature base metal restricted the thermal expansion which in turn led to the development of compressive strains in the metal during heating. This compressive strain initially increased non-linearly with increase in temperature due to variation in yield strength and expansion coefficient of metal with temperature rise. Further, increase in temperature softened the metal, therefore, compressive strain reduces gradually and eventually it is vanished. As the heat source starts moving away from the point of interest, temperature begins to decrease gradually and reduction in temperature causes the shrinkage of hot metal in base metal and HAZ. Initially at

high temperature contraction occurred without much resistance due to low yield strength of metal but the subsequent shrinkage of metal was resisted as the material gains strength due to the reduction in temperature during cooling regime of weld thermal cycle. Therefore, further contraction in shrinking base and weld metal was not allowed with reduction in temperature. This behaviour of contraction left the metal in a strained condition; meaning the metal which should have contracted, is not allowed to do so and this led to development of the tensile residual stresses. The residual stress along the weld is generally tensile in nature while balancing compressive residual stress is developed adjacent to the weld in HAZ on cooling to the room temperature.

4.4.1 Influence of metallurgical transformation

During welding, HAZ and FZ of steel invariably experience transformation of austenite into other phases phase mixture like pearlite, bainite or martensite. All these transformations occur with increase in specific volume at microscopic level. The transformations (from austenite to pearlite and bainite) occurring at high temperature are easily accommodated with this increase in specific volume owing to low yield strength and high ductility of these phases and phase mixtures at high temperature (above 550 °C) therefore such metallurgical transformations don't contribute much towards the development of residual stresses. However, transformation of austenite into martensite takes place at relatively very lower temperature with significant increase in specific volume. Hence, this transformation contributes significantly towards development of residual stresses. Depending upon the location of the austenite to martensitic transformation, residual stresses may be either tensile or compressive in nature. Irrespective of the nature of residual stresses, they affect the soundness, dimensional stability and mechanical performance of the weld joints.

5 Conclusions

In this thesis, certain uncommon welding process parameters have been defined and applied in an attempt to tailor the weld microstructure and mechanical properties of welded joints of low carbon steels. Through experimental and numerical simulations different welding strategies have been studied. The following conclusions can be drawn from this work

- Defining beam oscillations along a particular trajectory aids in proper mixing of material in the keyhole which, results in the reduction of segregations and improves weld joint quality. The oscillation of beam about a stationary position, even at low frequencies creates a dynamic distribution of heat inside the keyhole. This has a significant impact on the shape of weld pool and the weld nugget geometry.

- Beam oscillations do not particularly affect the morphology of the weld microstructure but produce considerable differences in the mechanical properties of the weld joints. Beam oscillations enhance the entrapment of heat in the weld which leads to lower cooling rates and an additional tempering like effect that lowers hardness and residual stresses in the weld joint.

- For enhanced product life, producing welds with beam oscillations is more efficient as they exhibit lower hardness and minimal residual stress.

- Similar observations could be seen for tool offsetting during friction stir welding of dissimilar materials. By off-setting the tool towards retreating side a welding mode where minimal strain accumulation in steel and complete dynamic recrystallization in aluminum could be achieved.

- Furthermore, tool offset minimizes the amount of embedded chips of harder metal in the weld nugget. Micro-cracks, voids and other defects were effectively eliminated. The biggest advantage of tool offset during Fe-Al welding is the absence of inter-metallic compounds in the fusion zone. Their presence is detrimental to the weld strength. The established empirical relationship between the grain size and hardness enables the adjustment of axial loads during welding. This improves the bending susceptibility of welds.

- In an attempt to minimize the experimental work load, a thermo-metallurgical framework is developed. Though the models described are tested for fusion welding methods, they could be adapted to pressure welding as well. A novel three dimensional heat source model is developed that precisely describes the variation of thermal gradients in the different quadrants of weld. The accuracy in predicting temperature profiles at different points in the weld provides the opportunity to optimize welding parameters to produce long lasting joints.

5 Conclusions

- Finite element modelling of welding enables rapid optimisation of process parameters, predicts weld microstructure and thus aids in enhancing the durability of weldments while reducing the fabrication costs.

Bibliography

[1] Pengfei Wang, Xizhang Chen, Qiuhong Pan, Bruce Madigan, and Jiangqi Long. Laser welding dissimilar materials of aluminum to steel: an overview. *The International Journal of Advanced Manufacturing Technology*, 87(9):3081–3090, Dec 2016. ISSN 1433-3015. doi: 10.1007/s00170-016-8725-y. URL https://doi.org/10.1007/s00170-016-8725-y.

[2] E. Williams and N. Lavery. Laser processing of bulk metallic glass: A review. *Journal of Materials Processing Technology*, 247(Supplement C):73 – 91, 2017. ISSN 0924-0136. doi: https://doi.org/10.1016/j.jmatprotec. 2017.03.034. URL http://www.sciencedirect.com/science/article/pii/ S0924013617301279.

[3] Jagesvar Verma and Ravindra Vasantrao Taiwade. Effect of welding processes and conditions on the microstructure, mechanical properties and corrosion resistance of duplex stainless steel weldments - A review. *Journal of Manufacturing Processes*, 25(Supplement C):134 – 152, 2017. ISSN 1526-6125. doi: https://doi.org/10.1016/j.jmapro.2016.11.003. URL http://www. sciencedirect.com/science/article/pii/S152661251630158X.

[4] Wilfried Behr. International electron beam welding conference : lectures of the 2nd IEBW conference taking place in aachen on march 26-30, 2012. volume 285. DVS Media GmbH, Dusseldorf, 2012. ISBN 978-3-87155-299-1.

[5] S. A. David and T. DebRoy. Current issues and problems in welding science. *Science*, 257(5069):497–502, 1992. ISSN 0036-8075. doi: 10.1126/science. 257.5069.497. URL http://science.sciencemag.org/content/257/5069/ 497.

[6] A. Vinoth Jebaraj, L. Ajaykumar, C.R. Deepak, and K.V.V. Aditya. Weldability, machinability and surfacing of commercial duplex stainless steel AISI2205 for marine applications - a recent review. *Journal of Advanced Research*, 8 (3):183 – 199, 2017. ISSN 2090-1232. doi: https://doi.org/10.1016/j.jare. 2017.01.002. URL http://www.sciencedirect.com/science/article/pii/ S2090123217300115.

[7] P.K. Mallick. 8 - joining for lightweight vehicles. In P.K. Mallick, editor, *Materials, Design and Manufacturing for Lightweight Vehicles*, Woodhead Publishing Series in Composites Science and Engineering, pages 275 – 308. Woodhead Publishing, 2010. ISBN 978-1-84569-463-0. doi: https://doi. org/10.1533/9781845697822.2.275. URL http://www.sciencedirect.com/ science/article/pii/B9781845694630500080.

[8] J.C. Benedyk. 3 - aluminum alloys for lightweight automotive structures. In P.K. Mallick, editor, *Materials, Design and Manufacturing for Lightweight Vehicles*, Woodhead Publishing Series in Composites Science and Engineering, pages 79 – 113. Woodhead Publishing, 2010. ISBN 978-1-84569-463-0. doi: https://doi.org/10.1533/9781845697822.1.79. URL `http://www.sciencedirect.com/science/article/pii/B9781845694630500031`.

[9] M. Alali, I. Todd, and B.P. Wynne. Through-thickness microstructure and mechanical properties of electron beam welded 20mm thick aisi 316l austenitic stainless steel. *Materials & Design*, 130(Supplement C):488 – 500, 2017. ISSN 0264-1275. doi: https://doi.org/10.1016/j.matdes.2017.05.080. URL `http://www.sciencedirect.com/science/article/pii/S0264127517305610`.

[10] Yoshihiro Kusuda. Honda develops robotized fsw technology to weld steel and aluminum and applied it to a mass production vehicle. *Industrial Robot: An International Journal*, 40(3):208–212, 2013. doi: 10.1108/01439911311309889.

[11] A. Amini, P. Asadi, and P. Zolghadr. 15 - friction stir welding applications in industry. In Mohammad Kazem Besharati Givi and Parviz Asadi, editors, *Advances in Friction-Stir Welding and Processing*, Woodhead Publishing Series in Welding and Other Joining Technologies, pages 671 – 722. Woodhead Publishing, 2014. ISBN 978-0-85709-454-4. doi: https://doi.org/10.1533/9780857094551.671. URL `http://www.sciencedirect.com/science/article/pii/B978085709454450015X`.

[12] Krishna Komerla, Stefan Gach, Thomas Vossel, Alexander Schwedt, Andreas Bührig-Polaczek, Uwe Reisgen, and Wolfgang Bleck. The effect of beam oscillations on the microstructure and mechanical properties of electron beam welded steel joints. *The International Journal of Advanced Manufacturing Technology*, 102:1–13, 06 2019. doi: 10.1007/s00170-019-03355-4.

[13] Diego Ferreño, Javier Portilla Carral, Roberto Lacalle Calderón, José A. Álvarez, and Federico Gutiérrez-Solana. Development and experimental validation of a simplified finite element methodology to simulate the response of steel beams subjected to flame straightening. *Construction and Building Materials*, 137(Supplement C):535 – 547, 2017. ISSN 0950-0618. doi: https://doi.org/10.1016/j.conbuildmat.2017.02.001. URL `http://www.sciencedirect.com/science/article/pii/S0950061817301769`.

[14] R. Lacalle, JA Álvarez, D. Ferreño, J. Portilla, E. Ruiz, B. Arroyo, and F. Gutiérrez-Solana. Flame straightening application on structural steels: Effects on mechanical and fracture properties, Aug 2013. URL `https://doi.org/10.1201/b15963-76`. 0.

[15] X. Sun, K.S. Choi, W.N. Liu, and M.A. Khaleel. Predicting failure modes and ductility of dual phase steels using plastic strain localization. *International Journal of Plasticity*, 25(10):1888 – 1909, 2009. doi: http://dx.doi.org/10.1016/j.ijplas.2008.12.012. URL `http://www.sciencedirect.com/science/article/pii/S0749641908001897`.

[16] A. Ramazani, K. Mukherjee, A. Schwedt, P. Goravanchi, U. Prahl, and W. Bleck. Quantification of the effect of transformation-induced geometrically necessary dislocations on the flow-curve modelling of dual-phase steels. *International Journal of Plasticity*, 43:128 – 152, 2013. doi: http://dx.doi.org/10. 1016/j.ijplas.2012.11.003. URL `http://www.sciencedirect.com/science/article/pii/S0749641912001684`.

[17] C.C. Tasan, J.P.M. Hoefnagels, M. Diehl, D. Yan, F. Roters, and D. Raabe. Strain localization and damage in dual phase steels investigated by coupled in-situ deformation experiments and crystal plasticity simulations. *International Journal of Plasticity*, 63:198 – 210, 2014. doi: http://dx.doi.org/10.1016/j.ijplas. 2014.06.004. URL `http://www.sciencedirect.com/science/article/pii/S0749641914001260`. Deformation Tensors in Material Modeling in Honor of Prof. Otto T. Bruhns.

[18] Hidekazu Minami, Kyouhei Nakayama, Tatsuya Morikawa, Kenji Higashida, Yuki Toji, and Kohei Hasegawa. Effect of tempering conditions on inhomogeneous deformation behavior of ferrite-martensite dual-phase steels. *Tetsu-to-Hagane*, 97(9):493–500, 2011. doi: 10.2355/tetsutohagane.97.493.

[19] Kohei Hasegawa, Yuki Toji, Hidekazu Minami, Hiroshi Ikeda, Tatsuya Morikawa, and Kenji Higashida. Effect of martensite fraction on tensile properties of dual-phase steels. *Tetsu-to-Hagane*, 98(6):320–327, 2012. doi: 10.2355/tetsutohagane.98.320.

[20] C.C. Tasan, M. Diehl, D. Yan, M. Bechtold, F. Roters, L. Schemmann, C. Zheng, N. Peranio, D. Ponge, M. Koyama, K. Tsuzaki, and D. Raabe. An overview of dual-phase steels: Advances in microstructure-oriented processing and micromechanically guided design. *Annual Review of Materials Research*, 45 (1):391–431, 2015. doi: 10.1146/annurev-matsci-070214-021103. URL `http://dx.doi.org/10.1146/annurev-matsci-070214-021103`.

[21] Chengwu Zheng and Dierk Raabe. Interaction between recrystallization and phase transformation during intercritical annealing in a cold-rolled dual-phase steel: A cellular automaton model. *Acta Materialia*, 61(14):5504 – 5517, 2013. ISSN 1359-6454. doi: https://doi.org/10.1016/j.actamat. 2013.05.040. URL `http://www.sciencedirect.com/science/article/pii/S1359645413004187`.

[22] R.D. Thomas. Submerged-arc welding of hsla steel for low-temperature services. *Metal Progress*, 111(4):30 – 36, 1977.

[23] C. S. Lee, R. S. Chandel, and H. P. Seow. Effect of welding parameters on the size of heat affected zone of submerged arc welding. *Materials and Manufacturing Processes*, 15(5):649–666, 2000. doi: 10.1080/10426910008913011. URL `https://doi.org/10.1080/10426910008913011`.

[24] M. Li, F. Sun, D.F. Li, P.E. O'Donoghue, S.B. Leen, and N.P. O'Dowd. The effect of ferrite phases on the micromechanical response and crack initiation in the intercritical heat-affected zone of a welded 9cr martensitic steel. *Fatigue &*

Fracture of Engineering Materials & Structures, 41(6):1245–1259, 2018. doi: 10.1111/ffe.12768. URL `https://onlinelibrary.wiley.com/doi/abs/10.1111/ffe.12768`.

[25] L. E. Collins, M. J. Godden, and J. D. Boyd. Microstructures of linepipe steels. *Canadian Metallurgical Quarterly*, 22(2):169–179, 1983. doi: 10.1179/cmq.1983.22.2.169. URL `https://doi.org/10.1179/cmq.1983.22.2.169`.

[26] T. Lienert, T. Siewert, S. Babu, and V. Acoff. *ASM handbook*, volume 6A. ASM International, 2011. ISBN 978-1-61503-133-7.

[27] J. Ronda and G.J. Oliver. Consistent thermo-mechano-metallurgical model of welded steel with unified approach to derivation of phase evolution laws and transformation-induced plasticity. *Computer Methods in Applied Mechanics and Engineering*, 189(2):361 – 418, 2000. ISSN 0045-7825. doi: https://doi.org/10.1016/S0045-7825(99)00461-2. URL `http://www.sciencedirect.com/science/article/pii/S0045782599004612`.

[28] Dean Deng and Hidekazu Murakawa. Finite element analysis of temperature field, microstructure and residual stress in multi-pass butt-welded 2.25cr–1mo steel pipes. *Computational Materials Science*, 43(4):681 – 695, 2008. ISSN 0927-0256. doi: https://doi.org/10.1016/j.commatsci.2008.01.025. URL `http://www.sciencedirect.com/science/article/pii/S0927025608000219`.

[29] F. G. Caballero, C. Capdevila, and C. Garcia De Andres. Modelling of kinetics of austenite formation in steels with different initial microstructures. *ISIJ International*, 41(10):1093–1102, 2001. doi: 10.2355/isijinternational.41.1093.

[30] R. G. Thiessen. *Physically-based Modelling of Material Response to Welding*. PhD thesis, Delft University of Technology, 2006.

[31] E.A. Wilson and S.F. Medina. Application of koistinen and marburger's athermal equation for volume fraction of martensite to diffusional transformations obtained on continuous cooling 0·13%c high strength low alloy steel. *Materials Science and Technology*, 16(6):630–633, 2000. doi: 10.1179/026708300101508397. URL `https://doi.org/10.1179/026708300101508397`.

[32] H. H. Pan and G. J. Weng. Thermal stress and volume change during a cooling process involving phase transformation. *Journal of Thermal Stresses*, 15(1):1–23, 1992. doi: 10.1080/01495739208946117. URL `https://doi.org/10.1080/01495739208946117`.

[33] S. A. H. Motaman, K. Komerla, T. Storms, U. Prahl, C. Brecher, and W. Bleck. Experimental and numerical investigation of dual phase steels formability during laser-assisted hole-flanging. *AIP Conference Proceedings*, 1960(1):060005, 2018. doi: 10.1063/1.5034894. URL `https://aip.scitation.org/doi/abs/10.1063/1.5034894`.

[34] Hibbit, Karlsson, and Sorensen. *ABAQUS/Standard Analysis User's Manual*. Hibbit, Karlsson, Sorensen Inc., USA, 2017.

[35] B Basu and R Raman. Microstructural variations in a high-strength structural steel weld under isoheat input conditions. *Welding Journal (Miami, Fla)*, 81: 239S–248S, 11 2002.

[36] K. Kumar and Satish V. Kailas. The role of friction stir welding tool on material flow and weld formation. *Materials Science and Engineering: A*, 485 (1):367 – 374, 2008. ISSN 0921-5093. doi: https://doi.org/10.1016/j.msea. 2007.08.013. URL http://www.sciencedirect.com/science/article/pii/ S0921509307015419.

[37] Krishna Komerla, Andreas Naumov, Chris Mertin, Ulrich Prahl, and Wolfgang Bleck. Investigation of microstructure and mechanical properties of friction stir welded aa6016-t4 and dc04 alloy joints. *The International Journal of Advanced Manufacturing Technology*, 94:4209–4219, 02 2018. doi: https://doi.org/10. 1007/s00170-017-1022-6.

[38] John Goldak, Aditya Chakravarti, and Malcolm Bibby. A new finite element model for welding heat sources. *Metallurgical Transactions B*, 15(2):299–305, 1984. ISSN 03602141. doi: 10.1007/BF02667333.

[39] D. Rosenthal. Mathematical theory of heat distribution during welding and cutting. *Welding Journal*, 20(5):220–234, 1941.

[40] V. Pavelic, R. Tanbakuchi, O. A. Uyehara, and P. S. Myers. Experimental and computed temperature histories in Gas Tungsten Arc Welding of thin plates. *Welding Journal Research Supplement*, 48(7):295–305, 1969.

[41] S.-H. Cho and J.-W. Kim. Analysis of residual stress in carbon steel weldment incorporating phase transformations. *Science and Technology of Welding and Joining*, 7(4):212–216, 2002. doi: 10.1179/136217102225004257. URL http://dx.doi.org/10.1179/136217102225004257.

[42] Dean Deng, Hidekazu Murakawa, and Wei Liang. Numerical simulation of welding distortion in large structures. *Computer Methods in Applied Mechanics and Engineering*, 196(45–48):4613 – 4627, 2007. doi: http://dx.doi. org/10.1016/j.cma.2007.05.023. URL //www.sciencedirect.com/science/ article/pii/S0045782507002320.

[43] G. X. Xu, Chuan Song Wu, G. L. Qin, X. Y. Wang, and S. Y. Lin. Adaptive volumetric heat source models for laser beam and laser + pulsed GMAW hybrid welding processes. *International Journal of Advanced Manufacturing Technology*, 57(1-4):245–255, 2011. doi: 10.1007/s00170-011-3274-x.

[44] Jazeel Rahman Chukkan, M. Vasudevan, S. Muthukumaran, R. Ravi Kumar, and N. Chandrasekhar. Simulation of laser butt welding of AISI 316L stainless steel sheet using various heat sources and experimental validation. *Journal of Materials Processing Technology*, 219:48–59, may 2015. doi: 10.1016/j.jmatprotec.2014.12.008. URL http://www.sciencedirect.com/ science/article/pii/S0924013614004944.

[45] Krishna Komerla, Stefan Gach, Fatma Akyel, Thomas Vossel, Uwe Reisgen, and Wolfgang Bleck. Finite element simulation of residual stress induced by high energy beam welding in dual phase steel. *Lasers in Manufacturing and Materials Processing*, 03 2020. doi: https://doi.org/10.1007/s40516-020-00112-4.